

WA School of Mines, Energy and Chemical Engineering

Centre for Exploration Geophysics

Modeling the effect of liquid and solid infill on elastic
moduli, dispersion and attenuation in porous media

Yongyang Sun

This thesis is presented for the Degree of
Doctor of Philosophy
of
Curtin University

January 2020

Declaration

To the best of my knowledge and belief this thesis contains no material previously published by any other person except where due acknowledgement has been made.

This thesis contains no material which has been accepted for the award of any other degree or diploma in any university.

Signature:

Date:

Abstract

Establishing a link to quantify the effect of liquid and solid pore infill on elastic moduli, dispersion and attenuation in porous media is of great interest for many geophysical applications, such as reservoir characterization and time-lapse seismic monitoring. This quantification requires comprehensive knowledge of the physical properties and the fraction of each component, the interactions between one component to another, and the pore geometry.

In microporous media like fluid (gas or Newtonian fluid)-saturated rocks, elastic wave velocities measured at ultrasonic frequency are frequently observed to be greater than predicted by the Biot-Gassmann theory. This difference is usually explained by squirt-flow dispersion. A number of theoretical models have been proposed to quantify this effect, but more or less problems exist in these models. On the one hand, some of these models are developed based on different theories. The question then arises whether these models give similar or different predictions. On the other hand, most models concern the high-frequency limit and the Gassmann low-frequency limit rather than the full frequency range. Similar to the squirt-flow dispersion in fluid-saturated rocks, there exists so-called "solid squirt" effect in porous rocks saturated with elastic solid or viscoelastic substances. The presence of elastic solid or viscoelastic substances causes shear resistance, which prevents the pressure communication between different compliances of pores. Several solid substitution schemes have been proposed to model the solid squirt effect, but they are insufficient to explain the experimental data. The research above concerns the issue of microporous media. In nanoporous

media, ultrasonic measurements also provide us with a convenient way to study the elastic properties of nanoporous medium and various pore infill. Although applying poroelasticity theories that are proven to be effective in microporous media to nanoporous media directly is questionable, it is quite useful to study their applicability.

In this thesis, three squirt-flow dispersion models, including the equivalent inclusion-average stress (EIAS), the crack-pores effective medium (CPEM), and the Mavko-Jizba model (MJ) as well as its generalization (MJG), are first compared analytically. Subsequently, numerical examples are used to demonstrate the similarities and differences of these models. When we assume stiff pores to be spheres and a small crack density, we show analytically and numerically that the three models give almost identical predictions. When the stiff pores are spheroids with an aspect ratio < 1 , the predictions of the two inclusion-based models – EIAS and CPEM models – are invalid while the MJ and MJG models are valid at ultrasonic frequencies. Preference for the selection of one model or another depends on the pore geometry information. If the pore geometry is specified, the two inclusion-based models should be used. Otherwise, the MJ and MJG model would be preferred.

Then, we develop a micromechanically consistent model which integrates a stress-dependency model of dry velocities or moduli with a micromechanical model that characterizes a typical fluid-saturated compliant pore as a soft inclusion between adjacent grains. The stress-dependency model allows us to extract the pore geometry information at each pressure. We can obtain the fraction and the spectrum of aspect ratios for compliant pores as a function of effective pressures. The micromechanical model provides us with a method to model the frequency effect at full frequency range. We then apply this micromechanically consistent model to the ultrasonic and low-frequency measurements on several fluid-saturated sandstone and carbonate samples. The model predictions are reasonably consistent with the laboratory measurements.

Subsequently, we develop a triple-porosity model to characterize the solid squirt effect observed in the ultrasonic measurements on a sandstone sample saturated with a solid substance. This model divides pores into different shapes: stiff, compliant and so-called intermediate. Each type of pores is assumed to have a single aspect ratio. Solid squirt effect occurs between stiff and compliant pores at relatively low-pressure (say < 100 MPa) and between stiff and intermediate pores at relatively high-pressure (say 200-500 MPa or above). However, such pressures are hard to approach in most rock physics laboratories, thus an essential parameter, the high-pressure limit dry moduli of a hypothetical rock containing only stiff pores, is hard to obtain. To address this problem, we employ a numerical simulation method based on the finite element method integrated with a self-consistent medium theory to invert the aspect ratio, and in turn to compute the parameter. Modeling results for liquid-octadecane-saturated show an excellent consistency with the predictions of the Gassmann theory, which implies that this model will reduce to the Gassmann theory when the pore infill is a Newtonian fluid. Modeling results for solid-octadecane-saturated show a reasonable fit to the laboratory measurements, performing better than other solid substitution models.

Finally, we explore the effect of liquid and solid infill on the moduli of nanoporous media. To this end, we apply the Gassmann theory and the effective medium theory to a Vycor glass sample saturated with liquid and solid argon. One uncertainty in this study is related to the elastic constants of non-porous Vycor glass, which is hard to obtain in laboratory measurements. To address this issue, we first assume the nanopores to be spheroids of the same shape and can be characterized by a single average aspect ratio. We then apply the effective medium theory to invert the aspect ratio for the nanopores. Subsequently, we substitute the obtained aspect ratio into the same effective medium theory to compute the elastic moduli of non-porous Vycor glass. Modeling results using the Gassmann theory show a good agreement with the measured moduli of Vycor saturated with

liquid argon. Estimates by the differential effective medium theory also show a reasonable agreement with the measured shear modulus of the Vycor glass saturated with solid argon, but a considerable discrepancy in bulk modulus. This discrepancy may be caused by the confinement effect in nanopores, which makes the elastic properties of "confined" matter differ significantly from the "bulk" state.

To this end, we have analysed the effect of liquid and solid infill on elastic moduli, dispersion and attenuation in porous media. This will help shape the understanding of the relationship between the properties of pore infill and porous rocks, which will have a potential for reservoir characterization and time-lapse seismic monitoring.

Acknowledgements

First, I would like to express my deep and sincere appreciation to my supervisor Prof. Boris Gurevich for the last three and a half years he spent with me, discussing research ideas, debugging code, and editing manuscripts. His sincerity, enthusiasm, motivation, and insight have deeply inspired me. He has taught me the methodology to find the problems in literature and refresh your research ideas. He also has given me lots of tips and suggestions for improving my oral and written English. I am extremely grateful to the amazing supervision I received so far without which I would not have achieved so much progress. It was my great honour and privilege to study and work under his guidance.

I am also extremely grateful to my co-supervisors Dr Stanislav Glubokovskikh, Dr Vassili Mikhaltsevitch at Curtin University, and Prof. Christoph Arns at UNSW, and committee chair Prof. Maxim Lebedev for their insightful guidance, constructive discussion and technical support in some of our publications. With a special mention of Assoc. Pro. Gennady Gor and Dr José M Carcione, I would like to thank them for imposing scientific research idea and editing the manuscripts.

I would like to say thank you to all my Curtin colleagues for your support, friendship, and advice during my PhD. Very special gratitude goes out to all down to Nichole Sik.

Additionally, I would like to thank the China Scholarship Council (CSC) for the financial support of my PhD project.

List of Publications included in this thesis

1. Sun, Y., Carcione, J. M., and Gurevich, B. (2020). Squirt-flow seismic dispersion models: A comparison. *Geophysical Journal International*, 222(3), 2068-2082.
2. Sun, Y., and Gurevich, B. (2020). Modeling the effect of pressure on the moduli dispersion in fluid-saturated rocks. *Journal of Geophysical Research: Solid Earth*, 125(8), e2019JB019297.
3. Sun, Y., Gurevich, B., Lebedev, M., Glubokovskikh, S., Mikhaltsevitch, V., and Guo, J. (2019). A triple porosity scheme for fluid/solid substitution: theory and experiment. *Geophysical Prospecting*, 67(4), 888–899.
4. Sun, Y., Gurevich, B., Glubokovskikh, S., Lebedev, M., Squelch, A., Arns, C., and Guo, J. (2019). A solid/fluid substitution scheme constrained by pore-scale numerical simulations. *Geophysical Journal International*, 220(3), 1804-1812.
5. Sun, Y., Gurevich, B., and Gor, G. Y. (2019). Modeling elastic properties of vycor glass saturated with liquid and solid adsorbates. *Adsorption*, 25(5), 973–982.

Statement of candidate about the contribution of co-authors

I am the first author of all the publications included in this thesis. Each of these publications were based on the work in which I was the principle researcher, but which included collaboration with my co-authors. I wrote the papers independently, but receiving technical advice and review comments from my co-authors. Please see comments of my co-authors in Appendix A.

Contents

Abstract	v
Acknowledgements	ix
1 Introduction and Overview	1
1.1 Background and Motivation	2
1.2 The Objectives and Outlines	9
1.3 Thesis publications and their relations to the thesis topic	11
1.4 Conclusions and Outlook	17
1.4.1 Conclusions	17
1.4.2 Outlook	20
References	23
2 Published Papers	31
2.1 Squirt-flow seismic models: a comparison	32
2.2 Modelling the effect of pressure on the moduli dispersion in fluid-saturated rocks	48
2.3 A triple porosity scheme for fluid/solid substitution: theory and experiment	67

2.4	A solid/fluid substitution scheme constrained by pore-scale numerical simulations	80
2.5	Modeling elastic properties of Vycor glass saturated with liquid and solid adsorbate	90
	Appendices	101
	A Statements of co-authors	103
	B Copyright Information	113

Chapter 1

Introduction and Overview

1.1 Background and Motivation

Establishing a link between the pore fills and porous media is of considerable interest in geophysical practice, such as seismic reservoir characterization and time-lapse seismic monitoring. This requires an understanding of the fraction and elastic properties of minerals and pore infill, the interactions among these components, and the pore geometry. Pore infill can be either gas, liquid or solid. Gas pore infill includes air, CO₂, steam, and hydrocarbon gas. Liquid pore infill can be oil, brine and magma. Solid pore infill can be gas hydrates, salt, bitumen, ice, kerogen (Saxena et al., 2016). For porous rocks saturated with fluid, dispersion and accompanied attenuation of seismic waves have attracted substantial attention because hydrocarbon reservoirs are frequently observed to exhibit significant P-wave attenuation, especially at low frequencies within the seismic band (Chapman, Liu, & Li, 2006; Quintal, Schmalholz, & Podladchikov, 2011; Rapoport, Rapoport, & Ryjkov, 2004). A comprehensive understanding of the effect of fluid on the dispersion and attenuation of porous media can help in the quantitative interpretation and seismic inversion, especially for identifying the fluid-type and its distribution in a reservoir. For rocks saturated with elastic solids or viscoelastic substances, quantifying the effect of pore infill on the elastic moduli of porous rocks are also important, especially for heavy oil or bitumen (Bianco, Kaplan, & Schmitt, 2010; Schmitt, 1999). Heavy oil plays an important role in energy source in some areas of the world. Yet, analysis of elastic properties of rocks saturated with elastic solids or viscoelastic substances until recently received relatively little attention.

At low frequencies, the elastic properties of fluid-saturated porous media are given by the Gassmann theory (Gassmann, 1951). Yet, at ultrasonic frequencies, the elastic properties are often observed to be significantly greater than the predictions of the Biot-Gassmann theories (Biot, 1956a; Gassmann, 1951). This effect is known as squirt dispersion, one mechanism that characterizes the wave-induced fluid flow at pore-scale. The squirt-flow mechanism was first proposed

by Mavko and Nur (1975) as an explanation of observed viscoelastic relaxation in the asthenosphere. This difference between the Gassmann low-frequency limit and ultrasonic-frequency limit is usually explained by a double-porosity concept (Shapiro, 2003; Walsh, 1965): relatively stiff pores and relatively compliant (soft) pores. Stiff pores dominate the pore space while compliant pores occupy only a small portion of the pores space. Compliant pores are present between adjacent grains and explain the stress effect on elastic velocities or moduli. The existence of compliant pores in a dry rock decreases the elastic moduli substantially. When a rock is saturated with fluid, an elastic wave will cause different fluid pressures build-up in compliant and stiff pores, and thus pressure gradients between them. At sufficiently low frequencies, such pressure gradients have ample time to reach an equilibrium. This satisfies the key assumption of the Gassman theory. Yet at much higher frequencies, there is no time for the fluid pressure gradients to relax such that compliant pores are isolated from each other and from stiff pores. This stiffening effect significantly increases the elastic moduli of porous rocks, making them much higher than those in the low-frequency limit.

One class of theoretical models of squirt-flow dispersion characterizes the stiff pores by one aspect ratio within the range of 0.1–1 and the compliant pores by a spectrum of aspect ratios (<0.01) (Mavko & Nur, 1979; O’Connell & Budiansky, 1977; Palmer & Traviola, 1980). Another approach assumes both typical stiff and compliant pores to be spheroids each with one aspect ratio (de Paula, Pervukhina, Makarynska, & Gurevich, 2012; Gurevich, Makarynska, de Paula, & Pervukhina, 2010; Pride, Berryman, & Harris, 2004). Mavko and Jizba (1991) (referred as MJ) utilized the double-porosity pore structure to derive simple and general expressions for the elastic moduli of the rock with pores and cracks of arbitrary shapes in the high-frequency limit. In this model, stiff pores remain dry while compliant pores are saturated with fluid. This state is termed as so-called ”unrelaxed” frame. Then, the saturated moduli can be obtained by using the Gassmann theory (in which the dry bulk modulus is replaced with the bulk

modulus of the unrelaxed frame).

Gurevich, Makarynska, and Pervukhina (2009) pointed out that the pore fluid in the MJ model must be liquid, and extended the MJ model to the case of fluids with arbitrary bulk modulus (referred as MJG). The MJ and MJG models are both independent of pore space parameters such as aspect ratio, explicitly. In contrast, two inclusion-based models, the equivalent inclusion-stress (EIAS) model (Endres & Knight, 1997) and the crack-pores effective medium (CPEM) model (Adelinet, Fortin, & Guéguen, 2011), are designed for elastic media with spherical pores and oblate spheroidal cracks, thus the predictions of these two models explicitly are controlled by the aspect ratio of cracks and the volume fraction of spherical pores and cracks. Now comes the question of whether the predictions of the three models are similar or different. Neither Endres and Knight (1997) nor Adelinet et al. (2011) compared their models to the MJ model analytically or numerically. Adelinet et al. (2011) numerically compared the modeling results of the CPEM model to those given by the EIAS model and found a considerable difference, which they ascribed to the use of the Kuster and Toksöz (1974) model (referred as KT) in the EIAS model. Such explanation appears unsatisfactory because the models of both Kachanov (1993) and KT are designed using the same Eshelby (1957) theory. Hence, it is important to compare the three different models to figure out the similarities and differences among them analytically and numerically.

In contrast to the low-frequency limit, which is given by the Gassmann theory, and the high-frequency limit, which is given by the MJ and MJG models, modeling dispersion and attenuation at intermediate frequencies require the knowledge of the pore geometry. This fact helps explain why there are a number of models of squirt attenuation and dispersion and no universally accepted model. One approach describes the pore shape by several distinct aspect ratios (Gurevich et al., 2010; Pride et al., 2004), but this theory has several “free” parameters describing the pore geometry, including the fraction of compliant pores and the pore aspect

ratio. These parameters are hard to measure and have to be obtained by fitting to laboratory measurements, but an excellent fit is insufficient to prove that the approach is adequate. This uncertainty limits the applicability of the approach. To tackle this uncertainty, an alternative direct and more rigorous method is to obtain a spectrum of aspect ratios for compliant pores through the analysis of the stress-dependency of the dry velocities or moduli of porous rocks. Morlier (1971) first proposed a quantitative link between the continuous spectrum of aspect ratios at each pressure and the stress-dependency of the velocities or moduli. This quantitative relationship was refined by Zimmerman (1991) and David and Zimmerman (2012). In particular, David and Zimmerman (2013) employed this relationship and proposed a model for estimating the frequency effects on the moduli. However, different from the theories of Gurevich et al. (2010); Murphy (1982); Pride et al. (2004), or Glubokovskikh, Gurevich, and Saxena (2016), this approach does not give an explicit solution to the micromechanical problem for the fluid pressure gradients between pores of different shapes. Instead, it assumes that compliant pores are either isolated or inter-connected with each other. Hence, it would be interesting to develop a model that integrates the stress-dependency model with the micromechanical model of Gurevich et al. (2010) and Glubokovskikh et al. (2016).

The above discussion concerns rocks saturated with Newtonian fluids (liquids or gases). On the other hand, for rocks saturated with elastic solids or high-viscous materials or non-Newtonian fluids such as gas hydrates, salt, bitumen, ice or kerogen, the Gassmann theory is inapplicable due to presence of the pore in-fill with shear resistance, which will prevent the pressure communication between compliant and stiff pores (Glubokovskikh et al., 2016; Makarynska, Gurevich, Behura, & Batzle, 2010; Saxena & Mavko, 2014). Ciz and Shapiro (2007) (referred as CS model) extended the Gassmann theory for solid-saturated porous rocks. This approximation is identical to the Gassmann theory for bulk modulus and gives a similar expression for shear modulus. However, recent studies

(Glubokovskikh et al., 2016; Saxena & Mavko, 2014) showed that the CS model significantly underestimates the elastic moduli of porous rocks saturated with elastic solids or non-Newtonian fluids. This is due to that the CS model also follows the crucial assumption of the Gassmann theory, which assumes spatial uniform stress throughout the entire pore space. This assumption only makes sense when the pores are assumed to be of approximately the same shape. However, when compliant and stiff pores both are present, this assumption is no longer valid.

Mavko and Saxena (2013) and Saxena and Mavko (2014) proposed the embedded bound theory and argued that this theory defines the upper and lower bound for fluid/solid substitution. This theory assumes non-uniform stress throughout the pore space. Although this theory guarantees that the solid substitution results lie between the upper and lower bounds, it cannot be used to quantify the results without the knowledge of microstructural information. Makarynska et al. (2010) pointed out that the existence of low-aspect-ratio pores will cause significant increase of the difference between the effective shear modulus of porous rock in a dry or solid-saturated state. This effect is similar to the stiffening effect that occurs in fluid-saturated rocks at ultrasonic frequencies. Leurer and Dvorkin (2006) termed this similarity as "solid squirt". Hence, to describe this stiffening effect in the solid-saturated rocks, Glubokovskikh et al. (2016) adopted the solution of Tsai and Lee (1998) and modeled the saturated compliant pores as soft inclusions between adjacent grains. However, our experiments suggest that this model is insufficient to accurately characterize laboratory data. de Paula et al. (2012) showed that on the one hand, the elastic moduli of a hypothetical rock containing only equant pores obtained from ultrasonic measurements are much smaller than the predictions by any effective medium theory for spheres (Berryman, 1980). On the other hand, the estimated characteristic frequency of a typical compliant pore is close to the seismic frequency band but is well below ultrasonic frequencies. Thus, de Paula et al. (2012) argued that the squirt-flow effects are also affected

by the existence of so-called intermediate pores, which are softer than stiff pores but much stiffer than compliant pores. The same approach can be used to characterize the moduli of rocks saturated with elastic solids or high-viscous substances. Indeed, the parameters of compliant pores can be estimated through the analysis of the stress-dependency of the dry velocities or moduli. However to obtain the parameters of intermediate pores, we need to know the aspect ratio of stiff pores, which cannot be obtained directly as the high-pressure limit, where both compliant and intermediate pores are closed but only stiff pores remain open, corresponds to much higher pressures (say 200-500 MPa or above). Such pressures are out of reach of most rock physics laboratories and sometimes can crush core samples (Fortin, Guéguen, & Schubnel, 2007; Wong, David, & Zhu, 1997; Zhang, Wong, & Davis, 1990). Therefore, the high-pressure limit dry bulk and shear moduli cannot be measured directly. Alternatively, numerical simulation directly from microtomographic images of the porous samples using finite element method (FEM) provides a promising tool to compute these moduli (Arns, Knackstedt, Pinczewski, & Lindquist, 2001; Arns, Knackstedt, Pinczewski, & Garboczi, 2002; Roberts & Garboczi, 2000). If we assume that only stiff pore can be resolved in the digital rock images, the simulated elastic moduli using the FEM can be used to represent the high-pressure limit moduli.

Theories and models mentioned above are proposed and developed for macroporous materials. Applying these theories directly to nanoporous media is questionable. Physical properties of nanostructured materials, including nanoconfined matter and nanostructured non-porous matrix, may differ significantly from those of "normal" bulk materials (Huber, 2015). However, the combination of ultrasound and gas adsorption plays as a promising tool in characterizing nanoporous media. Elastic properties of liquid and solid pore infill can be obtained directly from ultrasonic measurements. So far, ultrasound method has been widely used for studying various pore infills (Charnaya et al., 2001; Molz, Wong, Chan, & Beamish, 1993; Page et al., 1995; Schappert & Pelster, 2008; Warner & Beamish,

1988). Particularly, this method can be used to estimate the fraction of pore infill (Warner & Beamish, 1988), pore pressures (Schappert & Pelster, 2016), phase transition of the pore infill (Charnaya et al., 2001), pore filling dynamics (Page et al., 1995). Gor and Gurevich (2018) showed that the predictions of the Gassmann theory are almost identical to the measured moduli of Vycor saturated with fluids, such as n-hexane (Page et al., 1995) and argon (Schappert & Pelster, 2014). Now comes the question of whether the poroelasticity theory can be used to characterize the effect of solid infill on the elastic moduli of nanoporous media. Schappert and Pelster (2013) published the data of the measured moduli of Vycor saturated with solid argon. Using the data of the moduli of Vycor saturated with argon in the liquid or solid state, we can explore the effect of liquid and solid pore infill on the moduli of nanoporous media through numerical analysis using poroelasticity theory and elastic effective medium theory. This will help develop methods to characterize confined fluid and solid phases using ultrasonic measurements.

1.2 The Objectives and Outlines

The general objective of this thesis is to study and model the effect of liquid and solid pore infill on elastic moduli, dispersion and attenuation in porous media. As discussed in section 1.1, several squirt-flow models have been proposed to quantify the moduli dispersion in fluid-saturated rocks, but their range of applicability is unclear. Thus it is important to compare and contrast the differences and similarities among these models analytically and numerically in order to figure out the advantages and disadvantages of these models, which forms the first objective of the thesis.

Objective 1. Compare the predictions of the the equivalent inclusion-stress (EIAS), the crack-pores effective medium (CPEM) and MJ and MJG models of seismic dispersion in porous rocks, and analyse their ranges of applicability and limitations

At intermediate frequencies that lie between the Gassmann low-frequency limit and the high-frequency limit given by the above models, quantifying the moduli dispersion requires the knowledge of pore geometry. As discussed in section 1.1, the existing models commonly characterize the pore shapes by spheroids with several aspect ratios. This treatment is oversimplified and restrictive as the pore shapes cannot be described by several distinct aspect ratios. Thus, it is essential to obtain a spectrum of aspect ratios rather than a single one directly from laboratory measurements. Besides, a micromechanical model is necessary to give a solution to the micromechanical problem for the fluid flow pressure gradients between pores of different shapes. Those requirements lead to the second objective of this thesis.

Objective 2. Develop a micromechanically consistent model to quantify the effects of pressure and frequency on moduli dispersion and attenuation in fluid-saturated rocks and analyse the validity of the proposed model against laboratory measurements.

For rocks saturated with elastic solids or viscoelastic substances or non-Newtonian

fluids, as discussed in section 1.1, the existing models including the CS model and the double-porosity model both underestimate the effects of pore infill on the overall rock moduli when compared against laboratory measurements. Hence, it is desirable to develop a new model to study the effects of elastic solids or viscoelastic substances on the overall elastic properties of porous and cracked rocks, which forms the third objective of this thesis.

Objective 3. Develop a model to describe the effects of liquid and solid infill on the elastic moduli of porous sandstones such that the model predictions are consistent with laboratory measurements.

Theories and models mentioned above are proposed and developed for macroporous materials. For nanoporous media, ultrasound is believed to be a promising tool for characterizing the effects of pore infill on the elastic velocities or moduli. However, as discussed in section 1.1, many of the existing results were qualitative rather than quantitative. Hence, it is fascinating to quantify the effect of various pore infill, solid or fluid, on the properties of nanoporous media using poroelasticity and elastic effective medium theory, which forms the fourth objective of this thesis.

Objective 4. Estimate the elastic properties of nanoporous media saturated with liquid and solid pore infill and compare the numerical modeling results against laboratory measurements.

1.3 Thesis publications and their relations to the thesis topic

The thesis is presented by five peer-reviewed journal papers. This chapter starts an overview of all the papers that highlights the main achievements relevant to the topic. Then, a detailed description is given for each paper to show what they have achieved and how they are interlinked.

1. Sun, Y., Carcione, J. M., and Gurevich, B. (2020). Squirt-flow seismic dispersion models: A comparison. *Geophysical Journal International*, 222(3), 2068-2082.

Wave propagation in porous rocks shows anelastic properties including velocity or moduli dispersion, and dissipation of energy. Such anelastic properties depend on frequency (Carcione, 2014; Jones, 1986; Müller, Gurevich, & Lebedev, 2010, e.g.). Several theoretical models (Adelinet et al., 2011; Endres & Knight, 1997; Gurevich et al., 2009; Mavko & Jizba, 1991) have been proposed to quantify the seismic dispersion, which is defined as the difference between low- and high-frequency moduli (Alkhimenkov et al., 2020; Chapman, Zatsepin, & Crampin, 2002; Dvorkin, Mavko, & Nur, 1995; Mavko & Nur, 1975; Murphy III, Winkler, & Kleinberg, 1986; O'Connell & Budiansky, 1977; Palmer & Traviola, 1980; Pride et al., 2004). In paper 1, we compare and contrast three squirt-flow dispersion models: Mavko and Jizba (1991) (MJ) model and its generalization (Gurevich et al., 2009, MJG), the Equivalent Inclusion- Stress (EIAS) model (Endres & Knight, 1997) and its dilute approximation and the Crack-Pores Effective Medium (CPEM) model (Adelinet et al., 2011). The three models are all based on a binary pore structure in which pores are composed of stiff pores and compliant pores (cracks). The MJG model is valid for porous media with pores and cracks of arbitrary shapes. Both EIASD and CPEM models are developed based on idealized geometries of spheres and ellipsoids. We first perform a detailed analytical comparison of these models, and then carry out a numerical analysis

to demonstrate the similarities and differences between these models. Both analytical and numerical comparisons show that when assuming stiff pores to be spheres and a small crack density, the predictions of the three models are identical. Subsequently, we suggest the preference of one model to another. If the pore geometry information is known or assumed, the EIASD or CEPM model would be preferred. Otherwise, the MJG model should be employed. In this paper, the Zener model is only used as a simple way to estimate attenuation from dispersion. While a priori the attenuation/dispersion pair does not have to adhere to the Zener model, existing models of squirt flow show that it does, see e.g., Carcione and Gurevich (2011).

- 2. Sun, Y., and Gurevich, B. (2020). Modeling the effect of pressure on the moduli dispersion in fluid-saturated rocks. *Journal of Geophysical Research: Solid Earth*, 125(8), e2019JB019297.**

For squirt-flow effects or solid squirt effects, a series of approaches characterize the pore shapes by one or two aspect ratios for compliant pores (double-porosity or triple porosity model) and a single aspect ratio for stiff pores (de Paula et al., 2012; Gurevich et al., 2010; Pride et al., 2004). An alternative series of theories describe the compliant pores by a spectrum of aspect ratios and the stiff pores by a single aspect ratio (O’Connell & Budiansky, 1977; Palmer & Traviola, 1980). However, these theories have several “free” parameters such as compliant porosity, the aspect ratio of compliant pores, etc. These parameters are hard to measure such that we have to obtain them by fitting to laboratory measurements. However, an excellent fitting is insufficient to prove that the model is adequate, thus it will lower the usefulness of the model.

To address this uncertainty, we develop a micromechanically consistent model that incorporates the stress-dependency model into a micromechanical squirt-flow model. This model, on the one hand, provides a direct and more rigorous approach to invert a continuous spectrum of aspect ratios rather than one for compliant pores through the analysis of stress-dependency of dry velocities or moduli, on the

other hand, provides an explicit solution to the mechanical problem for the fluid pressure gradients between pores of different compliances. We then apply this model to two sandstones samples saturated with water. The model predictions for the elastic moduli at ultrasonic frequency agree well with the ultrasonic measurements and are consistent with the Gassmann theory in the low-frequency limit. We then apply this model to two carbonates saturated with glycerin. The model predictions for the moduli dispersion and attenuation at low-frequency match well with the laboratory measurements using the forced-oscillation method.

- 3. Sun, Y., Gurevich, B., Lebedev, M., Glubokovskikh, S., Mikhaltsevitch, V., and Guo, J. (2019). A triple porosity scheme for fluid/solid substitution: theory and experiment. *Geophysical Prospecting*, 67(4), 888–899.**

Similar to squirt-flow effect in fluid-saturated rocks, Makarynska et al. (2010) suggested that the existence of compliant pores will cause a considerable increase in the difference between the shear resistance of the porous rocks in a dry state or saturated with elastic solid or viscoelastic substances. Leurer and Dvorkin (2006) recognized this similarity and termed this stiffening effect as "solid squirt". To quantify this effect, a number of theoretical models, including bounds and deterministic models, have been proposed (Ciz & Shapiro, 2007; Glubokovskikh et al., 2016; Saxena & Mavko, 2014, 2015). However, a significant discrepancy between the model predictions and experimental data still remains. To address this mismatch, we first extend the dual-porosity model of Glubokovskikh et al. (2016) model and propose a triple pore structure in which pores are divided into compliant, intermediate and stiff pores. This triple-porosity model can be used to characterize the solid squirt effect between compliant and stiff pores at relatively low pressures and between intermediate and stiff pores at relatively higher pressures. Applying the proposed mode to a sandstone sample saturated with octadecane in the liquid or solid state shows a reasonable agreement with the measurements. Besides, the triple-porosity model performs better than several

other substitution schemes when comparing the model predictions against laboratory measurements. This implies that the solid squirt effect is controlled by the combination of compliant, intermediate and stiff pores.

4. Sun, Y., Gurevich, B., Glubokovskikh, S., Lebedev, M., Squelch, A., Arns, C., and Guo, J. (2019). A solid/fluid substitution scheme constrained by pore-scale numerical simulations. *Geophysical Journal International*, 220(3), 1804-1812.

One uncertainty in the above method lies in the moduli of a hypothetical rock in a dry state. As discussed earlier, in the high-pressure limit, the hypothetical rock contains stiff pores only. However, this pressure corresponds to 200-500 MPa or above, which is out of reach of most rock physics laboratories (Fortin et al., 2007; Wong et al., 1997; Zhang et al., 1990). To eliminate the uncertainty, we introduce a pore-scale numerical simulation method integrated with the self-consistent medium theory. First, we obtain a series of numerically simulated elastic moduli of porous rock in a dry state based on different selected fragments of a microtomographic rock image using the finite element method (FEM) (Arns et al., 2001, 2002; Roberts & Garboczi, 2000). In this process, we assume the majority of the porosity resolved is stiff porosity. This assumption only applies to microtomographic images with a voxel size of about 2-5 μm , which is the minimum voxel size currently available. Rather than using the simulated moduli for the hypothetical rock directly, we invert the aspect ratio for stiff pores by comparing the predictions of self-consistent medium theory against the numerical simulation results. Then, we substitute the aspect ratio into the self-consistent medium theory and compute the moduli of the hypothetical rock in the high-pressure limit. This modification avoids the need to specify the shape of stiff pores in the implementation of the triple-porosity model, thus enhances the predictive power. Besides, the resulting predictions of properties of the fluid and solid-filled rock have no adjustable parameters and are consistent with measured properties.

5. Sun, Y., Gurevich, B., and Gor, G. Y. (2019). Modeling elastic properties of vycor glass saturated with liquid and solid adsorbates. *Adsorption*, 25(5), 973–982.

Previous papers focus on studying the effect of liquid and solid infill on elastic moduli, dispersion and attenuation in microporous media, in which the pore size is at mm to μm . In this work, we explore the effect of liquid and solid argon on the moduli of porous Vycor glass using the Gassmann theory and the effective medium theory. We assume the nanopores to be spheroids with a single aspect ratio. Under this assumption, we estimate the parameters, such as the moduli of non-porous Vycor and the aspect ratio for nanopores. Then, we compare the modeling results against the measured moduli of Vycor saturated with argon in the liquid or solid state. Predictions of the Gassmann theory match well with the measured moduli of Vycor saturated with argon in the liquid state at temperature $T=80\text{K}$. Estimates of the differential effective medium theory show a reasonable fit to the measured shear modulus of Vycor saturated with argon in the solid state at temperature $T=74\text{ K}$. However, there exists a considerable overestimation in bulk modulus, which might be caused by the confinement effect of "bulk" argon in nanopores. Taking into account the pore geometry might produce a better match to experiments, but but it appears information about pore geometry is scarce due to small (nanoscale) size of the pores in Vycor. Moreover, from the analysis of the measurements, it appears that properties of confined argon close to the melting point (which are not well understood) have a greater effect on the discrepancy than the shape of pores. Biot theory has indeed been used by some authors to describe mechanics of Vycor class, but as shown by Gor and Gurevich (2018) at ultrasonic frequencies of 6-13 MHz, the velocities are consistent with the low-frequency (Gassmann) limit of Biot theory, and thus are not affected by Biot's dispersion.

The five peer-reviewed journal papers together form a framework of characterizing the effect of liquid and solid infill on elastic moduli, dispersion and

attenuation in porous media. With the help of different methods that characterize the pore structure, we have developed a number of models for micro-porous rocks saturated with different pore infill (either fluid, high viscoelastic material, or elastic solid) and explored the effects of pore infill (either fluid or solid) on the elastic properties of the nanoporous medium. These works will have a potential for characterizing the squirt-flow dispersion from laboratory or field data, describing the elastic properties of the heavy-oil reservoir and 4D seismic monitoring.

1.4 Conclusions and Outlook

1.4.1 Conclusions

The main conclusions that are drawn from the five peer-viewed journal papers forming this thesis are:

1. Sun, Y., Carcione, J. M., and Gurevich, B. (2020). Squirt-flow seismic dispersion models: A comparison. *Geophysical Journal International*, 222(3), 2068-2082.

(1) An analytical comparison shows that when crack density is small and stiff pores are spheres, the predictions of the three models (MJG model and two idealized theoretical approaches EIASD and CPEM) are consistent. The numerical analysis further confirms this conclusion.

(2) When we assume stiff pores to be oblate spheroids with one aspect ratio < 1 , the EIASD and CPEM models predict the higher moduli than the MJG model.

(3) Our analysis shows that the predictions of inclusion-based models corresponds to the true high-frequency limit (10^9 Hz or higher) while the predictions of the MJG model corresponds to ultrasonic frequency (about 10^6 Hz). Yet, the EIASD and CPEM models can be modified to be consistent with the MJG model by using the Gassmann theory to account for the fluid effect in stiff pores.

(4) Since the three models give almost identical predictions, preference for selecting one model or another is quite useful. When the pore geometry is specified, the EIASD or CPEM model should be used. Otherwise, the MJG model would be preferred. But these models only apply to the case of low crack density. For relatively higher crack density, the EIAS model should be used since this model considers the interactions between cracks to some degree.

2. Sun, Y., and Gurevich, B. (2020). Modeling the effect of pressure on the moduli dispersion in fluid-saturated rocks. *Journal of Geophysical Research: Solid Earth*, 125(8), e2019JB019297.

(1) We propose a mechanically consistent model that incorporates a stress-dependency model of velocities or moduli, which allows us to obtain a spectrum of aspect ratio for compliant pores at each pressure, into a micromechanical model, which characterizes the wave-induced fluid pressure relaxation at each frequency.

(2) The most important aspect of the proposed model is that this scheme avoids the need for fitting to laboratory measurements on saturated samples. It provides a direct and more rigorous approach to obtaining a continuous distribution of aspect ratios rather than one aspect ratio for compliant pores through the analysis of the stress-dependency of velocities or moduli, thus, this treatment enhances the predictive power.

(3) Applying the proposed model to the Fontainebleau and Vosges sandstone samples saturated with water gives reasonable modeling results for the elastic moduli, which are consistent with the ultrasonic measurements. More importantly, the predictions of the proposed model at low-frequency also match well with the laboratory measurements of the Coquina and Indiana carbonate samples saturated with glycerin using the low-frequency forced oscillation technique.

3. Sun, Y., Gurevich, B., Lebedev, M., Glubokovskikh, S., Mikhaltsevitch, V., and Guo, J. (2019). A triple porosity scheme for fluid/solid substitution: theory and experiment. *Geophysical Prospecting*, 67(4), 888–899.

4. Sun, Y., Gurevich, B., Glubokovskikh, S., Lebedev, M., Squelch, A., Arns, C., and Guo, J. (2019). A solid/fluid substitution scheme constrained by pore-scale numerical simulations. *Geophysical Journal International*, 220(3), 1804-1812.

(1) We extend the double-porosity model and propose a triple-porosity model in which pores are divided into three type – stiff, compliant and so-called intermediate.

(2) The essential parameters for the triple-porosity model can be obtained from the stress-dependency of velocities or moduli of porous rocks.

(3) A significant drawback is an uncertainty of the dry moduli in the high-pressure limit, which is a key to the triple-porosity model. This essential parameter is hard to estimate directly from laboratory measurements. To tackle this problem, we introduce a pore-scale numerical simulation method integrated with the self-consistent medium theory.

(4) The numerical simulation method based on the finite-element method at pore-scale allows us to compute the dry elastic moduli directly from the microtomographic rock images. The self-consistent medium theory allows us to overcome the uncertainty of the numerically simulated elastic moduli, which depends on the selection of an "appropriate" fragment. The combination of these two theories provides us with an approach to invert a single aspect ratio for stiff pores and estimate the dry moduli in the high-pressure limit.

(5) The modified triple-porosity model gives a reasonable fit to the measured moduli of a Bentheim sandstone saturated with octadecane in the liquid or solid state, performing much better than the models of Ciz and Shapiro (2007) and Glubokovskikh et al. (2016).

5. Sun, Y., Gurevich, B., and Gor, G. Y. (2019). Modeling elastic properties of vycor glass saturated with liquid and solid adsorbates. *Adsorption*, 25(5), 973–982.

(1) Our modeling results show that the predictions of the Gassmann theory agree well with the measured moduli of Vycor saturated with argon in the liquid state at the temperature $T = 80$ K. Only a minor discrepancy is detected, which might be caused by the measurements error. This agreement is well consistent with the molecular modeling results (Dobrzanski, Maximov, & Gor, 2018; Gor, 2014; Gor et al., 2015).

(2) Estimates using the differential effective medium theory also agree well with the measured shear modulus of Vycor saturated with argon in the solid state at temperature $T=74$ K. However, the modeling results significantly overestimate the effective bulk modulus compared against the measurements. Possible

reasons that can account for this estimation might be the incompleteness of phase transition during the experiments and the difference between the bulk modulus of the "bulk" and the "nano-confined" solid argon.

(3) Our modeling results deepen the understanding of the effect of liquid and solid pore infill on the moduli of nanoporous media using poroelasticity and elastic effective medium theory. This will help develop methods to characterize confined fluid and solid phases using ultrasonic measurements.

1.4.2 Outlook

Quantifying the effect of liquid and solid pore infill on elastic moduli, dispersion, and attenuation is of great interests in geophysical applications. This thesis has achieved some progress that can help gain a deeper understanding of this issue. Aiming at different pore infill, we have proposed several theoretical models to estimate their effects quantitatively. Next steps would concentrate on exploring several issues.

In papers 2-5, I compared the proposed models against experimental data, especially in paper 2, I use the low-frequency forced-oscillation data to validate my predictions. More such comparisons are in order. Indeed, the model in paper 2 is more rigorous and was developed after the work on the 3rd and 4th paper. As such, in the future, it would be useful to build upon my model described in paper 2.

The proposed models assume that there are no interactions between cracks. This approximation may be inadequate for large crack density. Under this circumstance, complex methods such as differential effective medium theory (Berryman, 1980; David & Zimmerman, 2012; Norris, 1985; Salganik, 1973) may be employed. It would be straightforward to extend the proposed framework to estimate the interactions of cracks by incorporating any effective medium scheme, but the expressions would be too complex and need an iterative solution.

Furthermore, analytical squirt-flow models employed in this thesis all assume

no elastic interaction between cracks and pores. Alkhimenkov et al. (2020) showed by numerical simulation of a model geometry that this assumption results in some errors in predicted magnitude and shape of the moduli dispersion and attenuation. Hence, it would be interesting to develop theories accounting for the connection effect between the compliant and the stiff pores.

Also, the proposed models are limited to isotropic elastic media. Many porous media such as limestone, dolomite and shale are all anisotropic. Hence, it would be important to extend our models to anisotropic media using the framework proposed by Collet and Gurevich (2013, 2016a, 2016b).

Besides, the proposed model for fluid-saturated rocks is limited to dispersion that only occurs between compliant pores and stiff pores. We do not consider the interactions between compliant pores. This only applies to moderate to high-porosity rocks in which crack to pore flow dominates. For cracked rocks with low porosity, fluid flow between cracks will dominate. Then, the proposed model would be unsuitable and need to be extended to consider the fluid flow between cracks and pores and the flow between crack to crack.

Moreover, the test of our models should be regarded as strictly preliminary. Further laboratory experiments and real-field data are required to verify and improve our models. For solid-saturated media, experiments on different kinds of samples with a broader pressure range are necessary. Field data such as well-logging and seismic data of heavy oil reservoir are desirable. For fluid-saturated media, experiments both at ultrasonic frequency and low-frequency with a broader pressure range are essential to shed light on the understanding of the effect of liquid pore infill on elastic moduli, dispersion and attenuation.

Some of the models developed in this thesis quantify the effect of fluid using the Gassmann theory, where the dry frame modulus is replaced with the unrelaxed frame modulus. However, the solid in this system is not uniform, and hence, strictly speaking, the Gassmann theory is not applicable. It would be interesting to develop a more theoretically consistent approach using the theory of Brown

and Korringa (1975).

References

- Adelinet, M., Fortin, J., & Guéguen, Y. (2011). Dispersion of elastic moduli in a porous-cracked rock: Theoretical predictions for squirt-flow. *Tectonophysics*, *503*(1), 173–181.
- Alkhimenkov, Y., Caspari, E., Gurevich, B., Barbosa, N. D., Glubokovskikh, S., Hunziker, J., & Quintal, B. (2020). Frequency-dependent attenuation and dispersion caused by squirt flow: Three-dimensional numerical study. *Geophysics*, *85*(3), 129–145.
- Arns, C. H., Knackstedt, M. A., Pinczewski, M. V., & Lindquist, W. (2001). Accurate estimation of transport properties from microtomographic images. *Geophysical research letters*, *28*(17), 3361–3364.
- Arns, C. H., Knackstedt, M. A., Pinczewski, W. V., & Garboczi, E. J. (2002). Computation of linear elastic properties from microtomographic images: Methodology and agreement between theory and experiment. *Geophysics*, *67*(5), 1396–1405.
- Berryman, J. G. (1980). Long-wavelength propagation in composite elastic media ii. ellipsoidal inclusions. *The Journal of the Acoustical Society of America*, *68*(6), 1820–1831.
- Bianco, E., Kaplan, S., & Schmitt, D. (2010). Seismic rock physics of steam injection in bituminous-oil reservoirs. In *Heavy oils: Reservoir characterization and production monitoring* (pp. 107–112). Society of Exploration Geophysicists.
- Biot, M. A. (1956a). Theory of propagation of elastic waves in a fluid-saturated

- porous solid. I. Low frequency range. *The Journal of the Acoustical Society of America*, 28, 179–191.
- Brown, R. J., & Korringa, J. (1975). On the dependence of the elastic properties of a porous rock on the compressibility of the pore fluid. *Geophysics*, 40(4), 608–616.
- Carcione, J. M. (2014). *Wave fields in real media: theory and numerical simulation of wave propagation in anisotropic, anelastic, porous and electromagnetic media*. Elsevier.
- Carcione, J. M., & Gurevich, B. (2011). Differential form and numerical implementation of biot’s poroelasticity equations with squirt dissipation. *Geophysics*, 76(6), N55–N64.
- Chapman, M., Liu, E., & Li, X.-Y. (2006). The influence of fluid sensitive dispersion and attenuation on avo analysis. *Geophysical Journal International*, 167(1), 89–105.
- Chapman, M., Zatsepin, S. V., & Crampin, S. (2002). Derivation of a microstructural poroelastic model. *Geophysical Journal International*, 151(2), 427–451.
- Charnaya, E., Plotnikov, P., Michel, D., Tien, C., Borisov, B., Sorina, I., & Martynova, E. (2001). Acoustic studies of melting and freezing for mercury embedded into vycor glass. *Physica B: Condensed Matter*, 299(1-2), 56–63.
- Ciz, R., & Shapiro, S. A. (2007). Generalization of gassmann equations for porous media saturated with a solid material. *Geophysics*, 72(6), A75–A79.
- Collet, O., & Gurevich, B. (2013). Fluid dependence of anisotropy parameters in weakly anisotropic porous media. *Geophysics*, 78(5), WC137–WC145.
- Collet, O., & Gurevich, B. (2016a). Frequency dependence of anisotropy in fluid saturated rocks—part i: aligned cracks case. *Geophysical Prospecting*, 64(Advances in Rock Physics), 1067–1084.
- Collet, O., & Gurevich, B. (2016b). Frequency dependence of anisotropy in fluid saturated rocks—part ii: Stress-induced anisotropy case. *Geophysical*

- Prospecting*, 64(Advances in Rock Physics), 1085–1097.
- David, E., & Zimmerman, R. W. (2012). Pore structure model for elastic wave velocities in fluid-saturated sandstones. *Journal of Geophysical Research: Solid Earth*, 117(B7).
- David, E., & Zimmerman, R. W. (2013). Model for frequency-dependence of elastic wave velocities in porous rocks. In *Poromechanics v: Proceedings of the fifth biot conference on poromechanics* (pp. 2431–2440).
- de Paula, O. B., Pervukhina, M., Makarynska, D., & Gurevich, B. (2012). Modeling squirt dispersion and attenuation in fluid-saturated rocks using pressure dependency of dry ultrasonic velocities. *Geophysics*, 77(3), WA157–WA168.
- Dobrzanski, C. D., Maximov, M. A., & Gor, G. Y. (2018). Effect of pore geometry on the compressibility of a confined simple fluid. *The Journal of chemical physics*, 148(5), 054503.
- Dvorkin, J., Mavko, G., & Nur, A. (1995). Squirt flow in fully saturated rocks. *Geophysics*, 60(1), 97–107.
- Endres, A. L., & Knight, R. J. (1997). Incorporating pore geometry and fluid pressure communication into modeling the elastic behavior of porous rocks. *Geophysics*, 62(1), 106–117.
- Eshelby, J. D. (1957). The determination of the elastic field of an ellipsoidal inclusion, and related problems. *Proceedings of the royal society of London. Series A. Mathematical and physical sciences*, 241(1226), 376–396.
- Fortin, J., Guéguen, Y., & Schubnel, A. (2007). Effects of pore collapse and grain crushing on ultrasonic velocities and vp/vs. *Journal of Geophysical Research: Solid Earth*, 112(B8).
- Gassmann, F. (1951). Über die Elastizität poröser Medien. *Viertel. Naturforsch. Ges. Zürich*, 96, 1–23.
- Glubokovskikh, S., Gurevich, B., & Saxena, N. (2016). A dual-porosity scheme for fluid/solid substitution. *Geophysical Prospecting*, 64(Advances in Rock

- Physics), 1112–1121.
- Gor, G. Y. (2014). Adsorption stress changes the elasticity of liquid argon confined in a nanopore. *Langmuir*, *30*(45), 13564–13569.
- Gor, G. Y., & Gurevich, B. (2018). Gassmann theory applies to nanoporous media. *Geophysical Research Letters*, *45*(1), 146–155.
- Gor, G. Y., Siderius, D. W., Rasmussen, C. J., Krekelberg, W. P., Shen, V. K., & Bernstein, N. (2015). Relation between pore size and the compressibility of a confined fluid. *The Journal of chemical physics*, *143*(19), 194506.
- Gurevich, B., Makarynska, D., de Paula, O. B., & Pervukhina, M. (2010). A simple model for squirt-flow dispersion and attenuation in fluid-saturated granular rocks. *Geophysics*, *75*(6), N109–N120.
- Gurevich, B., Makarynska, D., & Pervukhina, M. (2009). Ultrasonic moduli for fluid-saturated rocks: Mavko-jizba relations rederived and generalized. *Geophysics*, *74*(4), N25–N30.
- Huber, P. (2015). Soft matter in hard confinement: phase transition thermodynamics, structure, texture, diffusion and flow in nanoporous media. *Journal of Physics: Condensed Matter*, *27*(10), 103102.
- Jones, T. (1986). Pore fluids and frequency-dependent wave propagation in rocks. *Geophysics*, *51*(10), 1939–1953.
- Kachanov, M. (1993). Elastic solids with many cracks and related problems. In *Advances in applied mechanics* (Vol. 30, pp. 259–445). Elsevier.
- Kuster, G. T., & Toksöz, M. N. (1974). Velocity and attenuation of seismic waves in two-phase media: Part i. theoretical formulations. *Geophysics*, *39*(5), 587–606.
- Leurer, K. C., & Dvorkin, J. (2006). Viscoelasticity of precompacted unconsolidated sand with viscous cement. *GEOPHYSICS*, *71*(2), T31–T40.
- Makarynska, D., Gurevich, B., Behura, J., & Batzle, M. (2010). Fluid substitution in rocks saturated with viscoelastic fluids. *Geophysics*, *75*(2), E115–E122.
- Mavko, G., & Jizba, D. (1991). Estimating grain-scale fluid effects on velocity

- dispersion in rocks. *Geophysics*, 56(12), 1940–1949.
- Mavko, G., & Nur, A. (1975). Melt squirt in the aesthenosphere. *Geophysical Journal International*, 80(11), 1444–1448.
- Mavko, G., & Nur, A. (1979). Wave attenuation in partially saturated rocks. *Geophysics*, 44(2), 161–178.
- Mavko, G., & Saxena, N. (2013). Embedded-bound method for estimating the change in bulk modulus under either fluid or solid substitution. *Geophysics*, 78(5), L87–L99.
- Molz, E., Wong, A. P., Chan, M. H.-W., & Beamish, J. (1993). Freezing and melting of fluids in porous glasses. *Physical Review B*, 48(9), 5741.
- Morlier, P. (1971). Description of the state of rock fracturization through simple non-destructive tests. *Rock Mechanics*, 3(3), 125–138.
- Müller, T. M., Gurevich, B., & Lebedev, M. (2010). Seismic wave attenuation and dispersion resulting from wave-induced flow in porous rocks—a review. *Geophysics*, 75(5), 75A147–75A164.
- Murphy, W. F. (1982). *Effects of microstructure and pore fluids on the acoustic properties of granular sedimentary materials* (Unpublished doctoral dissertation). Stanford University.
- Murphy III, W., Winkler, K., & Kleinberg, R. (1986). Acoustic relaxation in sedimentary rocks—dependence on grain contacts and fluid saturation. *Geophysics*, 51(3), 757–766.
- Norris, A. N. (1985). A differential scheme for the effective moduli of composites. *Mechanics of materials*, 4(1), 1–16.
- O’Connell, R. J., & Budiansky, B. (1977). Viscoelastic properties of fluid-saturated cracked solids. *Journal of Geophysical Research: Solid Earth*, 82(36), 5719–5735.
- Page, J., Liu, J., Abeles, B., Herbolzheimer, E., Deckman, H., & Weitz, D. (1995). Adsorption and desorption of a wetting fluid in vycor studied by acoustic and optical techniques. *Physical Review E*, 52(3), 2763.

- Palmer, I., & Traviola, M. (1980). Attenuation by squirt flow in undersaturated gas sands. *Geophysics*, *45*(12), 1780—1792.
- Pride, S. R., Berryman, J. G., & Harris, J. M. (2004). Seismic attenuation due to wave-induced flow. *Journal of Geophysical Research: Solid Earth*, *109*(B01201).
- Quintal, B., Schmalholz, S. M., & Podladchikov, Y. Y. (2011). Impact of fluid saturation on the reflection coefficient of a poroelastic layer. *Geophysics*, *76*(2), N1–N12.
- Rapoport, M. B., Rapoport, L. I., & Ryjkov, V. I. (2004). Direct detection of oil and gas fields based on seismic inelasticity effect. *The Leading Edge*, *23*(3), 276–278.
- Roberts, A. P., & Garboczi, E. J. (2000). Elastic properties of model porous ceramics. *Journal of the American Ceramic Society*, *83*(12), 3041–3048.
- Salganik, R. (1973). Mechanics of bodies with many cracks. *Mech. Solids*, *8*(4), 135–143.
- Saxena, N., & Mavko, G. (2014). Exact equations for fluid and solid substitution. *Geophysics*, *79*(3), L21–L32.
- Saxena, N., & Mavko, G. (2015). Effects of fluid-shear resistance and squirt flow on velocity dispersion in rocks. *Geophysics*, *80*(2), D99–D110.
- Saxena, N., Mavko, G., Hofmann, R., Gurevich, B., Glubokovskikh, S., Aliyeva, S., & Dutta, P. (2016). Rock-physics models for heavy-oil and organic-solid substitution. *The Leading Edge*, *35*(6), 506–510.
- Schappert, K., & Pelster, R. (2008). Elastic properties and freezing of argon confined in mesoporous glass. *Physical Review B*, *78*(17), 174108.
- Schappert, K., & Pelster, R. (2013). Elastic properties of liquid and solid argon in nanopores. *Journal of Physics: Condensed Matter*, *25*(41), 415302.
- Schappert, K., & Pelster, R. (2014). Influence of the laplace pressure on the elasticity of argon in nanopores. *EPL (Europhysics Letters)*, *105*(5), 56001.
- Schappert, K., & Pelster, R. (2016). Experimental method for the determination

- of adsorption-induced changes of pressure and surface stress in nanopores. *Journal of Physics: Condensed Matter*, 29(6), 06LT01.
- Schmitt, D. R. (1999). Seismic attributes for monitoring of a shallow heated heavy oil reservoir: A case study. *Geophysics*, 64(2), 368–377.
- Shapiro, S. A. (2003). Elastic piezosensitivity of porous and fractured rocks. *Geophysics*, 68(2), 482–486.
- Sun, Y., Carcione, J. M., & Gurevich, B. (2020). Squirt-flow seismic dispersion models: A comparison. *Geophysical Journal International*, 222(3), 2068–2082.
- Sun, Y., & Gurevich, B. (2020). Modeling the effect of pressure on the moduli dispersion in fluid-saturated rocks. *Journal of Geophysical Research: Solid Earth*, 125(8), e2019JB019297.
- Sun, Y., Gurevich, B., Glubokovskikh, S., Lebedev, M., Squelch, A., Arns, C., & Guo, J. (2019). A solid/fluid substitution scheme constrained by pore-scale numerical simulations. *Geophysical Journal International*, 220(3), 1804–1812.
- Sun, Y., Gurevich, B., & Gor, G. Y. (2019). Modeling elastic properties of vycor glass saturated with liquid and solid adsorbates. *Adsorption*, 25(5), 973–982.
- Sun, Y., Gurevich, B., Lebedev, M., Glubokovskikh, S., Mikhaltsevitch, V., & Guo, J. (2019). A triple porosity scheme for fluid/solid substitution: theory and experiment. *Geophysical Prospecting*, 67(4), 888–899.
- Tsai, H.-C., & Lee, C.-C. (1998). Compressive stiffness of elastic layers bonded between rigid plates. *International Journal of Solids and Structures*, 35(23), 3053–3069.
- Walsh, J. (1965). The effect of cracks on the compressibility of rock. *Journal of Geophysical Research*, 70(2), 381–389.
- Warner, K., & Beamish, J. (1988). Ultrasonic measurement of the surface area of porous materials. *Journal of applied physics*, 63(9), 4372–4376.

-
- Wong, T., David, C., & Zhu, W. (1997). The transition from brittle faulting to cataclastic flow in porous sandstones: Mechanical deformation. *Journal of Geophysical Research: Solid Earth*, 102(B2), 3009-3025.
- Zhang, J., Wong, T.-F., & Davis, D. M. (1990). Micromechanics of pressure-induced grain crushing in porous rocks. *Journal of Geophysical Research: Solid Earth*, 95(B1), 341-352.
- Zimmerman, R. W. (1991). Aspect ratio distributions. In *Compressibility of sandstones*. Elsevier.

Chapter 2

Published Papers

2.1 Squirt-flow seismic models: a comparison

Squirt-flow seismic dispersion models: a comparison

Yongyang Sun¹, José M. Carcione^{2,3} and Boris Gurevich¹

¹Centre for Explorations Geophysics, Curtin University, G.P.O. Box U1987, Perth, WA 6845, Australia. E-mail: yongyang.sun@postgrad.curtin.edu.au

²Istituto Nazionale di Oceanografia e di Geofisica Sperimentale (OGS), Borgo Grotta Gigante 42c, 34010 Sgonico, Trieste, Italy

³School of Earth Sciences and Engineering, Hohai University, Nanjing 211100, China

Accepted 2020 May 30. Received 2020 May 29; in original form 2020 February 20

SUMMARY

The anelastic properties of porous rocks depend on the pore characteristics, specifically, the pore aspect ratio and the pore fraction (related to the soft porosity). At high frequencies, there is no fluid pressure communication throughout the pore space and the rock becomes stiffer than at low frequencies, where the pore pressure is fully equilibrated. This causes a significant difference between the moduli at low and high frequencies, which is known as seismic dispersion and is commonly explained by the squirt-flow mechanism. In this paper, we consider and contrast three squirt-flow dispersion models: the modified Mavko–Jizba model, valid for a porous medium with arbitrary shapes of the pores and cracks, and two other models, based on idealized geometries of spheres and ellipsoids: the EIAS (equivalent inclusion-average stress) and CPEM (cracks and pores effective medium) models. We first perform analytical comparisons and then compute several numerical examples to demonstrate similarities and differences between the models. The analytical comparison shows that when the stiff pores are spherical and the crack density is small, the theoretical predictions of the three models are very close to each other. However, when the stiff pores are spheroids with an aspect ratio smaller than 1 (say, between 0.2 and 1), the predictions of inclusion based models are not valid at frequencies of ultrasonic measurements on rock samples. In contrast, the predictions of the modified Mavko–Jizba model are valid at ultrasonic frequencies of about 10^6 Hz, which is a typical frequency of laboratory measurements on core samples. We also introduce Zener-based bulk and shear dispersion indices, which are proportional to the difference between the high- and low-frequency stiffness moduli, and are a measure of the degree of anelasticity, closely related to the quality factors by view of the Kramers–Kronig relations. The results show that the three models yield similar moduli dispersion with very small differences when the crack density is relatively high. The indices versus crack density can be viewed as a template to obtain the crack properties from low- and high-frequency velocity measurements.

Key words: Microstructure; Acoustic properties; Seismic attenuation.

1 INTRODUCTION

Wave propagation in rocks shows anelastic properties, namely, velocity dispersion and dissipation of energy depending on frequency (e.g. Jones 1986; Müller *et al.* 2010; Carcione 2014). In many rocks, the dispersion is caused by squirt flow, that is by fluid pressure equilibration between stiff pores, which occupies almost all the pore space, and soft pores or cracks, whose overall volume is very small but which strongly affect the overall rock moduli and are themselves sensitive to effective pressure (e.g. Walsh 1965; Zimmerman 1991; Zhang *et al.* 2019a, b). At low frequencies, the pore fluid has enough time to equilibrate throughout the pore space, and the wet-rock moduli are given by Gassmann (1951) equations. Conversely, at high frequencies, there is not enough time for fluid pressure to equilibrate between soft and stiff pores, and hence the overall moduli become higher. The difference between low- and high-frequency moduli quantifies seismic dispersion (Mavko & Nur 1975; O’Connell & Budiansky 1977; Palmer & Traviola 1980; Murphy *et al.* 1986; Dvorkin *et al.* 1995; Chapman *et al.* 2002; Pride *et al.* 2004; Alkhimenkov *et al.* 2020).

Several theoretical models have been proposed to quantify this dispersion. Mavko & Jizba (1991) proposed a model for so-called unrelaxed frame, whose soft pores are liquid saturated while stiff pores are dry. The moduli of the fully liquid-saturated rock are then computed using Gassmann equation (in which the dry bulk modulus is replaced with the modulus of the unrelaxed frame). In the Mavko &

Jizba (1991, MJ) model, the pore fluid must be liquid, but (Gurevich *et al.* 2009) generalized the MJ model to fluids of arbitrary bulk modulus. Similarly to Gassmann equation, both the original MJ model and the generalized version of Gurevich *et al.* (2009, MJG) do not depend on the parameters of the pore space, such as aspect ratios, explicitly.

In contrast, the equivalent inclusion-average stress (EIAS) model (Endres & Knight 1997) and the crack-pores effective medium (CPEM) model (Adelinet *et al.* 2011) use effective medium theory designed for elastic media with pores and cracks of oblate spheroidal shape, and their predictions explicitly depend on these aspect ratios and volume fractions of these pores and cracks. Thus, the question arises as to whether their predictions are the same or similar. Neither Endres & Knight (1997) nor Adelinet *et al.* (2011) compare their results to the MJ model. Adelinet *et al.* (2011) numerically compared the CPEM results to the EIAS results and found a significant discrepancy, which they attribute to the use of Kuster & Toksöz (1974, KT) model in the EIAS. This explanation is unconvincing as both Kachanov (1993) and KT models are based on the same Eshelby (1957) theory.

In general, it is extremely difficult to observe dispersion in seismic or acoustic field data due to limited frequency range of field data, which seldom cover more than one decade in frequency. However dispersion is directly related to attenuation, which is known to affect seismic and acoustic field data. Precise dependence of attenuation on frequency is controlled by details of the pore shape distribution. However, the Zener or standard-linear solid model (e.g. Carcione 2014) provides a precise mathematical relation between the amount of dispersion and the minimum quality factor, Q_0 , of the relaxation peak, or equivalently, the maximum dissipation factor, Q_0^{-1} . The model satisfies the Kramers-Kronig relations (Carcione *et al.* 2019). We introduce here the bulk and shear dispersion indices based on the Zener model, which are proportional to the difference between the high- and low-frequency stiffness moduli, and are a measure of the degree of anelasticity. The associated quality factor is that of the Zener model, which is a good representation of the relaxation peaks related to the squirt-flow attenuation mechanism, by which flow from fluid-filled microcracks (and grain contacts) to the stiff pore space and vice versa, induces energy dissipation (Carcione & Gurevich 2011). Biot (1962) was the first to discuss this mechanism and proposed a viscoelastic mechanical model to describe it.

In this paper, we perform a detailed analytical comparison of the dispersion predicted by the three models, CPEM, MJ with its generalization MJG and EIAS with its dilute approximation, and illustrate their similarities and differences by numerical examples. Plots of the dispersion indices as a function of the crack fraction and aspect ratio can be viewed as templates to obtain these properties from low- and high-frequency velocity measurements.

2 THE DISPERSION MODELS

We study three models, namely, the generalized MJ model (Mavko & Jizba 1991; Gurevich *et al.* 2009), the EIAS model by Endres & Knight (1997) and CPEM model of Adelinet *et al.* (2011). In the EIAS and CPEM models, the medium under study consists on an isotropic distribution of pores or cracks, respectively spheres and spheroids, whereas the MJ model considers pores and cracks of more general shapes (with aspect ratio on the order of 1 for pores and $\ll 1$ for cracks). Here, the crack fraction is denoted by c and the aspect ratio by a .

The EIAS and CPEM models yield the low-frequency bulk and shear moduli, K_0 and μ_0 , and the high-frequency bulk and shear moduli, K_∞ and μ_∞ , as functions of the aspect ratio and crack fraction. Both models have their root in the work of Eshelby (1957). The physics behind these inclusion-based models is as follows. A wave induces a higher fluid pressure in the cracks and the excess pressure is relieved to the spherical pores, so that $K_\infty > K_0$. This effect increases as the crack aspect ratio decreases.

2.1 THE EIAS MODEL

Endres & Knight (1997) assume that the stiff pores are spheres and the soft pores are spheroidal (penny-shaped) cracks of aspect ratio $a \ll 1$. At high frequencies, they assume that cracks are hydraulically isolated from the pores. The corresponding moduli K_∞ and μ_∞ predicted by Endres & Knight (1997, eqs 32 and 33), are

$$\begin{aligned} K_\infty &= K_s + \frac{\phi(K_f - K_s)\gamma}{1 - \phi(1 - \gamma)}, \\ \mu_\infty &= \frac{\mu_s(1 - \phi)}{1 - \phi(1 - \chi)}, \end{aligned} \quad (1)$$

where K_f is the fluid bulk modulus, ϕ is the total porosity, and

$$\begin{aligned} \gamma &= (1 - c)P_1 + cP_2, \\ \chi &= (1 - c)Q_1 + cQ_2 \end{aligned} \quad (2)$$

(Endres & Knight 1997, eqs 54 and 55) with

$$\begin{aligned} P_1 &= \frac{K_s + 4\mu_s/3}{K_f + 4\mu_s/3}, \\ P_2 &= \frac{K_s}{K_f + \pi a\beta}, \quad \beta = \mu_s \cdot \frac{3K_s + \mu_s}{3K_s + 4\mu_s} \\ Q_1 &= 1 + \mu_s/\zeta, \quad \zeta = \frac{\mu_s}{6} \cdot \frac{9K_s + 8\mu_s}{K_s + 2\mu_s}, \\ Q_2 &= \frac{1}{5} \left[1 + \frac{8\mu_s}{\pi a(\mu_s + 2\beta)} + 2 \cdot \frac{K_f + 2\mu_s/3}{K_f + \pi a\beta} \right], \end{aligned} \quad (3)$$

where P_1 and Q_1 correspond to spherical (stiff) pores and P_2 and Q_2 to penny-shaped (soft) cracks, with very low aspect ratios. Coefficients P_2 and Q_2 are approximations for $a \ll 1$. K_s and μ_s are the bulk and shear moduli of the grains.

At low frequencies, Endres & Knight (1997) assume complete fluid pressure communication between pores and cracks, the effective moduli are (Endres & Knight 1997, eqs 34 and 35),

$$\begin{aligned} K_0 &= K_s + \frac{\phi K_s (K_f - K_s) \gamma_0}{(1 - \phi)(K_s - K_f) + [K_f + \phi(K_s - K_f)] \gamma_0}, \\ \mu_0 &= \frac{\mu_s(1 - \phi)}{1 - \phi(1 - \chi_0)}, \end{aligned} \quad (4)$$

where γ_0 and χ_0 corresponds to the values of γ and χ when $K_f = 0$.

The EIAS model is consistent with the Hashin–Shtrikman bounds when applied to two-phase systems regardless of the pore shape spectrum. It has no restrictions on the crack density, since it includes interactions between cracks in some form. Endres & Knight (1997) also developed a dilute approximation given by their eqs (48)–(51). We refer to this dilute EIAS model as EIASD. Since both MJ and CPEM models assume a dilute concentration of cracks, the EIASD model is more suitable for comparison with these other models. The high-frequency wet moduli predicted by the EIASD model are

$$\begin{aligned} K_\infty &= \frac{K_s^2}{K_s + \phi(K_s - K_f)\gamma} \\ \mu_\infty &= \frac{\mu_s}{1 + \phi\chi}, \end{aligned} \quad (5)$$

where γ and χ are given in eq. (2). Taylor expansion of the right-hand side of eqs (1) and (5) in powers of ϕ shows that they coincide for $\phi \ll 1$.

2.2 The CPEM model

An alternative dispersion model was proposed by Adelinet *et al.* (2011), who also describe the pore space by a combination of spherical pores and penny-shaped cracks. Their high-frequency wet-rock moduli are given by

$$\frac{K_s}{K_\infty} = 1 + \phi_p \frac{3(1 - \nu_s)}{2(1 - 2\nu_s)} \left(\frac{\delta_p}{1 + \delta_p} \right) + \frac{16(1 - \nu_s^2)}{9(1 - 2\nu_s)} \left(\frac{\delta_c}{1 + \delta_c} \right) \epsilon \quad (6)$$

and

$$\frac{\mu_s}{\mu_\infty} = 1 + \phi_p \frac{15(1 - \nu_s)}{7 - 5\nu_s} + \left[\frac{16(1 - \nu_s)}{15(1 - 0.5\nu_s)} + \frac{32(1 - \nu_s)}{45} \left(\frac{\delta_c}{1 + \delta_c} \right) \right] \epsilon, \quad (7)$$

where $\phi_p = \phi(1 - c)$ is the stiff porosity,

$$\delta_p = \frac{2Y_s}{9(1 - \nu_s)} \left(\frac{1}{K_f} - \frac{1}{K_s} \right), \quad \delta_c = \frac{\pi Y_s a}{4(1 - \nu_s^2)} \left(\frac{1}{K_f} - \frac{1}{K_s} \right), \quad (8)$$

and

$$Y_s = \frac{9K_s\mu_s}{3K_s + \mu_s} \quad \text{and} \quad \nu_s = \frac{3K_s - 2\mu_s}{2(3K_s + \mu_s)} \quad (9)$$

are the mineral Young modulus and Poisson ratio, respectively. ϵ is the crack density defined by

$$\epsilon = \frac{3\phi_c}{4\pi a} = \frac{3\phi c}{4\pi a} \quad (10)$$

(Gurevich 2003, eq. 36), where $\phi_c = \phi c$ is the soft porosity.

The high-frequency dry-rock moduli, K_{m0} and μ_{m0} , can be obtained from eqs (6) and (7) by taking $\delta_p \rightarrow \infty$ and $\delta_c \rightarrow \infty$, so that $\delta_p/(1 + \delta_p) = 1$ and $\delta_c/(1 + \delta_c) = 1$. The low-frequency wet-rock moduli K_0 and μ_0 are given by Gassmann equations

$$K_0 = \frac{K_s - K_{m0} + \phi K_{m0} (K_s/K_f - 1)}{1 - \phi - K_{m0}/K_s + \phi K_s/K_f} \quad \text{and} \quad \mu_0 = \mu_{m0}, \quad (11)$$

where K_{m0} and μ_{m0} are the high-frequency dry-rock moduli previously obtained. Actually, the low- and high-frequency dry-rock moduli are identical (no dispersion in dry rock, Adelinet *et al.* 2011).

2.3 Mavko–Jizba moduli

Mavko & Jizba (1991) proposed a model for squirt dispersion in cracked rocks, where the main results are the so-called unrelaxed frame bulk and shear moduli, $K_{m\infty}$ and $\mu_{m\infty}$, obtained under an assumption that the stiff pores are dry but the soft (compliant) pores are filled with a fluid.

The unrelaxed frame bulk and shear moduli $K_{m\infty}$ and $\mu_{m\infty}$ are given by

$$\frac{1}{K_{m\infty}} \approx \frac{1}{K_h} + \left(\frac{1}{K_f} - \frac{1}{K_s} \right) \phi_c \quad (12)$$

and

$$\frac{1}{\mu_{m\infty}} = \frac{1}{\mu_{m0}} - \frac{4}{15} \left(\frac{1}{K_{m0}} - \frac{1}{K_{m\infty}} \right), \quad (13)$$

where K_h is the dry bulk modulus of the rock without soft porosity (without cracks).

However, the MJ model is only valid for liquid-saturated rocks. For rocks with much softer fluids (e.g. gas), Gurevich *et al.* (2009) generalized eq. (12) to

$$\frac{1}{K_{m\infty}} = \frac{1}{K_h} + \frac{1}{\frac{1}{\frac{1}{K_{m0}} - \frac{1}{K_h}} + \left(\frac{1}{K_f} - \frac{1}{K_s} \right) \phi_c}. \quad (14)$$

while shear modulus is given by the same eq. (13).

Then, the high-frequency wet-rock bulk and shear moduli are given by Gassmann equations,

$$K_\infty = \frac{K_s - K_{m\infty} + \phi K_{m\infty} (K_s/K_f - 1)}{1 - \phi - K_{m\infty}/K_s + \phi K_s/K_f} \quad \text{and} \quad \mu_\infty = \mu_{m\infty}. \quad (15)$$

Effectively, the unrelaxed frame consists of two 'minerals', the original mineral and the fluid in the cracks, but strictly speaking, this system is not actually Gassmann consistent and the full Brown–Korrington extension for mixed mineralogy should be used (Brown & Korrington 1975). Usually, this approach is impractical as there is no rigorous recipe to define the extra constant.

3 ANALYTICAL COMPARISON OF DISPERSION MODELS

In this section, we perform a detailed analytical comparison of the dispersion predicted by the three models and illustrate their similarities and differences. We first compare one of inclusion-based models, CPEM, against the MJG model, and then show that the moduli predicted by the two inclusion-based models are almost identical.

3.1 Comparison between the CPEM and MJG models

3.1.1 Bulk modulus

As discussed above, the MJG model relates the high-frequency modulus of the saturated rock to the dry-rock modulus of the same rock but without cracks. To obtain a similar relationship from the CPEM model, we note that the dry-rock bulk modulus K_{m0} can be obtained from eq. (6) by taking $\delta_p \rightarrow \infty$ and $\delta_c \rightarrow \infty$,

$$\frac{K_s}{K_{m0}} = \frac{K_s}{K_h} + \frac{16(1 - \nu_s^2)}{9(1 - 2\nu_s)} \epsilon, \quad (16)$$

where

$$\frac{K_s}{K_h} = 1 + \frac{3(1 - \nu_s)}{2(1 - 2\nu_s)} \phi_p. \quad (17)$$

Here, we have used the identity

$$\frac{16(1-\nu_s^2)}{9(1-2\nu_s)}\epsilon\delta_c = \frac{\phi_c Y_s}{3(1-2\nu_s)} \left(\frac{1}{K_f} - \frac{1}{K_s} \right) = \phi_c K_s \left(\frac{1}{K_f} - \frac{1}{K_s} \right). \quad (18)$$

which follows from the second eq. (8) and the definition of crack density (10).

The bulk modulus of the unrelaxed frame $K_{m\infty}$ can be obtained from eq. (6) by assuming that the stiff pores are dry, and hence $\delta_p \rightarrow \infty$,

$$\frac{K_s}{K_{m\infty}} = \frac{K_s}{K_h} + \frac{16(1-\nu_s^2)}{9(1-2\nu_s)}\epsilon \left(\frac{\delta_c}{1+\delta_c} \right). \quad (19)$$

or

$$\frac{K_s}{K_{m\infty}} = \frac{K_s}{K_h} + \left[\frac{1}{\frac{16(1-\nu_s^2)}{9(1-2\nu_s)}\epsilon} + \frac{1}{\frac{16(1-\nu_s^2)}{9(1-2\nu_s)}\epsilon\delta_c} \right]^{-1}. \quad (20)$$

Using eqs (16) and (18), eq. (20) becomes

$$\frac{1}{K_{m\infty}} = \frac{1}{K_h} + \frac{1}{\frac{1}{\left(\frac{1}{K_{m0}} - \frac{1}{K_h} \right)} + \frac{1}{\phi_c \left(\frac{1}{K_f} - \frac{1}{K_s} \right)}}. \quad (21)$$

This equation is identical to the MJG eq. (14) in form.

Rewriting eq. (6) as

$$\frac{K_s}{K_\infty} = 1 + \phi_p \frac{3(1-\nu_s)}{2(1-2\nu_s)} \left(\frac{\delta_p}{1+\delta_p} \right) + \left[\frac{1}{\frac{16(1-\nu_s^2)}{9(1-2\nu_s)}\epsilon} + \frac{1}{\frac{16(1-\nu_s^2)}{9(1-2\nu_s)}\epsilon\delta_c} \right]^{-1}, \quad (22)$$

we obtain

$$\frac{1}{K_\infty} = \frac{1}{K_h^{sat}} + \frac{1}{\frac{1}{\left(\frac{1}{K_{m0}} - \frac{1}{K_h} \right)} + \frac{1}{\phi_c \left(\frac{1}{K_f} - \frac{1}{K_s} \right)}}, \quad (23)$$

where K_h^{sat} is the bulk modulus of the fluid-saturated rock without soft porosity (without cracks),

$$\frac{K_s}{K_h^{sat}} = 1 + \phi_p \frac{3(1-\nu_s)}{2(1-2\nu_s)} \left(\frac{\delta_p}{1+\delta_p} \right). \quad (24)$$

Eqs (23) and (21) are similar. Indeed, the second terms in the right-hand sides of the two equations are identical. The difference is that eq. (21) is written for the unrelaxed frame, while eq. (23) is for the fully saturated medium. An approximate equivalence between these equations can be established by applying Gassmann equation to both sides of eq. (21). This is done in Appendix A, where we show that eq. (23) is consistent with Gassmann equation.

3.1.2 Shear modulus

The dry-rock shear modulus μ_{m0} can be obtained from eqs (7) by taking $\delta_c \rightarrow \infty$, so that $\delta_c/(1+\delta_c) \rightarrow 1$,

$$\frac{\mu_s}{\mu_{m0}} = 1 + \phi_p \frac{15(1-\nu_s)}{7-5\nu_s} + \left[\frac{16(1-\nu_s)}{15(1-0.5\nu_s)} + \frac{32(1-\nu_s)}{45} \right] \epsilon. \quad (25)$$

Subtracting this equation from eq. (7) gives

$$\frac{\mu_s}{\mu_\infty} - \frac{\mu_s}{\mu_{m0}} = -\frac{32(1-\nu_s)}{45} \frac{\epsilon}{\delta_c + 1}. \quad (26)$$

Similarly, for the bulk modulus, subtracting eq. (16) from eq. (19), we obtain

$$\frac{K_s}{K_{m\infty}} - \frac{K_s}{K_{m0}} = -\frac{16(1-\nu_s^2)}{9(1-2\nu_s)} \frac{\epsilon}{\delta_c + 1}. \quad (27)$$

Combining eqs (26) and (27) gives

$$\frac{1}{\mu_\infty} - \frac{1}{\mu_{m0}} = \frac{2K_s(1-2\nu_s)}{5\mu_s(1+\nu_s)} \left(\frac{1}{K_{m\infty}} - \frac{1}{K_{m0}} \right) \quad (28)$$

or

$$\frac{1}{\mu_\infty} = \frac{1}{\mu_{m0}} - \frac{4}{15} \left(\frac{1}{K_{m0}} - \frac{1}{K_{m\infty}} \right). \quad (29)$$

If the stiff pores are spherical, then the shear modulus of the rock without cracks is independent of the fluid compressibility, $\mu_\infty = \mu_{m\infty}$, and hence eq. (29) is identical to eq. (13).

3.1.3 Fluid effect in stiff pores

As discussed previously, if the stiff pores are spherical, the high-frequency limit wet-rock moduli predicted by the CPEM model are identical to those given by the MJG model. However, in real rocks, stiff pores are unlikely to have aspect ratio close to 1. More likely stiff pores could be approximated by spheroids with an aspect ratio a_s between 0.1 and 1 (or a range of aspect ratios). For bulk modulus, the KT approximation is consistent with Gassman equation for a dilute concentration of spheroidal pores of any single aspect ratio. Indeed, the Gassmann theory assumes that the fluid pressure is the same in all the pores. Even though the KT theory assumes that pores are isolated, bulk compression will induce the same fluid pressure in all the spheroidal pores. However if stiff pores are a mix of spheroids with more than one aspect ratio a_s (Zimmerman, 1991; Xu and White, 1995), the predictions of the KT and Gassmann equations will differ. In fact, the KT theory assumes that pores are isolated; hence the fluid pressure in pores of different aspect ratio will be different. Even if all pores are interconnected, in the high-frequency limit the fluid pressure will not have enough time to equilibrate, and hence in this limit the moduli should be consistent with the KT theory.

For the shear modulus, the high-frequency limit of the rock with stiff pores only computed using an effective medium theory (Kuster & Toksöz 1974; Berryman 1980) will deviate from the dry-rock modulus even when all of the stiff pores have a single aspect ratio $a_s \ll 1$. Indeed, this theory assumes that pores are isolated, and hence pressure induced by shear deformation in differently oriented spheroidal pores will be different. Thus, the resulting shear modulus will depend on the fluid compressibility unless all pores are spherical.

The high-frequency (or no-flow) limit predicted by the effective medium theory is only attained at frequencies above the characteristic frequency of squirt flow between stiff pores, $f_{sq} = a_s^3 \mu_s / \eta$ (here a_s refers to the characteristic aspect ratio of a range or distribution of aspect ratios of pores), where η is dynamic viscosity of the pore fluid (Jones 1986; Gurevich *et al.* 2010). For a water-saturated quartz sandstone and $a_s = 0.2$ and $f_{sq} \approx 3.5 \times 10^{11}$ Hz. Typical frequencies of ultrasonic rock-physics measurements are between 0.1 and 1 MHz, which are much smaller than f_{sq} . At these frequencies, fluid pressure will have ample time to equilibrate between stiff pores, and hence the moduli of the crack-free rock should be given by Gassmann equation. Hence, the contribution of stiff pores to the moduli should be computed with the Gassmann equation, as is done in the MJ and MJG models, rather than with any effective medium theory designed for isolated pores.

3.2 Comparison between the CPEM and EIASD models

The CPEM and MJG models are 'non-interactive', that is, the effect of the compliant pores (cracks) on the elastic compliances is linear in crack density (or crack porosity). Hence, strictly speaking, these models are only valid for a dilute crack concentration, although Grechka & Kachanov (2006) showed numerically that non-interactive models often provide reasonable approximations for crack densities as high as 0.2.

In contrast, the EIAS model attempts to account for interaction between cracks, and thus the effect of cracks on the rock compliance is non-linear. Thus, the EIAS model will only agree with the CPEM for a dilute concentration of cracks. Below, we compare the dispersion predicted by the CPEM and EIASD models.

3.2.1 Bulk modulus

For the bulk modulus of fluid-saturated rocks, we rewrite the EIASD model by Endres & Knight (1997, eq. 48) as

$$\frac{K_s}{K_\infty} = 1 + \frac{K_s - K_f}{K_s} (\phi_p P_1 + \phi_c P_2). \quad (30)$$

Substituting the pore-shape factor P_2 from the second eq. (3) gives

$$\frac{K_s}{K_\infty} = 1 + \phi_p \frac{K_s - K_f}{K_s} P_1 + \phi_c \frac{K_s - K_f}{K_f + \pi a \beta}. \quad (31)$$

On the other hand, the CPEM eq. (6) gives

$$\frac{K_s}{K_\infty} = 1 + \phi_p \left[\frac{1}{\frac{3(1-\nu_s)}{2(1-2\nu_s)} \delta_p} + \frac{1}{3(1-\nu_s)} \right]^{-1} + \left[\frac{1}{\frac{16(1-\nu_s^2)}{9(1-2\nu_s)} \epsilon_{\delta_c}} + \frac{1}{\frac{16(1-\nu_s^2)}{9(1-2\nu_s)} \epsilon} \right]^{-1}. \quad (32)$$

Furthermore, from eqs (8) and (9), we have

$$\begin{aligned}\frac{3(1-\nu_s)}{2(1-2\nu_s)}\delta_p &= \frac{3Y_s}{3(1-2\nu_s)}\left(\frac{1}{K_f}-\frac{1}{K_s}\right)=\frac{K_s-K_f}{K_f}, \\ \frac{3(1-\nu_s)}{2(1-2\nu_s)} &= \frac{3K_s+4\mu_s}{4\mu_s}, \\ \frac{16(1-\nu_s^2)}{9(1-2\nu_s)}\epsilon &= \frac{\phi_c K_s}{\pi a\beta}.\end{aligned}\quad (33)$$

Substituting eqs (18) and (33) into eq. (32) gives

$$\frac{K_s}{K_\infty}=1+\phi_p\frac{(K_s-K_f)}{K_s}P_1+\phi_c\frac{K_s-K_f}{K_f+\pi a\beta-\pi a\beta\frac{K_f}{K_s}}.\quad (34)$$

Eqs (31) and (34) differ by a term using the first-order Taylor expansion

$$\Delta=\phi_c\frac{K_s-K_f}{K_s}\frac{\pi a\beta K_f}{(K_f+\pi a\beta)^2}\quad (35)$$

For a small aspect ratio a , the difference in eq. (35) is always on the order of $a\phi_c$ and hence is negligible compared to the third term in eq. (31), which is always on the order of $\frac{a}{\phi_c}$. Thus, the EIASD and CPEM predictions for the bulk modulus are almost identical.

3.2.2 Shear modulus

For the shear modulus of fluid-saturated rocks, we rewrite the EIASD model by Endres & Knight (1997, their eq. 49) as

$$\frac{\mu_s}{\mu_\infty}=1+\phi\gamma=1+\phi_p Q_1+\phi_c Q_2.\quad (36)$$

Substituting the pore-shape factor Q_2 from eq. (3) gives

$$\frac{\mu_s}{\mu_\infty}=1+\phi_p Q_1+\frac{8\mu_s\phi_c}{5\pi a(\mu_s+2\beta)}+\frac{4}{15}\frac{\mu_s\phi_c}{K_f+\pi a\beta}\left(1+\frac{3}{2}\frac{K_f}{\mu_s}\right)+\frac{\phi_c}{5}.\quad (37)$$

On the other hand, the CPEM eq. (7) reads

$$\frac{\mu_s}{\mu_\infty}=1+\phi_p Q_1+\left[\frac{16(1-\nu_s)}{15(1-0.5\nu_s)}\epsilon+\frac{32(1-\nu_s)}{45}\epsilon\left(1+\frac{1}{\delta_c}\right)^{-1}\right].\quad (38)$$

Furthermore, from eqs (10) and $1-\nu_s=\mu_s/(2\beta)$, we have

$$\begin{aligned}\frac{16(1-\nu_s)}{15(1-0.5\nu_s)}\epsilon &= \frac{8\mu_s\phi_c}{5\pi a(\mu_s+2\beta)}, \\ \frac{32(1-\nu_s)}{45}\epsilon\left(1+\frac{1}{\delta_c}\right)^{-1} &= \frac{4}{15}\phi_c\mu_s\frac{K_s-K_f}{K_s(\pi a\beta+K_f)-K_f\pi a\beta}.\end{aligned}\quad (39)$$

Using the identities (39) in eq. (38) gives

$$\frac{\mu_s}{\mu_\infty}=1+\phi_p Q_1+\frac{8\mu_s\phi_c}{5\pi a(\mu_s+2\beta)}+\frac{4}{15}\mu_s\phi_c\frac{K_s-K_f}{K_s(\pi a\beta+K_f)-K_f\pi a\beta}.\quad (40)$$

If, as usually assumed, the aspect ratio a is small, then $\pi a\beta K_f\ll K_s K_f$, hence, eq. (40) reduces to

$$\frac{\mu_s}{\mu_\infty}=1+\phi_p Q_1+\frac{8\mu_s\phi_c}{5\pi a(\mu_s+2\beta)}+\frac{4}{15}\frac{\mu_s\phi_c}{K_f+\pi a\beta}\left(1-\frac{K_f}{K_s}\right).\quad (41)$$

Eqs (37) and (41) differ by a term

$$\Delta=\frac{\phi_c}{5}+\frac{4}{15}\frac{\mu_s\phi_c K_f}{K_f+\pi a\beta}\left(\frac{3}{2\mu_s}+\frac{1}{K_s}\right).\quad (42)$$

For a small aspect ratio a , the crack porosity is also small and hence the term $\phi_c/5$ is always negligible. Furthermore, the second term in the right-hand side of eq. (42) is on the order of $2\phi_c/3$ or smaller, and hence is also negligible. Thus the EIASD and CPEM predictions for the shear modulus are almost identical, with a relative difference on the order of the crack porosity.

The above analysis shows that the dispersion predicted by the three models (we compared the EIASD instead of the EIAS model for a dilute concentration of cracks) are almost identical with a very small difference. This consistency will be illustrated more clearly in the next section.

4 NUMERICAL COMPARISON OF DISPERSION MODELS

4.1 The dispersion index

Following eq. (B4), the bulk and shear dispersion indices are defined as

$$D_K = \frac{K_\infty - K_0}{2\sqrt{K_0 K_\infty}} \quad \text{and} \quad D_\mu = \frac{\mu_\infty - \mu_0}{2\sqrt{\mu_0 \mu_\infty}}. \quad (43)$$

respectively, and are directly related to the bulk and shear quality factors. These indices, inspired by the Zener model described in Appendix B, are similar to those defined by Endres & Knight (1997), that is $D = (M_\infty - M_0)/M_0$.

The P -wave dispersion index is

$$D_P = \frac{E_\infty - E_0}{2\sqrt{E_0 E_\infty}}, \quad (44)$$

where

$$E = K + \frac{4}{3} \mu. \quad (45)$$

The S -wave dispersion index is $D_S = D_\mu$.

Assuming that M is the P -wave modulus, a dispersion index for the P -wave velocity can be defined from eq. (B5) as

$$D_v = \frac{v_\infty}{v_0} - 1 \approx \frac{1}{Q_P} = D_P, \quad (46)$$

where Q_P is the P -wave quality factor. A similar equation for the S wave can be obtained.

4.2 Parametrization of the models

In the three models discussed above, the MJG and CPEM models assume a small crack density. In contrast, the EIAS model is not restricted to a small crack density as it includes the interaction between cracks in some form. Indeed, the approach of Endres & Knight (1997) ensures that the EIAS predictions are always within the Hashin–Shtrikman bounds. However inclusion interactions, and hence accuracy of the EIAS model, depend on crack size distribution and the spatial distribution of crack centres.

Hence, in order to illustrate the similarities and differences of the dispersion predicted by the three models, we first compare the EIAS model and its dilute approximation—EIASD model. We then present the results of the comparison of the EIASD, MJG and CPEM models. The aim in this step is to make their parameters consistent. To this end, we assume that the dry-rock moduli K_{m0} and μ_{m0} in the MJG model are given by eq. (5) of the EIASD model with $K_f = 0$. Also, K_h is the bulk modulus of the dry rock with pores only (no cracks) and hence should be given by the first of eq. (5) with

$$K_h = \frac{K_s}{1 + \phi_p P_1}, \quad (47)$$

with P_1 is given by the first eq. (3) and $K_f = 0$.

We assume that $K_s = \mu_s = 39$ GPa, $K_f = 2.25$ GPa (water) and $\phi = 0.1$. Numerical comparisons of the model predictions are presented in the next section.

4.3 Numerical results

The low- and high-frequency (a) bulk and (b) shear moduli predicted by the EIAS and EIASD models for $a = 0.001$ are displayed in Fig. 1. The pore fluid is water. As can be seen, the EIASD model gives an almost same dispersion range for bulk modulus with values shifted up compared to the EIAS model but a narrow dispersion range for shear modulus. The bulk dispersion predicted by the EIAS and EIASD models is much higher than the shear dispersion.

Fig. 2 shows the low- and high-frequency (a) bulk and (b) shear moduli of the water-saturated rocks predicted by the EIASD, MJG and CPEM models for $a = 0.001$. The normalized bulk and shear differences of the MJG and EIASD models relative to the CPEM model are presented in Figs 2(c) and (d). As can be observed, in all cases, the low-frequency (relaxed) moduli are lower than the high-frequency (unrelaxed) ones as expected (the dispersion index should be positive). At low frequencies, the EIASD and MJG models have the same predictions for bulk and shear moduli compared to those given by the CPEM model. At high frequencies, the EIASD has the same prediction for bulk modulus but a smaller prediction for shear modulus compared to those given by the CPEM model when the crack density is relatively high. Different from the performance of the EIASD model, the MJG model gives a higher prediction for the bulk modulus but a smaller prediction for the shear modulus compared to those given by the CPEM model when the crack density is relatively high. These behaviours are demonstrated more clearly in Figs 2(c) and (d), which are consistent with the previous analytical comparison in Section 4.2. The agreement between the three models is very good also for other aspect ratios.

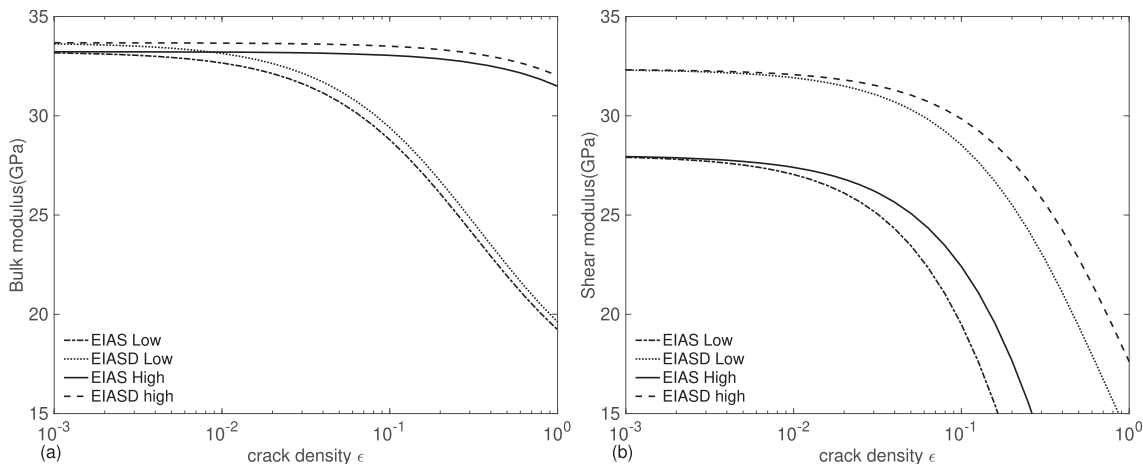


Figure 1. Comparison between the EIAS (dashed–dotted and solid lines) and EIASD (dotted and dashed lines) low- and high-frequency (a) bulk and (b) shear moduli as a function of the crack density and an aspect ratio $a = 0.001$. The fluid is water.

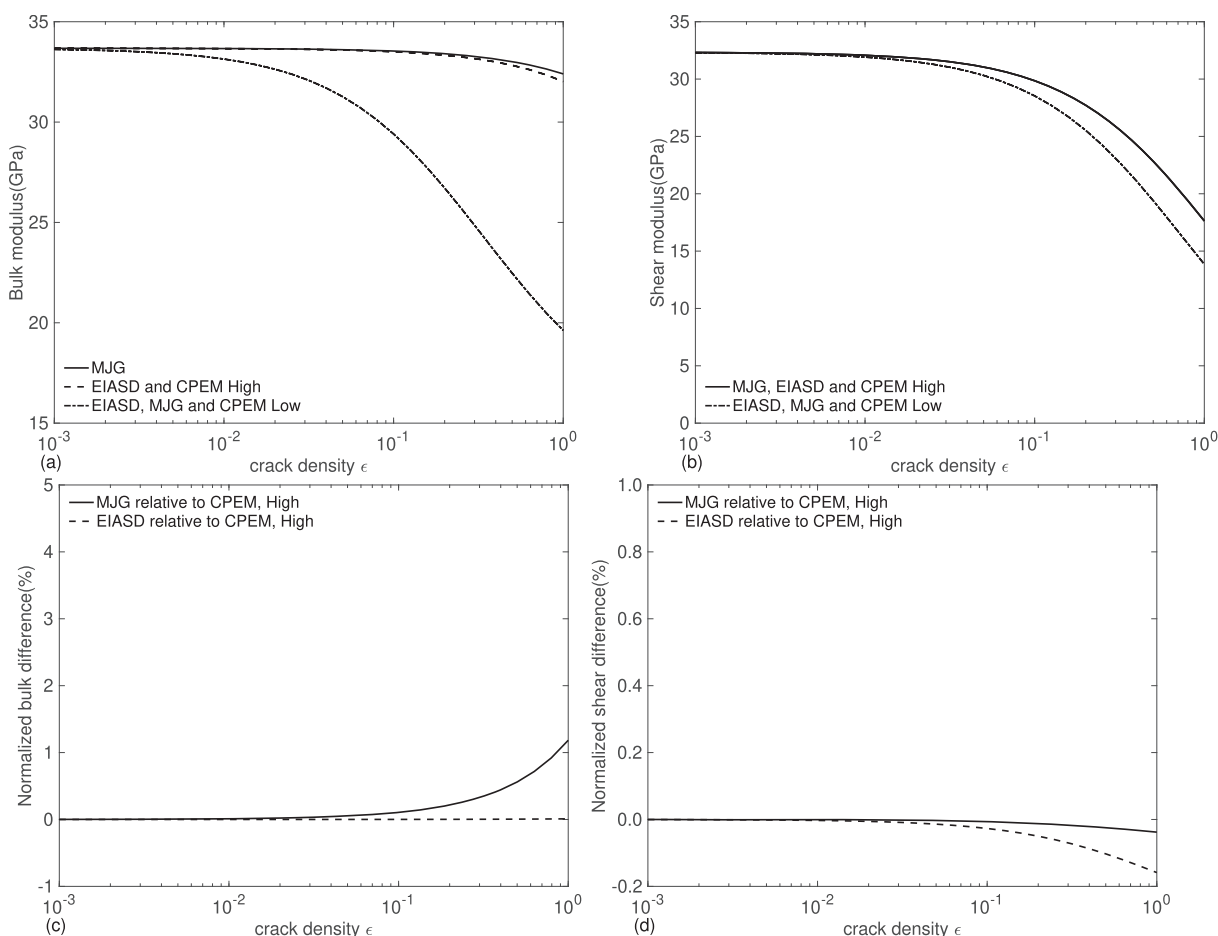


Figure 2. Comparison between the MJG, EIASD and CPEM low- and high-frequency (a) bulk and (b) shear moduli as a function of the crack density and an aspect ratio $a = 0.001$. (c) and (d) correspond to the normalized bulk and shear differences of the MJG and EIASD models in high-frequency limits relative to those given by the CPEM model. The fluid is water.

Fig. 3 shows the (a) bulk and (b) shear dispersion indices predicted by the MJG model when the fluid is water, compared to those of the EIASD model. The differences at relatively high crack density, from a practical point of view, are actually small. Basically, the dispersion (and attenuation) increases with increasing crack density and decreases with increasing aspect ratio. Aspect ratios equal or greater than 0.1 show very weak attenuation, with bulk and shear quality factors $Q > 1/10^{-3} \approx 1000$. Although strictly not applicable due to the non-interaction assumption, it can be shown that for $\epsilon > 0.3$ all the three models show a very good agreement. Figs 3(c) and (d) show the same data displayed

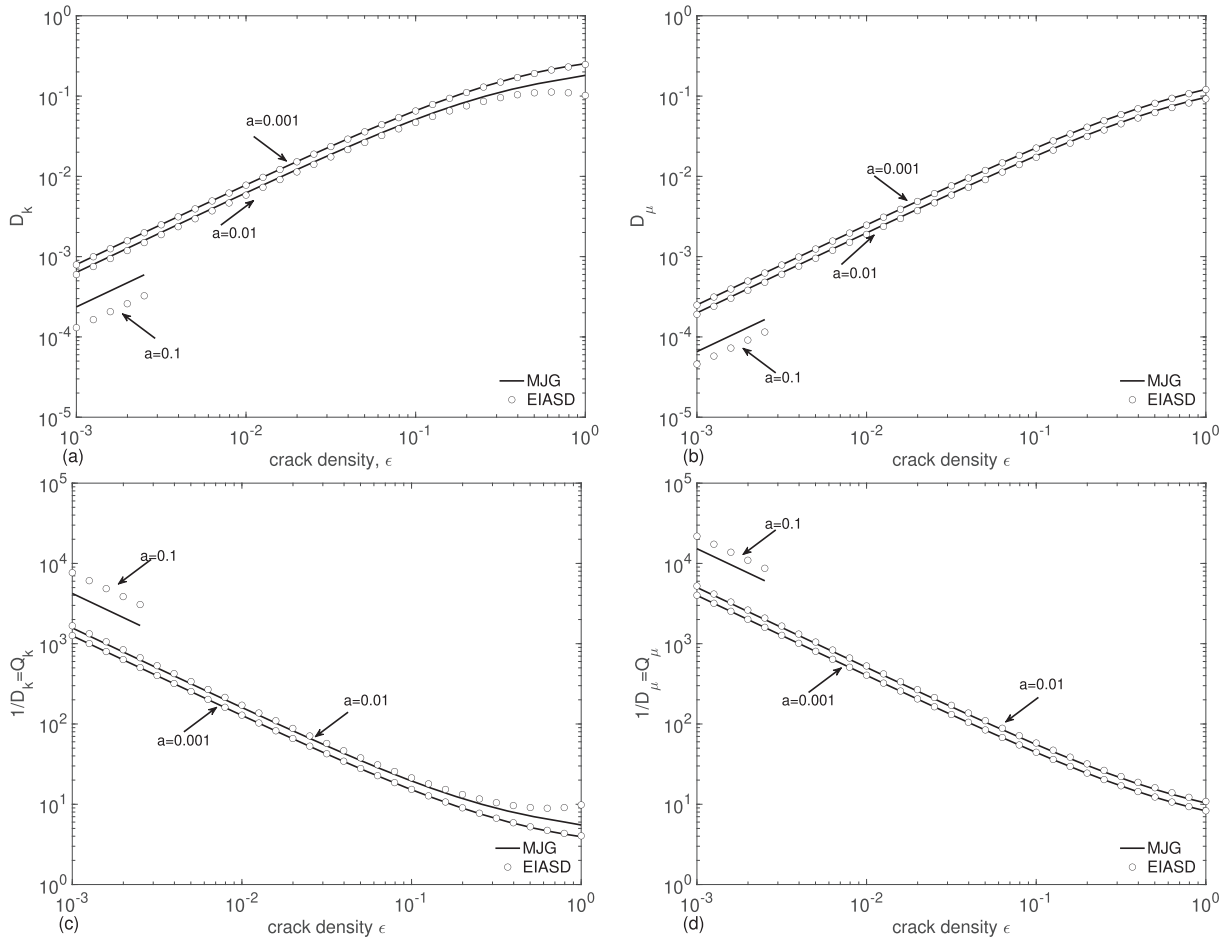


Figure 3. (a) and (b) Comparison between the EIASD (circles) and MJG (lines) bulk and shear dispersion indices and (c) and (d) their Zener quality factors as a function of the crack density and three values of the aspect ratio a . The fluid is water.

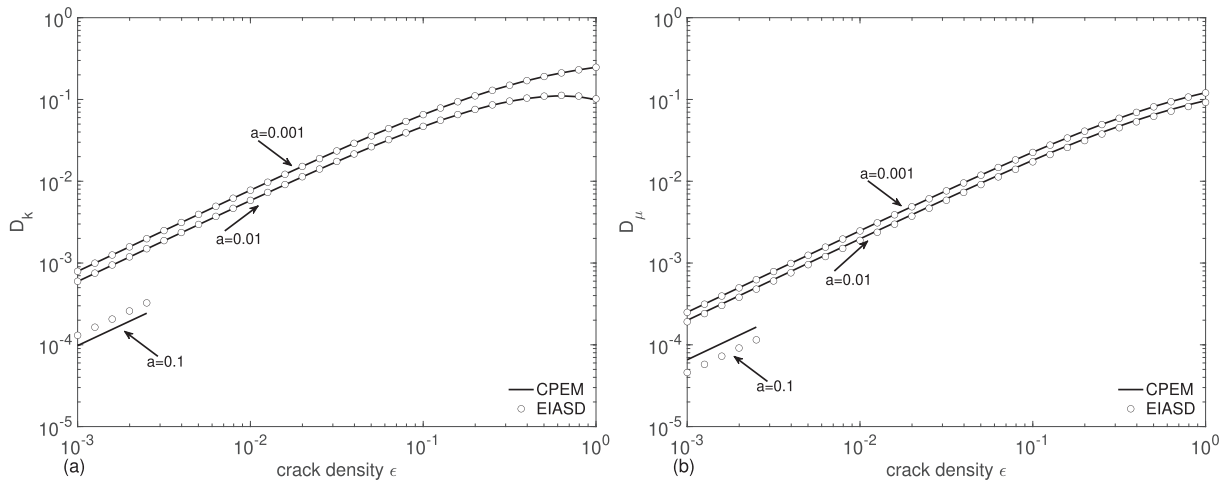


Figure 4. Comparison between the EIASD (circles) and CPEM (lines) (a) bulk and (b) shear dispersion indices as a function of the crack density and three values of the aspect ratio. The fluid is water.

in Figs 3(a) and (b), but in terms of the Zener quality factor, where it can clearly be seen that attenuation is higher for the smaller aspect ratio, that is a higher dispersion index.

Fig. 4 compares the (a) bulk and (b) shear dispersion indices estimated from the EIASD and CPEM models. As can be seen, the two models yield very similar values, showing the consistency of the results by using two different theoretical approaches.

Fig. 5 compares the (a) bulk and (b) shear dispersion indices by using the MJG (solid and dash lines) and (open circles and squares) MJ models when the fluid is gas, with $K_f = 0.01$ GPa, which roughly corresponds to methane at a pore pressure of 30 MPa and a depth of

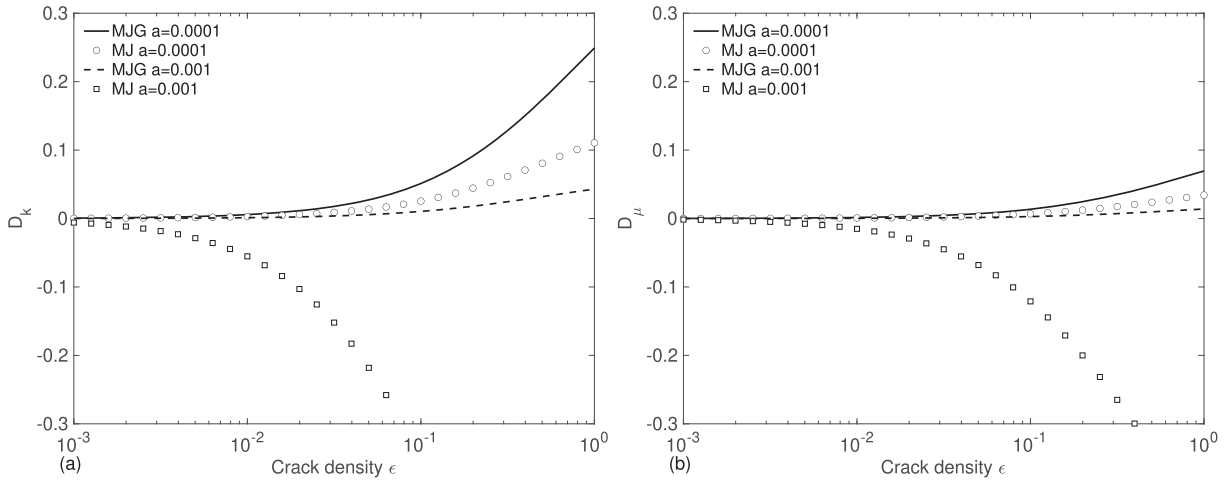


Figure 5. Comparison between the MJG (solid and dash lines) and original MJ (open circles and squares) (a) bulk and (b) shear dispersion indices as a function of crack density and two values of the aspect ratio. The fluid is gas. The open squares with $a = 10^{-3}$ represent unphysical values, since the dispersion index is negative.

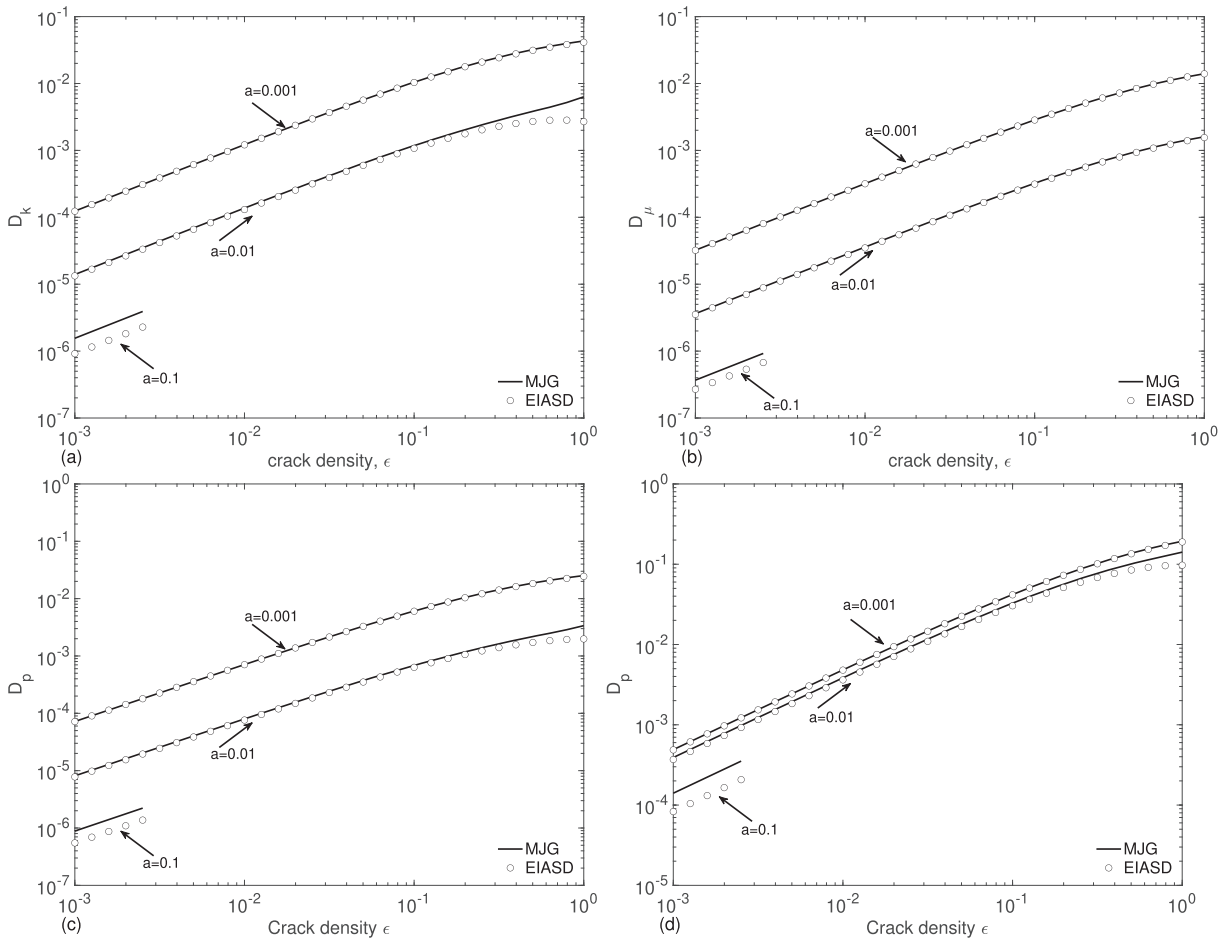


Figure 6. Comparison between the EIASD (circles) and MJG (lines) (a) bulk, (b) shear and (c) P -wave dispersion indices as a function of crack density and three values of the aspect ratio. The fluid is gas. Part (d) is the P -wave dispersion indices for water-saturated condition.

3 km. As can be seen, the MJ model cannot be used for relatively high aspect ratios (e.g. say $a > 10^{-4}$), since it yields negative values of the dispersion index. This confirms the recognition that the original MJ model is valid only for liquid (Gurevich *et al.* 2009). Anelasticity for gas is weaker compared to water, that is for $\epsilon = 0.1$ and $a = 0.001$ the bulk quality factor is approximately 96 in Fig. 5(a, dash line), whereas it is 15 in Fig. 3(a).

Fig. 6 shows the (a) bulk, (b) shear and (c) P -wave dispersion indices of the MJG model (open circles) when the fluid is gas, compared to those of the EIASD model (solid lines). Dispersion and attenuation is lower than for water-saturated rocks (Fig. 3), and is significant only

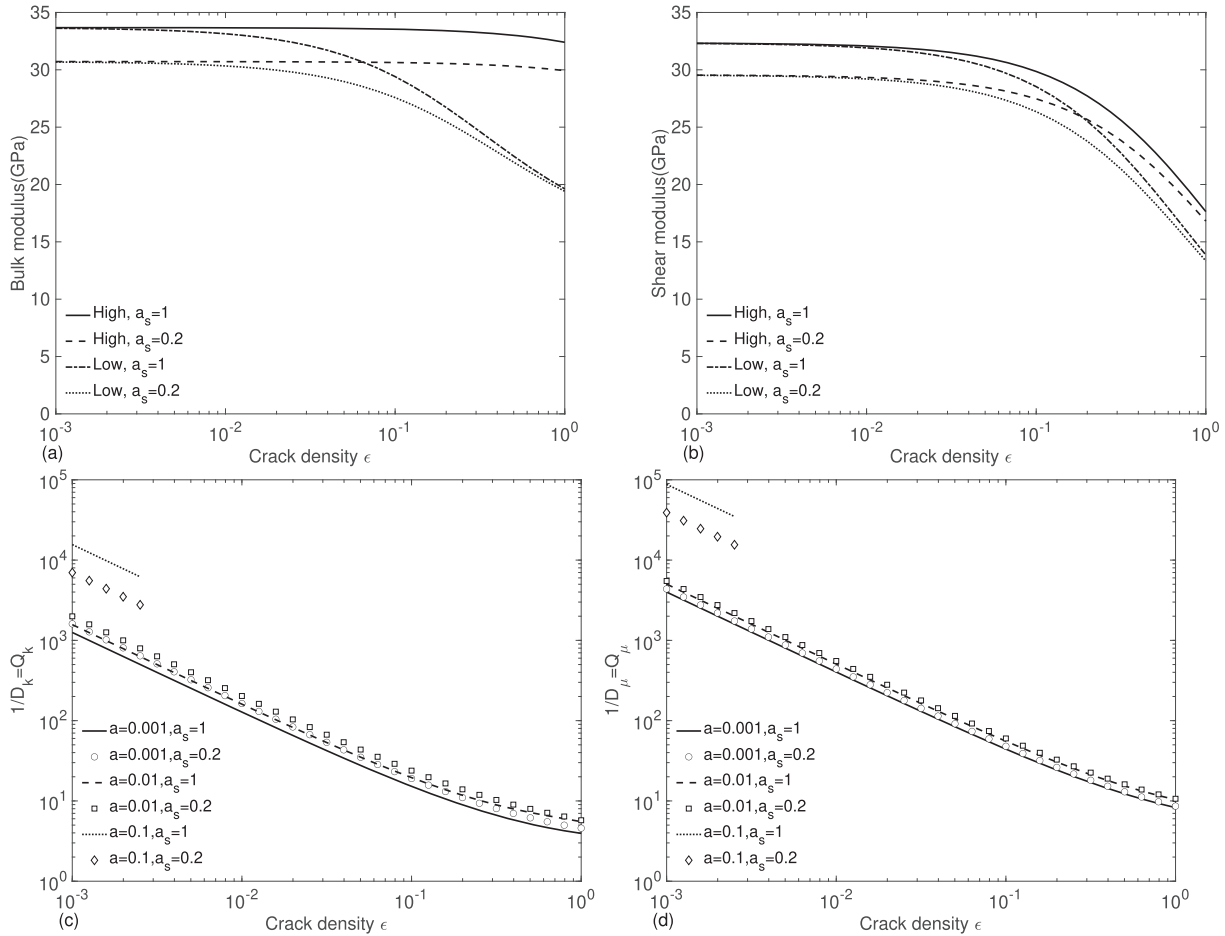


Figure 7. Effect of the aspect ratio of the stiff pores, a_s , on the low (relaxed) and high (unrelaxed) (a) bulk and (b) shear moduli and (c) bulk and (d) shear quality factors. The aspect ratio of the cracks in (a) and (b) is $a = 10^{-3}$ and the fluid is water. The model is based on the MJG relations.

at low aspect ratios and high crack density. Fig. 6(d) shows the P -wave indices of the MJG model when the fluid is water, compared to those of the EIASD model. It shows similar characteristics as those of Fig. 6(c), with higher bulk and shear dispersion indices. It can be shown that the dispersion index of the P -wave velocity [eq. (46)] is almost identical to that of the P -wave modulus E for $Q_p \gg 1$ (not shown).

It should be noted that the above comparisons are based on the assumption that the stiff pores are spherical. In real rocks stiff pores may have a lower aspect ratio, for example lie in a range $0.1 < a < 1$. For stiff pores in a shape of an oblate spheroid with an aspect ratio $a_s \leq 1$, the coefficients P_1 and Q_1 in the first and third eqs (3) are

$$P_1 = \frac{1}{3} T_{ijij}, \quad \text{and} \quad Q_1 = \frac{1}{5} (T_{ijij} - P_1), \quad (48)$$

where T_{ijij} and T_{ijij} are given in appendix A of Berryman (1980) or in Mavko et al. (2009, p. 189, the inclusion moduli should be taken equal to zero).

The effect of the aspect ratio of the stiff pores on the (a) and (b) bulk and shear moduli and (c) and (d) Zener quality factor is illustrated in Fig. 7. We compare the MJG results for spherical stiff pores ($a_s = 1$) and oblate spheroidal stiff pores ($a_s = 0.2$). The fluid is water. As can be observed, at constant crack density the dispersion and attenuation are weaker for decreasing aspect ratio of the stiff pores, and the low-frequency (relaxed) moduli are the same at high crack density. Fig. 8 compares the MJG and EIASD models for $a_s = 0.2$. Both the moduli and quality factors (and dispersion indices as a consequence) are similar. Similar behaviours are obtained for the bulk and shear moduli.

5 CONCLUSIONS

We have performed a comparative analysis of Zener-based dispersion indices obtained with the generalized Mavko–Jizba relations, and two inclusion-based models that incorporate pore geometry and fluid pressure communication to model the elastic behaviour of porous rocks. The inclusion-based models are based on a combination of stiff (equant) pores and penny-shaped cracks. The low-frequency moduli correspond to full fluid pressure equilibration between cracks and pores, whereas at high frequencies, the cracks are hydraulically isolated from pores. The difference between these two conditions results in significant moduli and velocity dispersion.

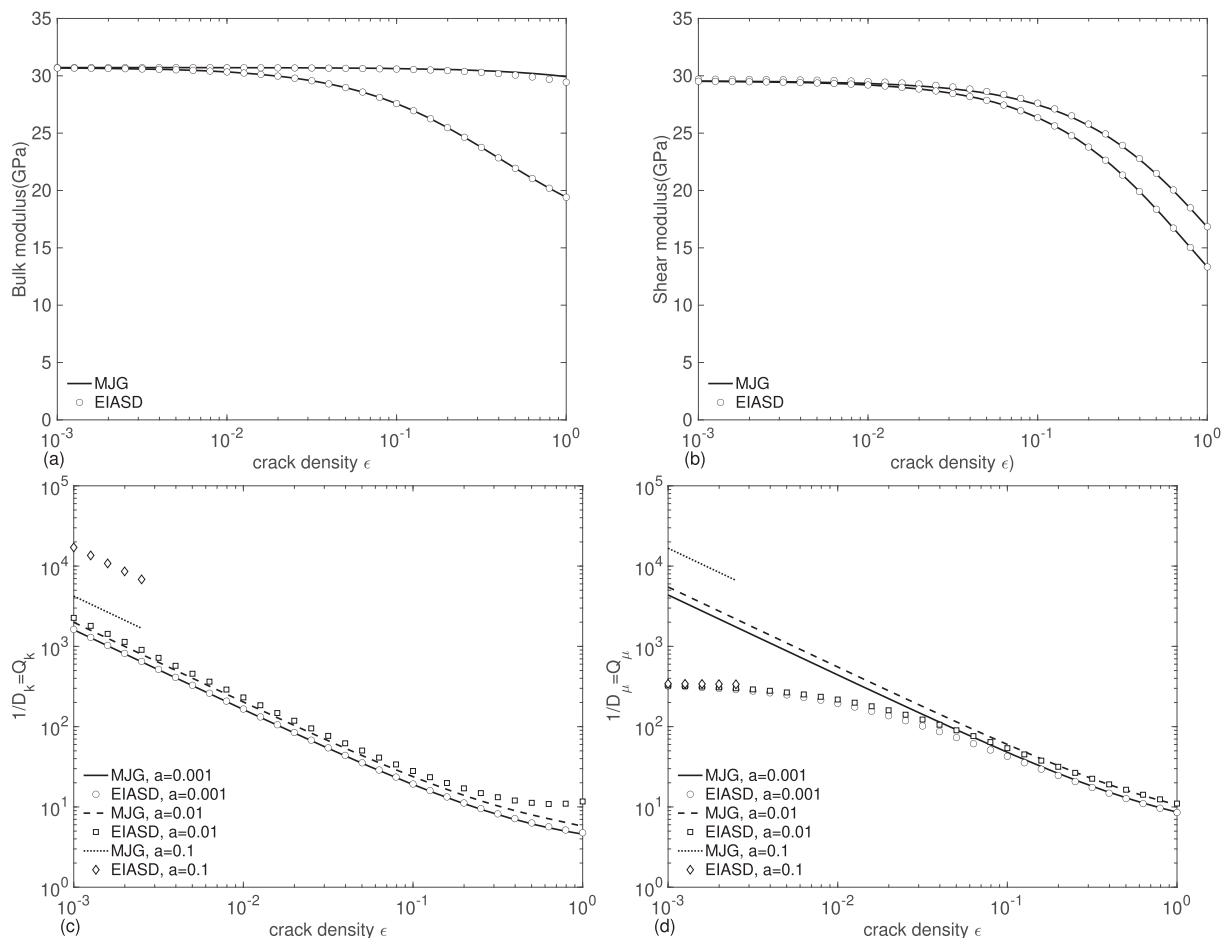


Figure 8. Comparison between the EIASD (symbols) and MJG (lines) (a) bulk, (b) shear moduli and (c) bulk and (d) shear quality factors as a function of crack density and three values of the aspect ratio. The aspect ratio of the stiff pores is $a_s = 0.2$ and the aspect ratio of the cracks in (a) and (b) is $a = 10^{-3}$. The fluid is water.

As demonstrated by the numerical comparisons, such dispersion (and attenuation) increases with crack density and decreases with increasing aspect ratio. Bulk modulus dispersion and attenuation are stronger than those for shear deformations. Aspect ratios equal or greater than 0.1 show very weak attenuation. Both analytical and numerical comparisons show that the three models yield very similar values, showing the consistency of the results by using two idealized theoretical approaches (EIASD and CPEM) compared to the MJG relations. Anelasticity for gas-saturated rocks is weaker than for liquid saturation. The dispersion indices can be viewed as a template to obtain the crack properties from low- and high-frequency velocity measurements.

Theoretical analysis and numerical examples show that when stiff pores are spherical and crack density is small, the predictions of all the models considered are almost identical. However when stiff pores are oblate spheroids with an aspect ratio less than 1 (say between 0.2 and 1), the high-frequency moduli predicted by inclusion-based models are considerably higher than the predictions of the MJG model. This is because the inclusion-based models assume that at high frequencies the pores are hydraulically isolated from each other, and hence correspond to the true high-frequency limit, which is attained at frequencies of 10^9 Hz or higher, which are irrelevant for measurements on rocks. In contrast, in the MJG model, the effect of stiff pores is modelled with Gassmann's theory, and hence its high-frequency limit corresponds to a case where pores are assumed disconnected from cracks, but interconnected with each other. Our analysis shows that these assumptions of the MJG model hold at ultrasonic frequencies on the order of 10^6 Hz. The two inclusion based models can be easily made consistent with the MJG model by accounting for the effect of fluid in stiff pores using Gassmann's theory.

Since predictions of all the three models are very similar, the preference for one model or another is a matter of convenience. When the specific pore space geometry is known or assumed, the inclusion based models would be preferred (but the effect of fluid in stiff pores should be treated with Gassmann's theory). Of the inclusion-based model, the non-interactive models are simpler and hence preferred when the crack density is low, but the EIAS model must be used for high crack densities. Conversely, when not much is known about pore geometry, the MJG model would be the most logical choice.

ACKNOWLEDGEMENTS

The authors thank the financial support from the Curtin Reservoir Geophysics Consortium (CRGC) and the China Scholarship Council (CSC). The authors thank Yves Guéguen and an anonymous reviewer for their careful reading of our manuscript and many insightful comments and suggestions.

REFERENCES

- Adelinet, M., Fortin, J. & Guéguen, Y., 2011. Dispersion of elastic moduli in a porous-cracked rock: theoretical predictions for squirt-flow, *Tectonophysics*, **503**(1), 173–181.
- Alkhimenkov, Y., Caspari, E., Gurevich, B., Barbosa, N.D., Glubokovskikh, S., Hunziker, J. & Quintal, B., 2020. Frequency-dependent attenuation and dispersion caused by squirt flow: three-dimensional numerical study, *Geophysics*, **85**(3), 129–145.
- Berryman, J.G., 1980. Long-wavelength propagation in composite elastic media II. Ellipsoidal inclusions, *J. acoust. Soc. Am.*, **68**(6), 1820–1831.
- Biot, M.A., 1962. Mechanics of deformation and acoustic propagation in porous media, *J. appl. Phys.*, **33**(4), 1482–1498.
- Brown, R.J.S. & Korrington, J., 1975. On the dependence of the elastic properties of a porous rock on the compressibility of the pore fluid, *Geophysics*, **40**(4), 608–616.
- Carcione, J.M., 2014. *Wave Fields in Real Media: Theory and Numerical Simulation of Wave Propagation in Anisotropic, Anelastic, Porous and Electromagnetic Media*, Elsevier.
- Carcione, J.M. & Gurevich, B., 2011. Differential form and numerical implementation of Biot's poroelasticity equations with squirt dissipation, *Geophysics*, **76**(6), N55–N64.
- Carcione, J.M., Cavallini, F., Ba, J., Cheng, W. & Qadrouh, A.N., 2019. On the Kramers–Kronig relations, *Rheol. Acta*, **58**(1), 21–28.
- Chapman, M., Zatsepin, S.V. & Crampin, S., 2002. Derivation of a microstructural poroelastic model, *Geophys. J. Int.*, **151**(2), 427–451.
- Dvorkin, J., Mavko, G. & Nur, A., 1995. Squirt flow in fully saturated rocks, *Geophysics*, **60**(1), 97–107.
- Endres, A.L. & Knight, R.J., 1997. Incorporating pore geometry and fluid pressure communication into modeling the elastic behavior of porous rocks, *Geophysics*, **62**(1), 106–117.
- Eshelby, J.D., 1957. The determination of the elastic field of an ellipsoidal inclusion, and related problems, *Proc. Roy. Soc. London. Ser. A*, **241**(1226), 376–396.
- Gassmann, F., 1951. Über die Elastizität poröser Medien, *Veiertel. Naturforsch. Ges. Zürich*, **96**, 1–23.
- Grechka, V. & Kachanov, M., 2006. Effective elasticity of fractured rocks, *Leading Edge*, **25**(2), 152–155.
- Gurevich, B., 2003. Elastic properties of saturated porous rocks with aligned fractures, *J. appl. Geophys.*, **54**(3), 203–218.
- Gurevich, B., Makarynska, D. & Pervukhina, M., 2009. Ultrasonic moduli for fluid-saturated rocks: Mavko–Jizba relations rederived and generalized, *Geophysics*, **74**(4), N25–N30.
- Gurevich, B., Makarynska, D., de Paula, O.B. & Pervukhina, M., 2010. A simple model for squirt-flow dispersion and attenuation in fluid-saturated granular rocks, *Geophysics*, **75**(6), N109–N120.
- Jones, T., 1986. Pore fluids and frequency-dependent wave propagation in rocks, *Geophysics*, **51**(10), 1939–1953.
- Kachanov, M., 1993. Elastic solids with many cracks and related problems, in *Advances in applied mechanics*, Vol. **30**, pp. 259–445, Elsevier.
- Kuster, G.T. & Toksöz, M.N., 1974. Velocity and attenuation of seismic waves in two-phase media: Part I. Theoretical formulations, *Geophysics*, **39**(5), 587–606.
- Mavko, G. & Jizba, D., 1991. Estimating grain-scale fluid effects on velocity dispersion in rocks, *Geophysics*, **56**(12), 1940–1949.
- Mavko, G. & Nur, A., 1975. Melt squirt in the asthenosphere, *Geophys. J. Int.*, **80**(11), 1444–1448.
- Müller, T.M., Gurevich, B. & Lebedev, M., 2010. Seismic wave attenuation and dispersion resulting from wave-induced flow in porous rocks—a review, *Geophysics*, **75**(5), 75A147–75A164.
- Murphy, W.III, Winkler, K. & Kleinberg, R., 1986. Acoustic relaxation in sedimentary rocks—dependence on grain contacts and fluid saturation, *Geophysics*, **51**(3), 757–766.
- O'Connell, R.J. & Budiansky, B., 1977. Viscoelastic properties of fluid-saturated cracked solids, *J. geophys. Res.*, **82**(36), 5719–5735.
- Palmer, I. & Traviola, M., 1980. Attenuation by squirt flow in undersaturated gas sands, *Geophysics*, **45**(12), 1780–1792.
- Pride, S.R., Berryman, J.G. & Harris, J.M., 2004. Seismic attenuation due to wave-induced flow, *J. geophys. Res.*, **109**(B1), doi:10.1029/2003JB002639.
- Walsh, J.B., 1965. The effect of cracks on the compressibility of rock, *J. geophys. Res.*, **70**(2), 381–389.
- Zhang, L., Ba, J., Carcione, J.M. & Sun, W., 2019a. Modeling wave propagation in cracked porous media with penny-shaped inclusions, *Geophysics*, **84**(4), WA141–WA151.
- Xu, S. & White, R.E., 1995. A new velocity model for clay-sand mixtures 1, *Geophys. Prospect.*, **43**(1), 91–118.
- Zhang, L., Ba, J., Fu, L., Carcione, J.M. & Cao, C., 2019b. Estimation of pore microstructure by using the static and dynamic moduli, *Int. J. Rock Mech. Min.*, **113**, 24–30.
- Zimmerman, R.W., 1991. *Compressibility of Sandstones*, Elsevier, Amsterdam.

APPENDIX A: WET-ROCK BULK MODULUS BASED ON THE UNRELAXED MJG MODULUS

To verify if eqs (23) and (14) are equivalent, we need to rewrite eq. (23) for a saturated medium. A wet-rock modulus K_∞ for a medium with a high-frequency unrelaxed bulk modulus $K_{m\infty}$, is given by the Gassmann equation

$$K_\infty = K_{m\infty} + K_h S(K_{m\infty}), \quad (\text{A1})$$

where $S(K_{m\infty}) = \alpha^2 M / K_h$, $\alpha = 1 - K_{m\infty} / K_s$ and $M = K_s / [(1 - K_{m\infty} / K_s) / K_s - \phi(1 - K_s / K_f)]$ (e.g. Carcione 2014).

We know that for most rocks $K_f \ll K_m$ and hence the Gassmann correction to the unrelaxed modulus [the second term in the right-hand side of eq. (A1)] is small compared to the first term. We can make this fact explicit by introducing a small parameter δ into eq. (A1),

$$K_\infty = K_{m\infty} + \delta K_h S(K_{m\infty}). \quad (\text{A2})$$

Note also that by construction the second term in the right-hand side of eq. (14) is very small, so that we can write

$$K_{m\infty} \approx K_h (1 + \varepsilon_h). \quad (\text{A3})$$

where $\varepsilon_h = K_h \phi_c (1/K_s - 1/K_f) \ll 1$. Substitution of eq. (A3) into eq. (A2) gives

$$K_\infty = K_h (1 + \varepsilon_h + \delta S [K_h (1 + \varepsilon_h)]). \quad (\text{A4})$$

Expanding $S[K_h (1 + \varepsilon_h)]$ in powers of ε_h yields

$$K_\infty = K_h (1 + \varepsilon_h + \delta [(S(K_h) + \varepsilon_h S_1)]), \quad (\text{A5})$$

or

$$K_\infty = K_h (1 + \varepsilon_h + \delta S(K_h) + \delta \varepsilon_h S_1). \quad (\text{A6})$$

The last term in eq. (A6) contains a product of two small parameters and hence can be neglected, thus eq. (A6) reduces to

$$K_\infty = K_h [1 + \varepsilon_h + \delta S(K_h)]. \quad (\text{A7})$$

Considering $K_h^{\text{sat}} = K_h [1 + \delta S(K_h)]$, eq. (A7) simplifies to

$$K_\infty = K_h^{\text{sat}} + \varepsilon_h K_h = K_h^{\text{sat}} \left(1 + \varepsilon_h \frac{K_h}{K_h^{\text{sat}}} \right). \quad (\text{A8})$$

Similar to ε_h , we define $\varepsilon_h^{\text{sat}} = K_h^{\text{sat}} \phi_c (1/K_s - 1/K_f) \ll 1$ and obtain

$$K_\infty = K_h^{\text{sat}} \left(1 + \varepsilon_h \frac{K_h}{K_h^{\text{sat}}} \right) = K_h^{\text{sat}} \left[1 + \varepsilon_h^{\text{sat}} \left(\frac{K_h}{K_h^{\text{sat}}} \right)^2 \right]. \quad (\text{A9})$$

Since $\varepsilon_h^{\text{sat}} \ll 1$ and $K_h/K_h^{\text{sat}} \approx 1 - \delta S(K_h)$, eq. (A9) reduces to

$$K_\infty = K_h^{\text{sat}} (1 + \varepsilon_h^{\text{sat}}). \quad (\text{A10})$$

Eq. (A10) approximates to eq. (23).

APPENDIX B: THE ZENER MODEL

A classical model of viscoelastic behaviour is the Zener model, which is defined by the complex modulus

$$M(\omega) = M_\infty - \frac{M_\infty - M_0}{1 + i\omega\tau}, \quad (\text{B1})$$

where ω is the angular frequency, τ is a relaxation time, $M_0 = M(0)$ and $M_\infty = M(\infty)$ are the relaxed and unrelaxed moduli (low and high frequencies, respectively), $i = \sqrt{-1}$, and $M_\infty \geq M_0$ holds (e.g. Carcione 2014). The Zener model satisfies the Kramers–Kronig relations (e.g. Carcione *et al.* 2019). Function $(M - M_\infty)(\omega)$ has a unique pole in the upper half ω -plane, that is, at i/ω and therefore it is analytic in the lower half ω -plane as required by causality. Its inverse time Fourier transform is causal and smooth for $t > 0$, since it is basically an exponential function of time.

The quality factor is defined as

$$Q(\omega) = \frac{M_R}{M_I} = \frac{M_0 + M_\infty(\omega\tau)^2}{\omega\tau(M_\infty - M_0)} \quad (\text{B2})$$

(e.g. Carcione 2014, p. 91) which has the minimum value

$$Q_0 = \frac{2\sqrt{M_\infty M_0}}{M_\infty - M_0} = \frac{2v_\infty v_0}{v_\infty^2 - v_0^2} \quad (\text{B3})$$

(Carcione 2014, p. 96), where we have defined the phase velocities at zero and infinite frequency as v_0 and v_∞ , such that $M_0 = \rho v_0^2$ and $M_\infty = \rho v_\infty^2$, where ρ is the mass density.

Let us define the Zener dispersion index as the inverse of the minimum quality factor, or dissipation factor, as

$$D = \frac{1}{Q_0} = \frac{M_\infty - M_0}{2\sqrt{M_\infty M_0}} = \frac{v_\infty^2 - v_0^2}{2v_\infty v_0} \quad (\text{B4})$$

It is easy to show that the amount of velocity dispersion is

$$\Delta v = v_\infty - v_0 = v_0 \left(Q_0^{-1} + \sqrt{1 + Q_0^{-2}} - 1 \right) \approx \frac{v_0}{Q_0}, \quad (\text{B5})$$

where the approximation holds for low-loss solids ($Q_0 \gg 1$). This is a simple relation between the maximum velocity dispersion and the minimum Q (higher attenuation). The Kramers–Kronig relations are more general and reflect the fact that if velocity dispersion is known for all frequencies then Q is known for all frequencies and vice versa.

2.2 Modelling the effect of pressure on the moduli dispersion in fluid-saturated rocks

Modeling the Effect of Pressure on the Moduli Dispersion in Fluid-Saturated Rocks

Yongyang Sun¹  and Boris Gurevich¹ ¹Centre for Exploration Geophysics, Curtin University, Perth, WA, Australia**Key Points:**

- A micromechanical model of wave-induced fluid pressure relaxation is incorporated into pressure dependency of elastic moduli of porous rocks
- The resulting equation expresses elastic wave dispersion and attenuation in porous rock as functions of effective pressure
- The model predictions show reasonable agreement with laboratory data measured using ultrasonic and forced oscillation techniques

Correspondence to:Y. Sun,
yongyang.sun@postgrad.curtin.edu.au**Citation:**Sun, Y., & Gurevich, B. (2020). Modeling the effect of pressure on the moduli dispersion in fluid-saturated rocks. *Journal of Geophysical Research: Solid Earth*, 125, e2019JB019297. <https://doi.org/10.1029/2019JB019297>

Received 1 JAN 2020

Accepted 8 JUL 2020

Accepted article online 11 JUL 2020

Abstract Laboratory experiments of ultrasonic velocities of fluid-saturated rocks are often much higher than the predictions of the Gassmann theory. This difference is usually attributed to the velocity dispersion caused by fluid pressure relaxation between pores of different shapes and orientation. This paper proposes a simple model to characterize pressure and frequency effects on the elastic moduli of fluid-saturated rocks in a broad frequency range. The proposed model incorporates micromechanics of wave-induced fluid pressure relaxation at grain contacts (between crack-like contacts and stiff pores) into pressure dependency of elastic moduli. Previously, the pressure dependency of the velocities or elastic moduli was ascribed to the progressive closure of cracks with the increasing effective pressure and expressed as an integral of crack compliance over the range of aspect ratios. For isolated cracks, this compliance is a function of crack geometry only. For cracks hydraulically connected to stiff pores, this crack compliance can be replaced by a frequency-dependent solution of the micromechanical problem of fluid pressure relaxation between a single crack and surrounding pores. The resulting equation expresses the bulk and shear moduli of the fluid-saturated rock as functions of both pressure and frequency. Furthermore, if pressure-dependent moduli of both dry and fluid-saturated moduli are known, the aspect ratio distribution can be obtained from the pressure dependency of the dry moduli, and then the saturated moduli can be computed with no adjustable parameters. The model predictions show reasonable agreement with laboratory data measured using ultrasonic and forced oscillation techniques.

1. Introduction

Elastic wave velocities and corresponding elastic moduli of fluid-saturated rocks often exhibit frequency dependency due to the wave flow between pores of different shapes and orientations (Borgomano et al., 2019; Chapman et al., 2019; Jones, 1986; Mavko & Nur, 1975; Mikhaltsevitch et al., 2015; O'Connell & Budiansky, 1977; Pimienta et al., 2017; Winkler, 1986). At low frequencies, the fluid pressure is spatially uniform throughout the pore space, and hence, the effective elastic moduli of fluid-saturated rocks satisfy the Gassmann (1951) theory. At higher frequencies, the fluid pressure does not have enough time to equilibrate within one period of the wave, and hence, the grain contacts become stiffer. This, in turn, causes the elastic moduli to increase and no longer fit the Gassmann theory (Gurevich et al., 2009b; Mavko & Jizba, 1991; Wulff & Burkhardt, 1997). Expressions for high-frequency moduli have been derived by Mavko and Jizba (1991) (referred to as MJ model) and generalized by Gurevich et al. (2009b). The elastic moduli at intermediate frequencies lie between the low- and high-frequency regimes, but their prediction is nonunique as they depend on the distribution of cracks shapes and orientations.

A number of theories have been proposed to estimate the frequency-dependent moduli. One class of theories describes the pore structure based on a continuous distribution of pore shapes (O'Connell & Budiansky, 1977; Palmer & Traviolia, 1980). An alternative approach characterizes the pore geometry by two or three distinct aspect ratios (de Paula et al., 2012; Gurevich et al., 2010; Pride et al., 2004). However, all these theories have a number of “free” parameters characterizing the pore shapes (such as pore aspect ratio and the amount of compliant porosity). These parameters are never known and are usually obtained by fitting to the experimental data. This reduces the predictive power and usefulness of these models as a good fit is not necessarily a proof that the model is adequate.

The goal of this paper is to overcome this uncertainty and obtain such parameters independently from the pressure dependency of the velocities or elastic moduli. Indeed, the pressure dependency of the velocities or elastic moduli is controlled by the shape and fraction of compliant pores or cracks. Hence, the analysis

of this dependency can be used to estimate these parameters. One such approach was developed by de Paula et al. (2012) and Sun et al. (2018), who adopted the theoretical model of pressure dependency of dry velocities previously proposed by Shapiro (2003). However, the Shapiro (2003) model does not explicitly include the pore shape parameters; hence, de Paula et al. (2012) and Sun et al. (2018) assumed that compliant pores in the Shapiro (2003) model all have the same aspect ratio. However, this assumption is rather arbitrary and restrictive. Indeed, it is well known that rocks cannot be adequately described by cracks with a single aspect ratio.

A more rigorous and direct approach is to obtain the distribution of aspect ratios directly from the stress dependency of dry velocities. The quantitative relationship between the stress dependency of the elastic moduli and pore shape distribution was first proposed by Morlier (1971), refined by Zimmerman (1991) and more recently by David and Zimmerman (2012). Later, David and Zimmerman (2013) developed a model for frequency-dependent moduli based on the work of David and Zimmerman (2012). However, unlike the theories of Murphy (1982), Pride et al. (2004), Gurevich et al. (2010), or Glubokovskikh et al. (2016), the approach of David and Zimmerman (2013) does not explicitly solve the micromechanical problem of wave-induced fluid flow between pores of different shapes. Instead, it assumes that pores are either in full communication or isolated and uses the cross frequency as a fitting parameter.

In this paper, we develop a mechanically consistent model that combines the stress-dependent model of dry velocities of David and Zimmerman (2012) with the micromechanical squirt-flow model of Gurevich et al. (2010) and Glubokovskikh et al. (2016) to account for the pressure and frequency effects on the elastic moduli of fluid-saturated rocks. First, we briefly review the theoretical model of David and Zimmerman (2012) for the pressure dependency of the dry moduli as a function of the distribution of aspect ratios. Then, we also briefly describe a micromechanical model for pressure relaxation between compliant pores (with a single aspect ratio) and stiff pores. We then develop an approach that incorporates this pressure relaxation between compliant and stiff pores into the model of pressure dependency of the moduli. The resulting model gives elastic moduli and attenuation factors as functions of both pressure and frequency. We then illustrate the model using published laboratory measurements performed with ultrasonic and forced oscillation techniques and obtain a reasonable agreement between the model predictions and the measurements.

2. Background Theory

2.1. Pressure Dependency of Moduli

Numerous laboratory studies show that the elastic velocities or moduli of dry rock increase substantially with increasing effective pressure (confining pressure minus pore pressure) (Eberhart-Phillips et al., 1989; Han et al., 1986; Zimmerman, 1991). This pressure dependency is often explained by the progressive closure of cracks depending on their aspect ratios (Walsh, 1965; Zimmerman, 1991). Although these cracks make up a small proportion of the pore space, they have significant effects on the effective velocities of porous rocks as they have much higher compliances (and hence they close at much lower pressures than stiff pores) than say spherical or near-spherical pores. David and Zimmerman (2012) considered an isotropic rock with matrix moduli K_s and G_s and total porosity ϕ and assumed that the pore space is characterized by compliant pores ϕ_c with a distribution of small aspect ratios (usually in a range between 10^{-4} and 10^{-2}) and a group of non-closable stiff pores with the specific volume ϕ_s , which are assumed to have a single aspect ratio between 0.1 and 1, that is, much larger than any of the compliant pores. With effective pressure increasing, compliant pores are gradually closing. When effective pressure approaches a much higher value, compliant pores are closed completely and the moduli K_{dry}^{hp} and G_{dry}^{hp} (superscript *hp* refers to the high-pressure limit) only correspond to the effects of nonclosable stiff pores. In this limit, the dry velocities or moduli typically increase linearly or remain constant with increasing effective pressure. Thus, any deviation from this linear variation is caused by the closure of cracks with increasing effective pressure. Therefore, the pressure dependency of dry moduli $K_{dry}(p)$ and $G_{dry}(p)$ allows the extraction of crack aspect ratio distribution at each pressure. Those dry moduli can be obtained directly from ultrasonic measurements on dry samples assuming that the frequency dispersion of the dry moduli is negligible (Mikhailovskikh et al., 2019; Pimienta et al., 2017).

2.1.1. Pressure Dependency of the Dry Moduli

As explained earlier, the pressure dependency of the velocities or moduli is governed by compliant pores, which are often approximated by penny-shaped cracks with small aspect ratios. According to David and Zimmerman (2012), in a noninteractive approximation, the dry bulk and shear moduli K_{dry} and G_{dry} are given by their eq. 40 and 41 with $K_f \rightarrow 0$

$$\frac{K_{\text{dry}}^{\text{hp}}}{K_{\text{dry}}(p)} = 1 + \int_{\alpha^0 > \alpha^*(p)} \left[c(\alpha^0) \left(1 - \frac{\alpha^*(p)}{\alpha^0} \right) \times P_{\text{dry}}(\alpha^0 - \alpha^*(p), \nu_{\text{dry}}^{\text{hp}}) \right] d\alpha^0, \quad (1)$$

$$\frac{G_{\text{dry}}^{\text{hp}}}{G_{\text{dry}}(p)} = 1 + \int_{\alpha^0 > \alpha^*(p)} \left[c(\alpha^0) \left(1 - \frac{\alpha^*(p)}{\alpha^0} \right) \times Q_{\text{dry}}(\alpha^0 - \alpha^*(p), \nu_{\text{dry}}^{\text{hp}}) \right] d\alpha^0, \quad (2)$$

where P_{dry} and Q_{dry} define the bulk and shear excess compliances of dry pores. For ellipsoidal pores, analytical expressions for P_{dry} and Q_{dry} can be found in Berryman (1980) and David and Zimmerman (2011). Also, in Equations 1 and 2,

$$\nu_{\text{dry}}^{\text{hp}} = (3K_{\text{dry}}^{\text{hp}} - 2G_{\text{dry}}^{\text{hp}}) / (6K_{\text{dry}}^{\text{hp}} + 2G_{\text{dry}}^{\text{hp}}),$$

where $\nu_{\text{dry}}^{\text{hp}}$ is the Poisson's ratio of the dry porous matrix without compliant pores (cracks). α^0 is the crack aspect ratio distribution at zero pressure, which is given in Appendix B. $c(\alpha^0)$ is the crack porosity distribution function. $\alpha^*(p)$ is the critical aspect ratio such that all cracks having aspect ratios smaller than $\alpha^*(p)$ will close completely at pressure p

$$\alpha^*(p) = \frac{4 \left[1 - (\nu_{\text{dry}}^{\text{hp}})^2 \right]}{3\pi K_{\text{dry}}^{\text{hp}} (1 - 2\nu_{\text{dry}}^{\text{hp}})} p. \quad (3)$$

Note that $\alpha^*(p)$ is also equal to the decrease of aspect ratio caused by pressure p . All cracks having aspect ratios higher than $\alpha^*(p)$ will have the same amount of decrease in aspect ratios, which gives the effective crack aspect ratio distribution at each pressure p as $\alpha(p) = \alpha^0 - \alpha^*(p)$.

The advantage of using a noninteractive approximation is that Equations 1 and 2 are uncoupled and only contain the unknown effective moduli $K_{\text{dry}}(p)$ and $G_{\text{dry}}(p)$ on the left-hand side. Thus, the integrals in these equations can be evaluated analytically.

2.1.2. Pressure Dependency of the Moduli of Saturated Rock in the Low- and High-Frequency Limits

In order to model the pressure effects on the frequency-dependent moduli of fluid-saturated rocks in a full frequency range, we first compute the fluid-saturated moduli in the low- and high-frequency limits. In the low-frequency limit, the saturated moduli $K_{\text{sat}}^{\text{lf}}$ and $G_{\text{sat}}^{\text{lf}}$ are obtained by the Gassmann (1951) equation

$$K_{\text{sat}}^{\text{lf}} = K_{\text{dry}} + \frac{(K_s - K_{\text{dry}})^2}{(K_s - K_f)\phi + (K_s - K_{\text{dry}})}, \quad (4)$$

$$G_{\text{sat}}^{\text{lf}} = G_{\text{dry}}, \quad (5)$$

where K_f is the bulk modulus of the fluid.

In the high-frequency limit, it is convenient to obtain the moduli of the saturated rock $K_{\text{sat}}^{\text{hf}}$ and $G_{\text{sat}}^{\text{hf}}$ through a two-stage process. First, define the moduli of the modified frame (a rock in which cracks are filled with the liquid but the stiff pores are dry), and then calculate the effect of fluid in stiff pores using Gassmann equations (Mavko & Jizba, 1991). The modified frame moduli $K_{\text{mf}(p)}$ and $G_{\text{mf}(p)}$ can be obtained by replacing the dry cracks in Equations 1 and 2 with fluid-saturated cracks,

$$\frac{K_{\text{dry}}^{\text{hp}}}{K_{\text{mf}}(p)} = 1 + \int_{\alpha^0 > \alpha^*(p)} \left[c(\alpha^0) \left(1 - \frac{\alpha^*(p)}{\alpha^0} \right) \left(1 - \frac{K_f}{K_{\text{dry}}^{\text{hp}}} \right) \times P_{\text{sat}} \left(\alpha^0 - \alpha^*(p), \frac{K_f}{K_{\text{dry}}^{\text{hp}}}, \nu_{\text{dry}}^{\text{hp}} \right) \right] d\alpha^0, \quad (6)$$

$$\frac{G_{\text{dry}}^{\text{hp}}}{G_{\text{mf}}(p)} = 1 + \int_{\alpha^0 > \alpha^*(p)} \left[c(\alpha^0) \left(1 - \frac{\alpha^*(p)}{\alpha^0} \right) \times Q_{\text{sat}} \left(\alpha^0 - \alpha^*(p), \frac{K_f}{K_{\text{dry}}^{\text{hp}}}, \nu_{\text{dry}}^{\text{hp}} \right) \right] d\alpha^0, \quad (7)$$

where P_{sat} and Q_{sat} are bulk and shear excess compliances of wet cracks. Then, the bulk modulus of the fully saturated rock is obtained by substituting $K_{\text{mf}}(p)$ given by Equation 6 for $K_{\text{dry}}(p)$ in Gassmann's equation, Equation 4.

The high-frequency moduli obtained by this approach is similar to but somewhat different from eqs. (40) and (41) of David and Zimmerman (2012) for fluid-saturated rocks, because in their equations, the effect of fluid in stiff pores is expressed through the effective medium theory, rather than Gassmann's equations. However, since the pressure in stiff pores should be approximately uniform, these two methods should give similar results (Sun et al., 2020).

Mavko and Jizba (1991) showed that at for liquid-saturated rocks, the modified frame moduli at ultrasonic frequencies are related to dry moduli by equations

$$\frac{1}{K_{\text{mf}}(p)} = \frac{1}{K_{\text{dry}}^{\text{hp}}} + \left(\frac{1}{K_f} - \frac{1}{K_s} \right) \phi_c, \quad (8)$$

and

$$\frac{1}{G_{\text{mf}}(p)} = \frac{1}{G_{\text{dry}}(p)} - \frac{4}{15} \left(\frac{1}{K_{\text{dry}}(p)} - \frac{1}{K_{\text{mf}}(p)} \right), \quad (9)$$

It is shown in Appendix A that Equations 6 and 7 are approximately consistent with Equations 8 and 9.

2.2. Dispersion

MJ model is only valid for liquid-saturated rocks. For rocks saturated with softer fluids (e.g., gas), Gurevich et al. (2009b) (referred to MJG) generalized these equations to give

$$\frac{1}{K_{\text{mf}}(p)} = \frac{1}{K_{\text{dry}}^{\text{hp}}} + \frac{1}{\frac{1}{\frac{1}{K_{\text{dry}}(p)} - \frac{1}{K_{\text{dry}}^{\text{hp}}} + \left(\frac{1}{K_f} - \frac{1}{K_s} \right) \phi_c}}, \quad (10)$$

$$\frac{1}{G_{\text{mf}}(p)} = \frac{1}{G_{\text{dry}}(p)} - \frac{4}{15} \left(\frac{1}{K_{\text{dry}}(p)} - \frac{1}{K_{\text{mf}}(p)} \right). \quad (11)$$

For finite (intermediate) frequencies (partially relaxed pores), Gurevich et al. (2010) showed that the moduli obey the same Equations 10 and 11 but with fluid modulus K_f replaced by a frequency-dependent quantity $K_f^*(\omega)$ given by the solution of the elastic problem for a flat contact between grains filled with a viscous fluid. Glubokovskikh et al. (2016) simplified and generalized the approach of Gurevich et al. (2010) to account for solid and viscoelastic pore fill. For a particular case of a fluid pore fill with dynamic viscosity η , the corresponding expression for $K_f^*(\omega)$ is given by Tsai and Lee (1998)

$$K_f^*(\omega) = K_f + \frac{4}{3} G_f^*(\omega) - \frac{(K_f - \frac{2}{3} G_f^*(\omega))^2}{\left(K_f + \frac{4}{3} G_f^*(\omega) \right) \frac{\gamma_f}{2\alpha} \frac{I_0 \left(\frac{\gamma_f}{2\alpha} \right)}{2I_1 \left(\frac{\gamma_f}{2\alpha} \right)} - G_f^*(\omega)}, \quad (12)$$

Table 1
Properties of the Two Samples and Pore Fluid in This Study (David & Zimmerman, 2012; Fortin et al., 2007)

Sandstone	Porosity (%)	Bulk density (dry) (kg/m ³)	Matrix K_s (GPa)	Matrix G_s (GPa)	Water K_f (GPa)	Water η (Pa·s)
Fontainebleau	4	1,950	37	44	2.24	10^{-3}
Vosges	25	2,544	39	24	2.20	10^{-3}

where

$$\gamma_f = \sqrt{\frac{36G_f^*(\omega)}{3K_f + 4G_f^*(\omega)}}$$

where $\alpha \ll 1$ is the aspect ratio of the grain-to-grain contact (or crack), I_k is a modified Bessel function of the first kind of the order k , and $G_f^*(\omega) = i\omega\eta$.

3. Modeling the Pressure-Dependent Moduli at Intermediate Frequencies

In the high-frequency limit, the pressure dependency of the bulk and shear moduli of the modified frame is defined by Equations 6 and 7. The moduli at lower frequencies can be obtained by replacing the fluid bulk modulus K_f in Equations 6 and 7 with $K_f^*(\omega)$

$$\frac{K_{\text{dry}}^{\text{hp}}}{K_{\text{mf}}(p, f)} = 1 + \int_{\alpha^0 > \alpha^*(p)} \left[c(\alpha^0) \left(1 - \frac{\alpha^*(p)}{\alpha^0} \right) \left(1 - \frac{K_f^*(\omega)}{K_{\text{dry}}^{\text{hp}}} \right) \times P \left(\alpha^0 - \alpha^*(p), \frac{K_f^*(\omega)}{K_{\text{dry}}^{\text{hp}}}, \nu_{\text{dry}}^{\text{hp}} \right) \right] d\alpha^0, \quad (13)$$

$$\frac{G_{\text{dry}}^{\text{hp}}}{G_{\text{mf}}(p, f)} = 1 + \int_{\alpha^0 > \alpha^*(p)} \left[c(\alpha^0) \left(1 - \frac{\alpha^*(p)}{\alpha^0} \right) \times Q \left(\alpha^0 - \alpha^*(p), \frac{K_f^*(\omega)}{K_{\text{dry}}^{\text{hp}}}, \nu_{\text{dry}}^{\text{hp}} \right) \right] d\alpha^0. \quad (14)$$

Equations 13 and 14 essentially generalize the approach of Gurevich et al. (2010) to a broad range of aspect ratios (and their dependence on pressure). Once the modified frame moduli $K_{\text{mf}}(p, f)$ and $G_{\text{mf}}(p, f)$ are obtained from Equations 13 and 14, the fully saturated moduli K_{sat} and G_{sat} can be computed using Equations 4 and 5 with $K_{\text{dry}}(p)$ and $G_{\text{dry}}(p)$ replaced by the modified frame moduli $K_{\text{mf}}(p, f)$ and $G_{\text{mf}}(p, f)$.

In the dry case, Equations 13 and 14 are uncoupled and only contain the unknown effective moduli $K_{\text{mf}}(p, f)$ and $G_{\text{mf}}(p, f)$ on the left-hand side. In contrast to Equations 1 and 2, in Equations 13 and 14, factors P and Q depend on the aspect ratio in a complicated way, and thus, the integrals cannot be evaluated analytically but can be easily computed numerically.

Equations 13 and 14 with Equation 12 are the central results of this paper. They give the dependency of the moduli on both pressure and frequency. This is illustrated in the next section by comparing the model predictions against laboratory measurements.

4. Comparisons to Published Laboratory Data

4.1. Comparisons to Ultrasonic Measurements

4.1.1. Crack Aspect Ratio Distribution

To illustrate our model, we apply the scheme to the published laboratory measurements of ultrasonic P - and S -wave velocities and density on two isotropic sandstone samples. One data set consists of the ultrasonic measurements of David and Zimmerman (2012) on a Fontainebleau sandstone sample at a frequency of 1 MHz, in the effective pressure range of 0–90 MPa (here pore pressure is set to 5 MPa, and confining pressure is increased gradually). Fontainebleau sandstone is a well-sorted system of pure quartz ideal for rock physics analysis as it has almost the same grain size of 250 μm . Another set is the ultrasonic measurements of Fortin et al. (2007) on a Vosges sandstone sample at a frequency of 1 MHz, in an effective pressure range from 0 to 110 MPa. This sample has a mineral composition of ~50% quartz, ~20% oxides micas, and ~30% feldspar. Grain sizes are from 80 to 150 μm with an average value of 110 μm . Since the anisotropy is lower than 1.5%, we can treat this sample as isotropic. Physical properties of these two samples are presented in

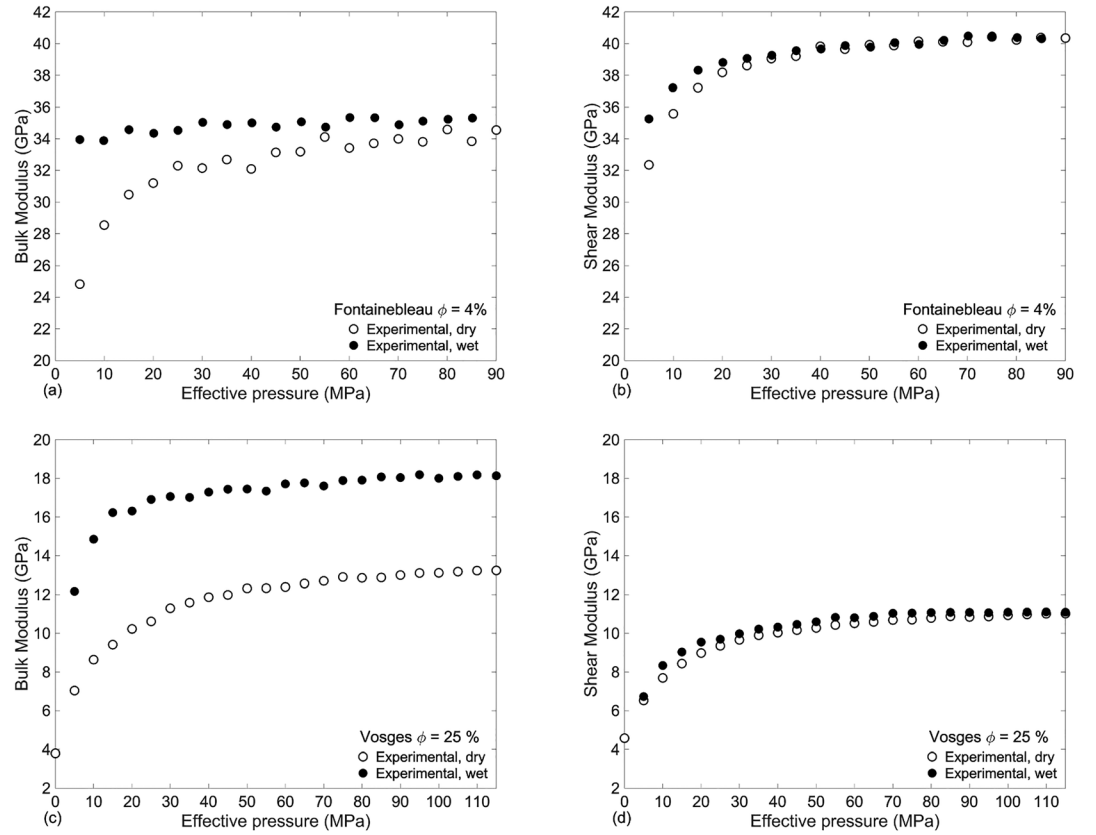


Figure 1. Ultrasonic measurements of the dry (open circles) and water-saturated (solid circles) bulk and shear moduli of the (a and b) Fontainebleau and (c and d) Vosges sandstone samples.

Table 1. The pore fluid was water with the bulk modulus $K_f = 2.24$ GPa measured at 10 MPa for the Fontainebleau sandstone, and $K_f = 2.20$ GPa for Vosges sandstone sample measured at 5 MPa (David & Zimmerman, 2012). The viscosity of water η is taken to be 10^{-3} Pa·s.

The workflow described in the previous section requires the high-pressure limit dry moduli K_{dry}^{hp} and G_{dry}^{hp} . For Fontainebleau sandstone sample, we take these values directly from the measurements at the highest pressure from David and Zimmerman (2012). The reason is that both dry (open circles) and water-saturated (solid circles) bulk and shear moduli shown in Figures 1a and 1b level off (within measurement errors) at pressures over 70 MPa, which implies that cracks are closed completely at such pressures. Conversely, both dry and water-saturated moduli of Vosges sandstone sample (Figures 1c and 1d) show a steady linear increase at high pressures over 50 MPa, which is due to the closure of stiffer pores (Gurevich et al., 2009a). Such linear trends are commonly observed in many rocks (de Paula et al., 2012; Shapiro, 2003; Sun et al., 2018; Vernik & Hamman, 2009). Thus, for the Vosges sandstone sample, in a slight deviation from the approach of David and Zimmerman (2012), we assume that moduli K_{dry}^{hp} and G_{dry}^{hp} of the host medium are linear functions of pressure.

Then, we obtain the crack density $\Gamma(p)$ by least-square fitting of the values of the pressure dependency of ultrasonic velocities and density (Figure 2). Open (solid) circles show the inverted crack density obtained from the dry bulk (shear) modulus only at each pressure. Solid line gives the fitting result from both the bulk and shear moduli simultaneously using an exponential dependence of the crack density $\Gamma(p)$ on pressure:

$$\Gamma(p) = \Gamma^0 e^{-\frac{p}{\hat{p}}}, \quad (15)$$

where Γ^0 is the crack density at $p = 0$ and \hat{p} is a scaling factor. The good fit shows that the assumption of crack density that obeys an exponential decay law is adequate and meaningful, at least for these two sandstone samples.

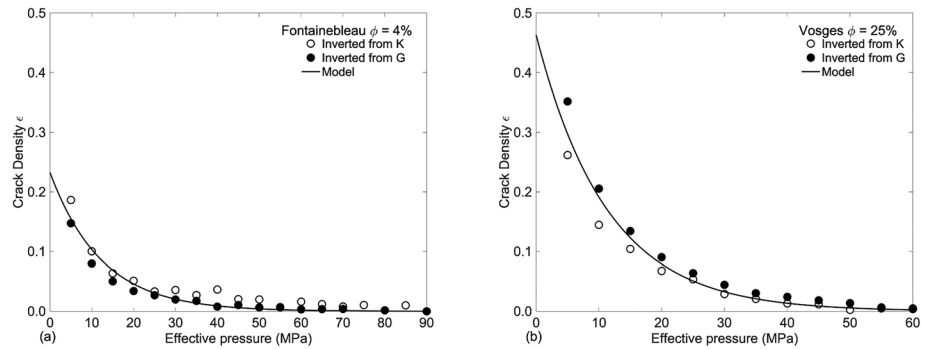


Figure 2. Crack density modeling for the (a) Fontainebleau and (b) Vosges sandstone samples as a function of effective pressure. Open (solid) circles show the inverted crack density obtained from the dry bulk (shear) modulus only at each pressure. Solid line gives the fitting result from both bulk and shear moduli simultaneously.

Figure 3 presents the modeling results of the effective dry bulk and shear moduli (solid lines) for Fontainebleau (a and b) and Vosges (c and d) sandstone sample versus effective pressure against ultrasonic measurements (open circles). For the Fontainebleau sandstone sample, similarly to David and Zimmerman (2012), the stress-dependent model fits the dry bulk and shear moduli reasonably well. For the Vosges sandstone sample, we observe that the combination of an exponential term and a linear term (dash line) describes the pressure dependency more accurately.

Figure 4 shows the crack density $\Gamma(\alpha^0)$ as a function of crack aspect ratio distribution α^0 at zero pressure. Open (solid) circles show the inverted crack density obtained from the dry bulk (shear) modulus only at each pressure, while the solid line shows the modeling results using Equation B5 in Appendix B, which proves that an exponential pressure dependency of compressibility implies an exponential distribution of crack aspect ratios (David & Zimmerman, 2012; Morlier, 1971; Zimmerman, 1991).

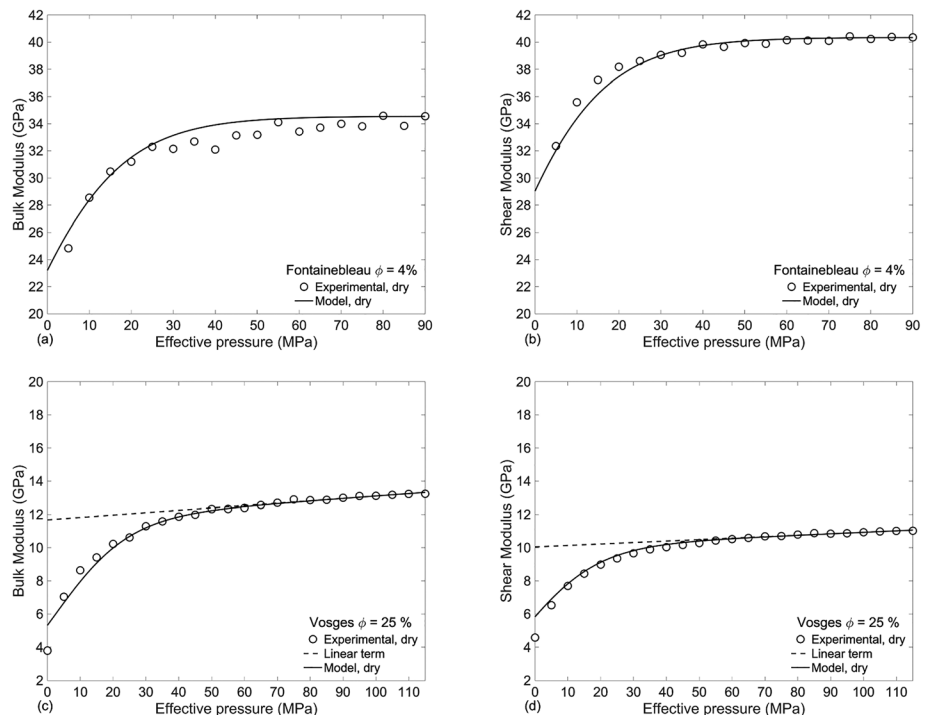


Figure 3. Fitting of the effective dry bulk and shear moduli (solid lines) of the (a and b) Fontainebleau and (c and d) Vosges sandstone samples versus effective pressure against ultrasonic measurements (open circles).

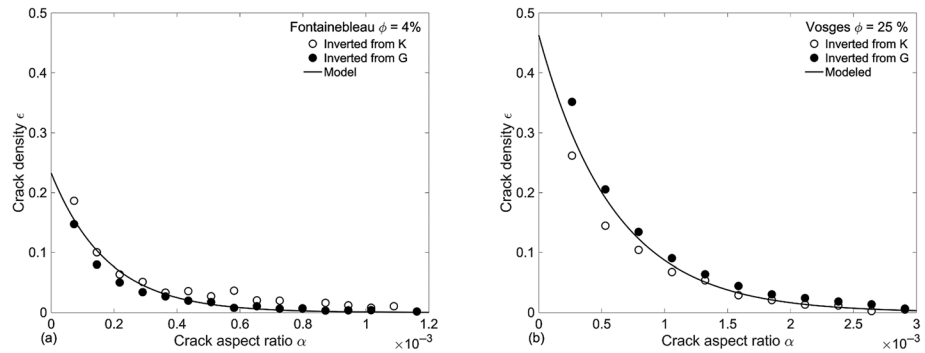


Figure 4. Inverted crack density for the (a) Fontainebleau and (b) Vosges sandstone samples as a function of the aspect ratio distribution at zero pressure. Open (solid) circles show the inverted crack density obtained from the dry bulk (shear) modulus only at each pressure. Solid lines give the fitting result from both the bulk and shear moduli simultaneously.

Once the crack aspect ratio distribution α^0 zero pressure and the critical aspect ratio $\alpha^*(p)$ are obtained, we can obtain the crack porosity distribution function as

$$c(a) = -\frac{4}{3}\pi\alpha\frac{d\Gamma}{d\alpha}, \quad (16)$$

and cumulative porosity distribution function as

$$C(a) = -\int_{\alpha^0 > \alpha^*(p)} c(a) \left(1 - \frac{\alpha^*(p)}{\alpha^0}\right) d\alpha^0, \quad (17)$$

(David & Zimmerman, 2012).

Figure 5 illustrates the pressure effects on the crack porosity distribution function $c(a)$ (a and b) and cumulative crack porosity function $C(a)$ (c and d) as a function of the effective crack aspect ratio distribution for Fontainebleau (a) and Vosges (b) sandstone samples respectively, which are very similar to the result of David and Zimmerman (2013). As expected, crack porosity is sensitive to the effective pressure. The increase of effective pressure from 0 to 10 MPa leads to a decrease in crack porosity of over 50% for both Fontainebleau and Vosges samples (Figures 5a and 5b). This decrease can also be illustrated by the pressure dependency of cumulative porosity distribution in Figures 5c and 5d. The crack porosity decreases from 0.017% to 0.0076% for the Fontainebleau sample and from 0.11% to 0.045% for Vosges samples with the increase of effective pressure from 0 to 10 MPa.

4.1.2. Pressure and Frequency Effects on the Moduli of the Fluid-Saturated Rocks

Parameters obtained above allow us to compute the pressure and frequency dependence of the saturated moduli using Equations 13 and 14. Figure 6 shows the model predictions for water-saturated bulk and shear moduli (real part) for the Fontainebleau (a and b) and Vosges (c and d) sandstone samples versus the wave frequency at increasing effective pressure, 0 MPa (solid line), 10 MPa (dashed line), 20 MPa (dash-dotted line), and 50 MPa (dotted line), respectively. Predicted bulk and shear moduli show significant dispersion between the seismic (\sim Hz) and ultrasonic (\sim MHz) frequencies at pressures below 50 MPa where most cracks are still open. At zero pressure, model predictions for Fontainebleau sandstone show increases of 21.8% and 11.4% for bulk and shear moduli respectively between low- and high-frequency limits. For Vosges sandstone, the differences between low- and high-frequency bulk and shear moduli are 37.8% and 17.3%, respectively. However, at high pressures (around 50 MPa), no dispersion of either bulk or shear moduli is observed. This behavior is consistent with our expectation that pressure gradients between compliances of different shapes control the fluid and frequency effects on the moduli of fluid-saturated rocks. With increasing effective pressure, the frequency dependence of bulk and shear moduli is decreased as cracks are gradually closed. Note that at high frequency (it depends on the crack aspect ratio distribution, here around 1 MHz), the bulk modulus is almost independent of effective pressure as all the compliant pores are closed. Therefore, the value of the bulk modulus is approaching that of the host medium. For the shear modulus, the behavior is different as water at 1 MHz still has negligible shear resistance. Indeed, the characteristic frequency of viscous shear

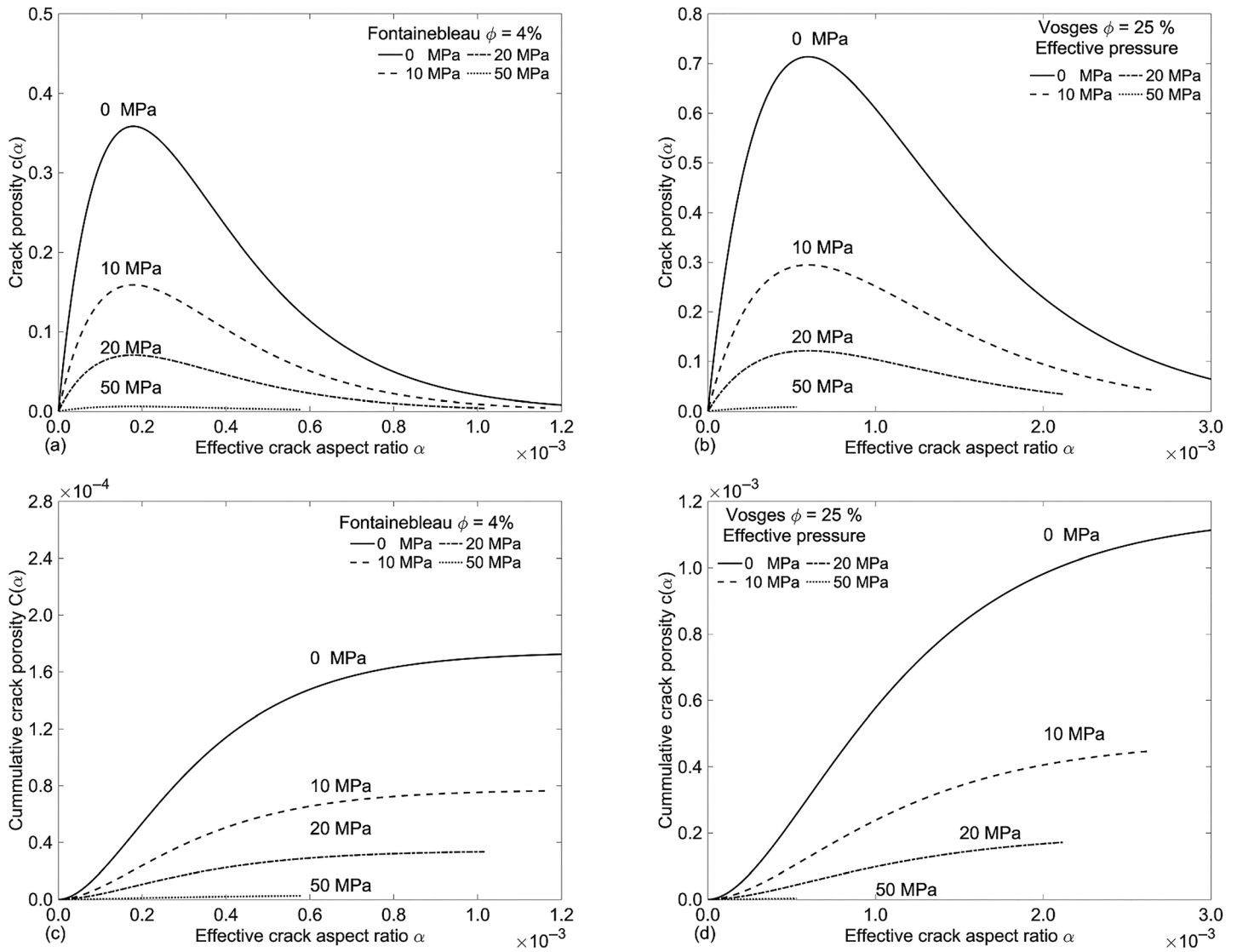


Figure 5. (a and b) Differential $c(\alpha)$ and (c and d) cumulative $C(\alpha)$ crack porosity distribution versus the effective crack aspect ratio at different effective pressures for the Fontainebleau and Vosges sandstone samples.

relaxation is $f_v = \alpha G_s / 2\pi\eta$, where α is the crack aspect ratio and G_s the mineral shear modulus (O'Connell & Budiansky, 1977). For water-saturated cracks with $\alpha = 10^{-3}$ in quartz, f_v is about $0.6 \cdot 10^{10}$ Hz. Increasing effective pressure leads to the gradual closure of cracks, which increases shear modulus.

Figure 7 shows the model predictions for water-saturated bulk and shear moduli for the Fontainebleau (a and b) and Vosges (c and d) sandstone samples versus the effective pressure at increasing frequencies f of 1 Hz, 1 KHz, and 1 MHz. For the Fontainebleau sandstone sample, model predictions at ultrasonic frequency (red line) for water-saturated bulk (a) and shear (b) moduli show a reasonable match with ultrasonic measurements (solid circles). The bulk modulus at such frequencies appears to be independent of effective pressure, which indicates that the rock is in the fully unrelaxed state. Besides, model predictions (blue line) at 1 Hz for water-saturated bulk and shear moduli are almost identical to the estimates for bulk (stars) and shear (open circles) moduli from the Gassmann theory, which show that our model is Gassmann consistent in the low-frequency limit.

For the Vosges sandstone sample, model predictions (red line) give a reasonable fit for the shear modulus of water-saturated sandstone measured at 1 MHz (solid circles). However, there is a clear discrepancy for bulk

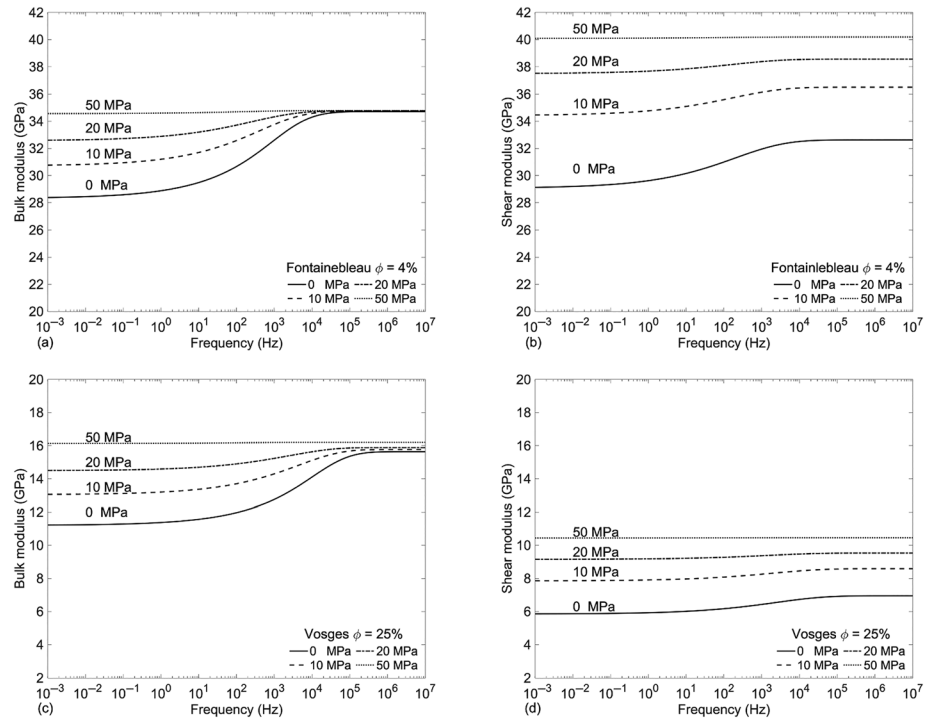


Figure 6. Model predictions for water-saturated bulk and shear moduli for the (a and b) Fontainebleau and (c and d) Vosges sandstone samples as a function of frequency at different effective pressures.

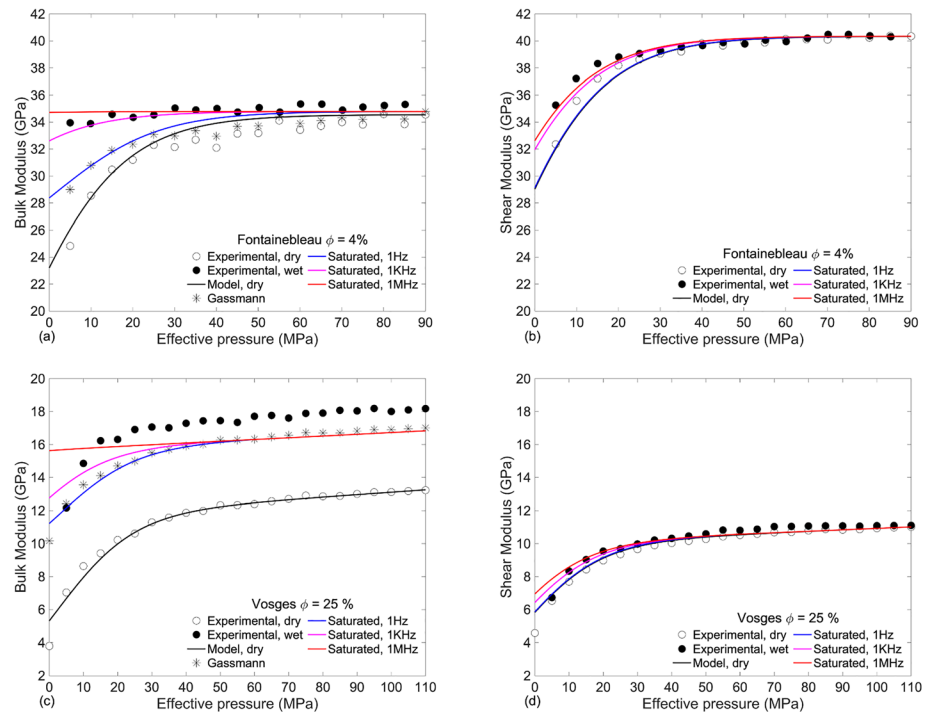


Figure 7. Model predictions for water-saturated bulk and shear moduli for the (a and b) Fontainebleau and (c and d) Vosges sandstone samples as a function of effective pressure at different frequencies.

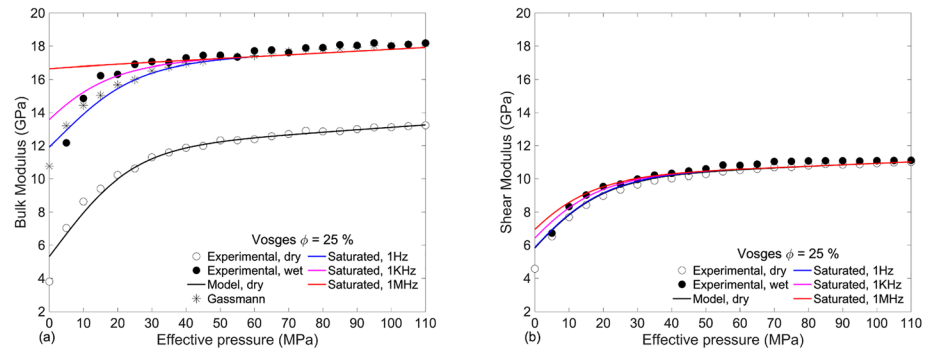


Figure 8. Model predictions for (a) water-saturated bulk and (b) shear moduli for the Vosges sandstone samples as a function of effective pressures at different frequencies. The plots are an update of Figures 7c and 7d by adjusting the bulk modulus of the matrix to $K_s = 53$ GPa.

modulus at all pressures. The reason for this systematic discrepancy may be in the mineral composition of Vosges sandstone, which is much more complex than Fontainebleau sandstone. The moduli of some of its minerals are not well defined, and hence, the overall mineral modulus needed for the Gassmann equation has some uncertainty. Moreover, strictly speaking, the Gassmann theory is not valid for multiminerall rocks (Mavko & Mukerji, 2013); instead, a more general model of Brown and Korrington (1975) should be used, but parameters of this model are hard to define independently.

Hence, we treat the mineral bulk modulus for the Vosges sandstone as an adjustable parameter. The value $K_s = 53$ GPa gives the best fit between the predicted and measured moduli at high pressures. The updated modeling for the Vosges sandstone sample is shown in Figure 8. At higher pressures, the Gassmann prediction (stars) is now consistent with laboratory measurements (solid circles) at ultrasonic frequencies. Yet, at low pressures, there exists some discrepancy between the modeling results and ultrasonic measurements.

One possible reason is the uncertainty of the “dry” rock velocities or moduli obtained from laboratory measurements. One uncertainty in the practice of ultrasonic measurements is that even a small amount of water adsorbed in the cracks results in a significant weakening of the dry velocities or moduli. This effect has been reported by numerous studies (Murphy, 1982; Pimienta et al., 2017; Wyllie et al., 1962; Yurikov et al., 2018). The ultrasonic measurements of dry velocities are conducted at room relative humidity (RH). Such measurements will cause the uncertainty of the dry velocities or moduli obtained, which might account for the mismatch between the model predictions and ultrasonic measurements of the Vosges sandstone sample. Note that this effect is most pronounced at the lowest effective pressures, where the adsorption stress is comparable to the applied pressure.

Another possible reason for the discrepancy can be related to the use of the modified frame concept. In particular, recent numerical simulations (Alkhimenkov et al., 2020) show that the frequency dependency of the elastic moduli can be strongly affected by the interaction between the crack and the pores connected to it. This effect is ignored in our work but will be explored in future studies.

Additionally, the pore structure characterization in this paper is based on the assumption of ellipsoidal pore shapes, which are amenable to analytical solutions in closed form based on the Eshelby theory (O’Connell & Budiansky, 1974; Walsh, 1965). This treatment might be oversimplified as almost no realistic cracks have ellipsoidal shapes (Mavko & Nur, 1978). Thus, the crack aspect ratio distribution obtained from the stress dependency of dry velocities or moduli is nonunique and depends on the crack model chosen. Indeed, an alternative model can be developed based on the concept of rough cracks, where stress dependency corresponds to asperities coming into contact or complex-shaped cracks (Mavko & Nur, 1978). However, we currently do not have a micromechanical squirt-flow model for these geometries. This is an interesting subject for future research but is outside the scope of the present paper.

4.2. Comparisons With Forced Oscillation Measurements

We also apply the proposed model to the published forced oscillation data on two glycerin-saturated carbonate samples measured by Borgomano et al. (2019). Forced oscillation method is ideal for measuring dispersion and

Table 2

Properties of the Two Limestone Samples and Pore Fluid in This Study (Borgomano et al., 2019)

Sandstone	Porosity (%)	Matrix K_s (GPa)	Crack-free matrix ν_{dry}^{hp}	Crack-free matrix K_{dry}^{hp} (GPa)	Glycerine K_f (GPa)	Glycerine η (Pa·s)
Coquina	7.5	77	0.2	54	4.36	1
Indiana	13.9	77	0.2	35.5	4.36	1

attenuation in rocks (Batzle et al., 2006; Mikhaltsevitch et al., 2014; Paffenholz & Burkhardt, 1989; Pimienta et al., 2017; Spencer, 1981). The use of glycerin which is much more viscous than water is essential to lower the characteristic frequency of squirt flow, so it falls within the frequency range of quasi-static forced oscillation measurements (below 100 Hz). Borgomano et al. (2019) measured dispersion for four carbonate samples using forced oscillation measurements and showed that two of the samples exhibit squirt-flow dispersion. One of them is Coquina limestone consisting of >97% calcite. The measurements were performed at effective pressures from 3.5 to 25 MPa for dry rock and up to 10 MPa and in a full-frequency range from 0.2 to 100 Hz for glycerin-saturated condition (pore pressure is set to 2 MPa, and confining pressure is increasing). Another set is a thermally cracked Indiana limestone composed of pure calcite (69% fossiliferous calcite and 31% cement calcite). The hydrostatic oscillation was performed at pressures from 3.5 to 20 MPa for dry rock and up to 20 MPa and in a full-frequency range of 0.01–1 Hz for glycerin-saturated condition. Physical properties of these two samples are given in Table 2.

Figure 9 shows the fitting (solid line) for the dry bulk modulus of the Coquina (a) and Indiana (b) limestone samples against the forced oscillation measurements (open circles). Since the neither drained nor undrained moduli level off at the highest pressure available, the high-pressure limit modulus K_{dry}^{hp} cannot be obtained directly from the measurements; instead, we invert K_{dry}^{hp} from the measurements of the bulk modulus of the glycerin-saturated sample at the pressure of 20 MPa and the highest frequency using the Gassmann equation; see Table 2.

Figures 10a and 10b show the bulk modulus measured in a forced oscillation apparatus (symbols) and modeling results (lines) for the bulk modulus of the glycerin-saturated Coquina limestone sample and corresponding attenuation as a function of frequency. The measured bulk modulus at pressures 3.5 (solid circles) and 5 MPa (red diamonds) is significantly smaller than that for the undrained condition (horizontal line) as estimated from the Gassmann theory at pressure 3.5 MPa. This indicates that at these pressures, the

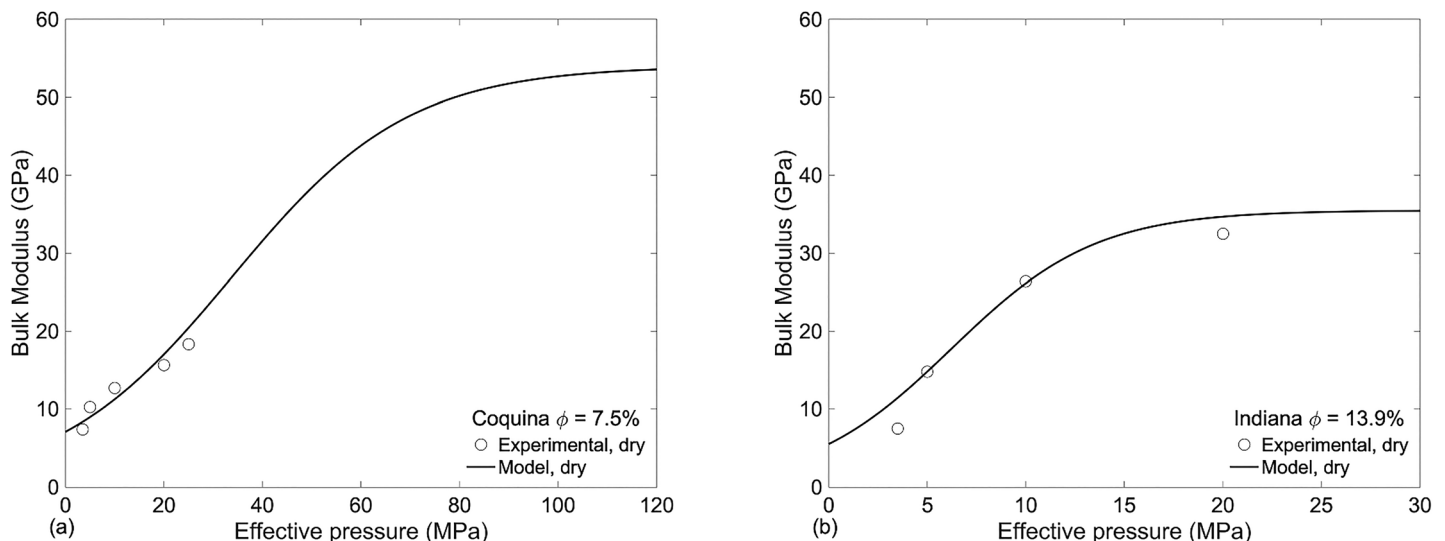


Figure 9. Best fit (solid lines) of the dry bulk modulus for the (a) Coquina and (b) Indiana limestone samples measured with the forced oscillation method (open circles).

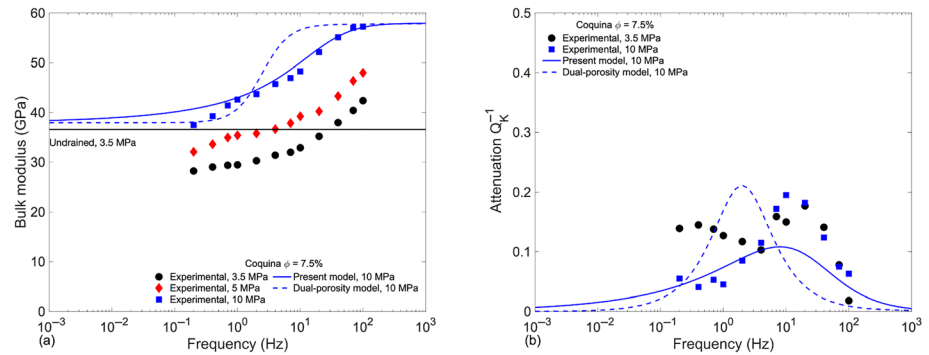


Figure 10. Comparison of the predictions (lines) for the frequency-dependent bulk modulus of the glycerin-saturated Coquina limestone sample and its corresponding attenuation as a function of frequency against the low-frequency measurements using the forced oscillation method (symbols).

rock has been significantly weakened by nonmechanical interaction with glycerin. Since these effects cannot be modeled with any squirt-flow model, we do not attempt to model the data at pressures of 3.5 and 5 MPa and only present the modeling for the highest pressure of 10 MPa (blue line). For the modulus (Figure 10a), the modeling gives an excellent match with the measurements (blue squares), in terms of dispersion magnitude, characteristic frequency, and shape. This match is much better than for the model with a single crack aspect ratio (Gurevich et al., 2010) (blue dashed line). For the attenuation (Figure 10b), the characteristic frequency is predicted reasonably well, but the magnitude of the attenuation peak is underestimated by about 45%.

For the cracked Indiana limestone, the undrained bulk modulus (taken as the measured modulus at the lowest frequency of 0.01 Hz) for the glycerin-saturated sample shows a dramatic variation with pressure (Figure 10b). Indeed, from pressure 3.5 (solid circles) to 20 MPa (magenta triangles), the increase in the bulk modulus is almost 22 GPa, which is much larger than for the dry modulus or the undrained modulus of the water-saturated sample (about 11 GPa) (see Fig. 8c of Borgomano et al., 2019). Similarly to the case of the Coquina, this suggests that the rock has been significantly altered by nonmechanical interaction with glycerin, and hence, the measurements for glycerin saturated samples cannot be modeled using pressure dependency of the dry moduli. Instead, we obtain the dry bulk modulus from the undrained modulus (measurements at the lowest frequency of 0.01 Hz) by inverting the Gassmann equation (Zhu & McMechan, 1990). Furthermore, we had to exclude the measurements at the pressure of 3.5 MPa due to the negative values obtained from the inversion. Indeed, the measured undrained modulus of 19 GPa at the pressure of 3.5 MPa is well below the lower Hashin-Shtrikman (or Wood) bound for a mixture of calcite and glycerin (23 GPa). The inverted dry bulk modulus for the pressures at 5, 10, and 20 MPa is shown in Figure 9b.

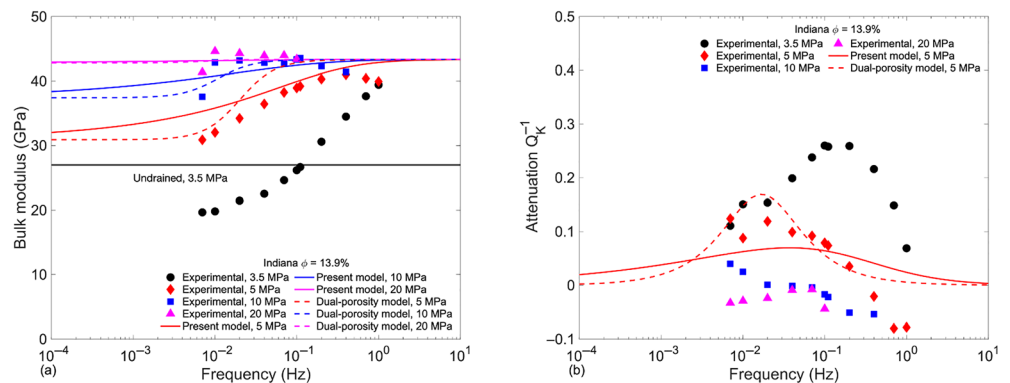


Figure 11. Comparison of the predictions (lines) for the frequency-dependent bulk modulus of the glycerin-saturated Indiana limestone sample and its corresponding attenuation as a function of frequency against the low-frequency measurements using the forced oscillation method (symbols).

Figures 11a and 11b show the frequency-dependent bulk modulus (Figure 11a) of the glycerin-saturated Indiana limestone sample and the corresponding attenuation (Figure 11b) as a function of frequency. At 5 MPa, the present model (red line) gives a reasonably good match with the measurements (red diamonds) and better than the dual-porosity model (red dashed line). At higher pressures of 10 and 20 MPa, all the models predict much smaller dispersion (see Figure 6a), which is broadly consistent with the measurements. For the attenuation (Figure 11b), similarly to the Coquina limestone sample, the present model (red line) gives a good estimate of the characteristic frequency but underestimates its magnitude. The measured attenuation for higher pressures is negative and cannot be predicted. These negative values may be used to quantify the measurement errors.

5. Discussion

We have presented a simple model to estimate the effects of fluid and pressure on the frequency-dependent moduli of fluid-saturated rocks. This model combines the stress dependency of dry moduli described by David and Zimmerman (2012) with the micromechanical squirt-flow pressure relaxation model of Gurevich et al. (2010) and Glubokovskikh et al. (2016). Application of this model to two sandstone samples shows a reasonable match with laboratory measurements. However, there are some discrepancies; in particular, the model does not explain the significant pressure dependency of the bulk modulus of fluid-saturated Vosges sandstone at the effective pressures below 15 MPa (Figure 8).

Comparison with the measurements of the Vosges sandstone sample at ultrasonic frequencies (Figures 7c and 8a) may seem inadequate because we argue that at such frequencies, they are in an unrelaxed regime. However, as shown in de Paula et al. (2012), this is not always true. Indeed, in the unrelaxed regime, the bulk modulus of most granular rocks is independent of pressure or increases linearly with increasing pressure (see, e.g., red lines in Figures 7a and 7c). Yet the measured ultrasonic water-saturated bulk (solid circles) modulus of the Vosges sandstone sample in Figure 7c shows significant pressure dependency. This shows that the moduli are not fully relaxed and cannot be modeled using any high-frequency theory. Indeed, they require a theory that models the rock moduli as a function of frequency as well as pressure. This cannot be done with either the model of David and Zimmerman (2012) (which only applies to the fully unrelaxed regime) or with the Gurevich et al. (2010) and Glubokovskikh et al. (2016) models, which cannot model pressure dependency. It might be modeled with the approaches of de Paula et al. (2012) and Sun et al. (2018), but the approach proposed in the present paper is much more rigorous and consistent.

The tests of our model against forced oscillation data should be regarded as strictly preliminary, as the very limited range of pressures for the dry or drained moduli is grossly insufficient to estimate the aspect ratio distribution with reasonable certainty. For this purpose, we explored a number of published data sets of forced oscillation measurements on several glycerin-saturated rocks (Borgomano et al., 2019; Chapman et al., 2019; Mikhaltsevitch et al., 2016; Pimienta et al., 2015) but encountered the same problem. We endeavor to pursue such measurements in the near future.

The proposed model uses noninteractive approximation, where the effects of all cracks are additive. For very large crack densities, this approach may be inadequate, and more complex schemes such as differential effective medium (Berryman, 1980; David & Zimmerman, 2012; Norris, 1985; Salganik, 1973) may be required. The proposed framework can incorporate any effective medium scheme, but the equations will become more complicated and would need to be solved by iteration.

Though the proposed model has been derived for fluid-saturated rocks, the pressure relaxation model of Glubokovskikh et al. (2016) is more general and can also incorporate solid and viscoelastic pore fill (Mikhaltsevitch et al., 2019; Sun et al., 2018; Sun et al., 2019). Thus, the present model can be easily extended to also incorporate these rheologies. This is important for a number of applications such as mineral substitution and prediction of viscoelastic properties of heavy oil rocks, where attenuation and dispersion may be even more significant (Ciz et al., 2009; Ciz & Shapiro, 2007; Saxena et al., 2016).

The model is limited to dispersion due to flow between cracks and pores, which is dominant for moderate to high-porosity rocks. For low-porosity cracked rocks, where crack-to-crack flow dominates, the proposed model is unlikely to be applicable.

The present model is also limited to isotropic rocks. Stress dependency of elastic properties of anisotropic rocks is an active topic of research, but the micromechanical model of squirt flow is general and can account for anisotropy (Collet & Gurevich, 2016).

6. Conclusion

We have developed a scheme to model the pressure and frequency effects on the elastic moduli of fluid-saturated rocks. This model combines the stress dependency of dry velocities of David and Zimmerman (2012) with the micromechanical model of squirt-flow relaxation (Glubokovskikh et al., 2016; Gurevich et al., 2010). In the proposed model, the pore space consists of two parts: compliant cracks that have a distribution of aspect ratios and stiff pores that have a single aspect ratio between 0.1 and 1. By quantitatively characterizing the crack closure process, we obtain the crack aspect ratio distribution at each pressure. Combined with the modified bulk modulus of fluid-saturated cracks derived from the squirt-flow dispersion models, modified frame moduli can be predicted by computing the effect of fluid-filled cracks in a dry porous matrix at each pressure. Then, fully fluid-saturated moduli at different frequencies can be obtained by using Gassmann equation for stiff pores. Applying this model to the Fontainebleau and Vosges sandstone samples gives reasonable fits to laboratory measurements at ultrasonic frequencies. More importantly, the model predictions for two carbonate samples give a reasonable match to the bulk modulus dispersion measured with the forced oscillation technique.

The significance of the proposed model lies in the fact that it eliminates the need for fitting parameters and thus increases its predictive power. Indeed, previous squirt-flow models (Chapman et al., 2002; Gurevich et al., 2010; Murphy et al., 1986; Pride et al., 2004) describe dispersion and attenuation for a given aspect ratio of penny-shaped cracks. This parameter is never known and has to be obtained from fitting to the data, thus reducing the predictive power of the models. Moreover, it is well known that rocks cannot be adequately described by cracks with a single aspect ratio and hence the previous models are too idealized and cannot describe the behavior of real rocks. Attempts to overcome this problem have been proposed by de Paula et al. (2012) and Sun et al. (2019) by using so-called triple porosity concept. However, the framework of David and Zimmerman (2012) provides a more rigorous and direct approach to obtaining aspect ratio distribution from the pressure dependency of dry moduli. Thus, incorporation of squirt-flow relaxation into the equation for the pressure dependency of elastic moduli provides an internally consistent squirt-flow model for velocity and attenuation as functions of both frequency and pressure.

Appendix A

Equations 6 and 7 give the modified frame moduli $K_{mf}(p)$ and $G_{umf}(p)$ of a hypothetical rock in which cracks with a distribution of aspect ratios are saturated with fluid while stiff pores remain dry. This appendix provides the equivalence of these equations with the MJ model.

A.1 Bulk Modulus

In Equation 6, factor $P_{\text{sat}} \left(\alpha^0 - \alpha^*(p), \frac{K_f}{K_{\text{dry}}^{\text{hp}}}, \nu_{\text{dry}}^{\text{hp}} \right)$ denotes the bulk excess compliance caused by the fluid-saturated crack. For a penny-shaped crack, it is expressed in an analytical form (Berryman, 1980)

$$P_{\text{sat}} = \frac{K_{\text{dry}}^{\text{hp}}}{K_f + \pi[\alpha^0 - \alpha^* p] \beta_{\text{dry}}^{\text{hp}}}, \quad (\text{A1})$$

where $\beta_{\text{dry}}^{\text{hp}} = G_{\text{dry}}^{\text{hp}} \left(3K_{\text{dry}}^{\text{hp}} + G_{\text{dry}}^{\text{hp}} \right) / \left(3K_{\text{dry}}^{\text{hp}} + 4G_{\text{dry}}^{\text{hp}} \right)$.

For cracks, generally, we have $\alpha^0 < 0.01$. Hence, for liquid-saturated condition, we have $\pi[\alpha^0 - \alpha^* p] \beta_{\text{dry}}^{\text{hp}} \ll K_f$. So that $P_{\text{sat}} \cong K_{\text{dry}}^{\text{hp}} / K_f$ and is independent of α^0 .

Thus, Equation 6 reduces to

$$\frac{K_{\text{dry}}^{\text{hp}}}{K_{\text{mf}}(p)} = 1 + \frac{K_{\text{dry}}^{\text{hp}}}{K_f} \left(1 - \frac{K_f}{K_{\text{dry}}^{\text{hp}}}\right) \int_{\alpha^0 > \alpha^*(p)} c(\alpha^0) \left(1 - \frac{\alpha^*(p)}{\alpha^0}\right) d\alpha^0, \quad (\text{A2})$$

From David and Zimmerman (2012), we have

$$\int_{\alpha^0 > \alpha^*(p)} c(\alpha^0) \left(1 - \frac{\alpha^*(p)}{\alpha^0}\right) d\alpha^0 = \phi_c, \quad (\text{A3})$$

and hence, Equation A2 further simplifies to

$$\frac{1}{K_f(p)} = \frac{1}{K_{\text{dry}}^{\text{hp}}} + \left(\frac{1}{K_f} - \frac{1}{K_{\text{dry}}^{\text{hp}}}\right) \phi_c. \quad (\text{A4})$$

Since $\frac{1}{K_{\text{dry}}^{\text{hp}}} \ll \frac{1}{K_f}$ and $\frac{1}{K_f} - \frac{1}{K_{\text{dry}}^{\text{hp}}} \approx \frac{1}{K_f} - \frac{1}{K_g}$, Equation A4 is consistent with the MJ Equation 8 for bulk modulus.

A.2 Shear Modulus

The shear excess compliance for fluid-saturated spheroidal cracks is given by (Berryman, 1980)

$$Q_{\text{sat}} = \frac{1}{5} \left[1 + \frac{8G_{\text{dry}}^{\text{hp}}}{\pi\alpha^0 (K_{\text{dry}}^{\text{hp}} + 2\beta_{\text{dry}}^{\text{hp}})} + 2 \frac{K_f + \frac{2}{3}K_{\text{dry}}^{\text{hp}}}{K_f + \pi\alpha^0\beta_{\text{dry}}^{\text{hp}}} \right] = Q_{\text{dry}} + \frac{1}{5} \left(2 + \frac{4G_{\text{dry}}^{\text{hp}}}{3K_f} - \frac{4G_{\text{dry}}^{\text{hp}}}{3\pi\alpha^0\beta_{\text{dry}}^{\text{hp}}} \right). \quad (\text{A5})$$

Substituting this relationship and Equation 1 into Equation 11 gives

$$\frac{1}{G_{\text{mf}}(p)} = \frac{1}{G_{\text{dry}}(p)} - \frac{4}{15} \left(\frac{1}{K_{\text{dry}}(p)} - \frac{1}{K_{\text{dry}}^{\text{hp}}} \right) + \frac{2}{5} \frac{1}{G_{\text{dry}}^{\text{hp}}} \phi_c + \frac{4}{15} \frac{1}{K_f} \phi_c. \quad (\text{A6})$$

According to Equation A4, we get

$$\frac{4}{15} \left(\frac{1}{K_{\text{mf}}(p)} - \frac{1}{K_{\text{dry}}^{\text{hp}}} \right) = \frac{4}{15} \left(\frac{1}{K_f} - \frac{1}{K_{\text{dry}}^{\text{hp}}} \right) \phi_c. \quad (\text{A7})$$

Substituting Equation A7 into Equation A6 leads to

$$\frac{1}{G_{\text{mf}}(p)} = \frac{1}{G_{\text{dry}}(p)} + \frac{4}{15} \left(\frac{1}{K_{\text{mf}}(p)} - \frac{1}{K_{\text{dry}}^{\text{hp}}} \right) + \frac{2}{5} \frac{1}{G_{\text{dry}}^{\text{hp}}} \phi_c + \frac{4}{15} \frac{1}{K_{\text{dry}}^{\text{hp}}} \phi_c. \quad (\text{A8})$$

Recalling that $\phi_c \ll 1$, Equation A8 reduces to the MJG Equation 9.

Appendix B

David and Zimmerman (2012) showed that crack aspect ratio distribution α^0 at zero pressure can be computed by the integral

$$\alpha^0 = \frac{3}{4\pi} \int_{\Gamma^0}^{\Gamma(\alpha)} \frac{(C_{\text{dry}}(\Gamma) - C_{\text{dry}}^{\text{hp}}) dp}{\Gamma d\Gamma}, \quad (\text{B1})$$

where $C_{\text{dry}}^{\text{hp}}$ is the inverse of $K_{\text{dry}}^{\text{hp}}$, $C_{\text{dry}}(\Gamma)$ is the compressibility of dry rock as a function of crack density, which is given by

$$C_{\text{dry}}(\Gamma) = C_{\text{dry}}^{\text{hp}} + C_{\text{dry}}^{\text{hp}} \frac{16 \left[1 - \left(\nu_{\text{dry}}^{\text{hp}} \right)^2 \right] \Gamma}{9 \left(1 - 2\nu_{\text{dry}}^{\text{hp}} \right)}, \quad (\text{B2})$$

where Γ^0 can be computed from C_{dry} at zero pressure using Equation B2.

Combining Equations B1 and B2 gives

$$\alpha^0 = C_{\text{dry}}^{\text{hp}} \frac{4 \left[1 - \left(\nu_{\text{dry}}^{\text{hp}} \right)^2 \right]}{3\pi \left(1 - 2\nu_{\text{dry}}^{\text{hp}} \right)} \int_{\Gamma^0}^{\Gamma(\alpha)} \frac{dp}{d\Gamma} d\Gamma. \quad (\text{B3})$$

From Equation 16, it is convenient to obtain

$$\frac{dp}{d\Gamma} = -\frac{\hat{p}}{\Gamma}. \quad (\text{B4})$$

Substitution of Equation B4 into Equation B2 gives

$$\alpha^0 = C_{\text{dry}}^{\text{hp}} \frac{4 \left[1 - \left(\nu_{\text{dry}}^{\text{hp}} \right)^2 \right]}{3\pi \left(1 - 2\nu_{\text{dry}}^{\text{hp}} \right)} \hat{p} \ln \frac{\Gamma^0}{\Gamma}. \quad (\text{B5})$$

This relationship suggests that an exponential pressure dependency of compressibility implies an exponential distribution of crack aspect ratios.

Data Availability Statement

The data can be found in Fortin et al. (2007), David and Zimmerman (2012), and Borgomano et al. (2019).

Acknowledgments

The authors are grateful to Samuel Chapman, Jerome Fortin, Stanislav Glubokovskikh, Junxin Guo, Maxim Lebedev, and Vassili Mikhaltsevitch for constructive discussions and comments. We are especially grateful to Emmanuel David, who critically reviewed an earlier version of the manuscript, including mathematical derivations, and made many insightful comments and useful suggestions. The authors thank Yves Guéguen, Erik Saenger, and an anonymous reviewer for their careful reading of our manuscript and many insightful comments and suggestions. The authors thank the sponsors of the Curtin Reservoir Geophysics Consortium (CRGC) and the China Scholarship Council (CSC) for financial support. The authors declare that there is no conflict of interest concerning the publication of this paper.

References

- Alkhimenkov, Y., Caspari, E., Gurevich, B., Barbosa, N. D., Glubokovskikh, S., Hunziker, J., & Quintal, B. (2020). Frequency-dependent attenuation and dispersion caused by squirt flow: Three-dimensional numerical study. *Geophysics*, *85*(3), MR129–MR145.
- Batzle, M. L., Han, D. H., & Hofmann, R. (2006). Fluid mobility and frequency-dependent seismic velocity—Direct measurements. *Geophysics*, *71*(1), N1–N9.
- Berryman, J. G. (1980). Long-wavelength propagation in composite elastic media II. Ellipsoidal inclusions. *The Journal of the Acoustical Society of America*, *68*(6), 1820–1831.
- Borgomano, J. V., Pimienta, L. X., Fortin, J., & Guéguen, Y. (2019). Seismic dispersion and attenuation in fluid-saturated carbonate rocks: Effect of microstructure and pressure. *Journal of Geophysical Research: Solid Earth*, *124*(12), 12,498–12,522.
- Brown, R. J., & Korrington, J. (1975). On the dependence of the elastic properties of a porous rock on the compressibility of the pore fluid. *Geophysics*, *40*(4), 608–616.
- Chapman, M., Zatsepin, S. V., & Crampin, S. (2002). Derivation of a microstructural poroelastic model. *Geophysical Journal International*, *151*(2), 427–451.
- Chapman, S., Borgomano, J. V., Yin, H., Fortin, J., & Quintal, B. (2019). Forced oscillation measurements of seismic wave attenuation and stiffness moduli dispersion in glycerine-saturated Berea sandstone. *Geophysical Prospecting*, *67*(4), 956–968.
- Ciz, R., Saenger, E. H., Gurevich, B., & Shapiro, S. A. (2009). Temperature-dependent poroelastic and viscoelastic effects on microscale—Modelling of seismic reflections in heavy oil reservoirs. *Geophysical Journal International*, *176*(3), 822–832.
- Ciz, R., & Shapiro, S. A. (2007). Generalization of Gassmann equations for porous media saturated with a solid material. *Geophysics*, *72*(6), A75–A79.
- Collet, O., & Gurevich, B. (2016). Frequency dependence of anisotropy in fluid saturated rocks—Part II: Stress-induced anisotropy case. *Geophysical Prospecting*, *64*(4), 1085–1097.
- David, E., & Zimmerman, R. W. (2011). Compressibility and shear compliance of spheroidal pores: Exact derivation via the Eshelby tensor, and asymptotic expressions in limiting cases. *International Journal of Solids and Structures*, *48*(5), 680–686.
- David, E., & Zimmerman, R. W. (2012). Pore structure model for elastic wave velocities in fluid-saturated sandstones. *Journal of Geophysical Research*, *117*, B07210.
- David, E., & Zimmerman, R. W. (2013). Model for frequency-dependence of elastic wave velocities in porous rocks. Paper presented at the Poromechanics V: Proceedings of the Fifth Biot Conference on Poromechanics, C. Hellmich, B. Pichler, and D. Adam.
- de Paula, O. B., Pervukhina, M., Makarynska, D., & Gurevich, B. (2012). Modelling squirt dispersion and attenuation in fluid-saturated rocks using pressure dependency of dry ultrasonic velocities. *Geophysics*, *77*(3), WA157–WA168.
- Eberhart-Phillips, D., Han, D., & Zoback, M. (1989). Empirical relationships among seismic velocity, effective pressure, porosity, and clay content in sandstone. *Geophysics*, *54*(1), 82–89.

- Fortin, J., Guéguen, Y., & Schubnel, A. (2007). Effects of pore collapse and grain crushing on ultrasonic velocities and V_p/V_s . *Journal of Geophysical Research*, *112*, B08207. <https://doi.org/10.1029/2005JB004005>
- Gassmann, F. (1951). Über die Elastizität poröser Medien: Vierteljahrsschrift der Naturforschenden Gesellschaft in Zürich. *96*, 1–23.
- Glubokovskikh, S., Gurevich, B., & Saxena, N. (2016). A dual-porosity scheme for fluid/solid substitution. *Geophysical Prospecting*, *64*(4), 1112–1121.
- Gurevich, B., Makarynska, D., de Paula, O. B., & Pervukhina, M. (2010). A simple model for squirt-flow dispersion and attenuation in fluid-saturated granular rocks. *Geophysics*, *75*(6), N109–N120.
- Gurevich, B., Makarynska, D., & Pervukhina, M. (2009a). Are penny-shaped cracks a good model for compliant porosity? In SEG Technical Program Expanded Abstracts 2009 (pp. 3431–3435): Society of Exploration Geophysicists.
- Gurevich, B., Makarynska, D., & Pervukhina, M. (2009b). Ultrasonic moduli for fluid-saturated rocks: Mavko-Jizba relations rederived and generalized. *Geophysics*.
- Han, D.-H., Nur, A., & Morgan, D. (1986). Effects of porosity and clay content on wave velocities in sandstones. *Geophysics*, *51*(11), 2093–2107.
- Jones, T. D. (1986). Pore fluids and frequency-dependent wave propagation in rocks. *Geophysics*, *51*(10), 1939–1953.
- Mavko, G., & Jizba, D. (1991). Estimating grain-scale fluid effects on velocity dispersion in rocks. *Geophysics*, *56*(12), 1940–1949.
- Mavko, G., & Mukerji, T. (2013). Estimating Brown-Korrington constants for fluid substitution in multiminerals rocks. *Geophysics*, *78*(3), L27–L35.
- Mavko, G., & Nur, A. (1975). Melt squirt in the asthenosphere. *Journal of Geophysical Research*, *80*(11), 1444–1448.
- Mavko, G., & Nur, A. (1978). The effect of nonelliptical cracks on the compressibility of rocks. *Journal of Geophysical Research*, *83*(B9), 4459–4468.
- Mikhailitsevich, V., Lebedev, M., & Gurevich, B. (2014). A laboratory study of low-frequency wave dispersion and attenuation in water-saturated sandstones. *The Leading Edge*, *33*, 616–622.
- Mikhailitsevich, V., Lebedev, M., & Gurevich, B. (2015). A laboratory study of attenuation and dispersion effects in glycerol-saturated Berea sandstone at seismic frequencies. In *SEG Technical Program Expanded Abstracts 2015* (pp. 3085–3089). Society of Exploration Geophysicists.
- Mikhailitsevich, V., Lebedev, M., & Gurevich, B. (2016). Validation of the laboratory measurements at seismic frequencies using the Kramers-Kronig relationship. *Geophysical Research Letters*, *43*, 4986–4991. <https://doi.org/10.1002/2016gl069269>
- Mikhailitsevich, V., Lebedev, M., Gurevich, B., Sun, Y., & Glubokovskikh, S. (2019). A seismic-frequency laboratory study of solid substitution in Bentheim sandstone. *Journal of Geophysical Research: Solid Earth*, *124*, 5492–5499. <https://doi.org/10.1029/2018jb016960>
- Morlier, P. (1971). Description of the state of rock fracturization through simple non-destructive tests. *Rock Mechanics*, *3*(3), 125–138.
- Murphy, W. F. (1982). Effects of microstructure and pore fluids on the acoustic properties of granular sedimentary materials. Ph. D. dissertation, Stanford University.
- Murphy, W. F., Winkler, K. W., & Kleinberg, R. L. (1986). Acoustic relaxation in sedimentary rocks: Dependence on grain contacts and fluid saturation. *Geophysics*, *51*(3), 757–766.
- Norris, A. N. (1985). A differential scheme for the effective moduli of composites. *Mechanics of Materials*, *4*(1), 1–16.
- O'Connell, R. J., & Budiansky, B. (1974). Seismic velocities in dry and saturated cracked solids. *Journal of Geophysical Research*, *79*(35), 5412–5426.
- O'Connell, R. J., & Budiansky, B. (1977). Viscoelastic properties of fluid-saturated cracked solids. *Journal of Geophysical Research*, *82*(36), 5719–5735.
- Paffenholz, J., & Burkhardt, H. (1989). Absorption and modulus measurements in the seismic frequency and strain range on partially saturated sedimentary rocks. *Journal of Geophysical Research*, *94*(B7), 9493–9507.
- Palmer, I., & Traviolia, M. (1980). Attenuation by squirt flow in undersaturated gas sands. *Geophysics*, *45*(12), 1780–1792.
- Pimienta, L. X., Borgomano, J. V., Fortin, J., & Guéguen, Y. (2017). Elastic dispersion and attenuation in fully saturated sandstones: Role of mineral content, porosity, and pressures. *Journal of Geophysical Research: Solid Earth*, *122*, 9950–9965. <https://doi.org/10.1002/2017jb014645>
- Pimienta, L. X., Fortin, J., & Guéguen, Y. (2015). Bulk modulus dispersion and attenuation in sandstones. *Geophysics*, *80*(2), D111–D127.
- Pride, S. R., Berryman, J. G., & Harris, J. M. (2004). Seismic attenuation due to wave-induced flow. *Journal of Geophysical Research*, *109*, B01201. <https://doi.org/10.1029/2003jb002639>
- Salganik, R. (1973). Mechanics of bodies with many cracks. *Mechanics of Solids*, *8*(4), 135–143.
- Saxena, N., Mavko, G., Hofmann, R., Gurevich, B., Glubokovskikh, S., Aliyeva, S., & Dutta, P. (2016). Rock-physics models for heavy-oil and organic-solid substitution. *The Leading Edge*, *35*(6), 506–510.
- Shapiro, S. A. (2003). Elastic piezosensitivity of porous and fractured rocks. *Geophysics*, *68*(2), 482–486.
- Spencer, J. W. Jr. (1981). Stress relaxations at low frequencies in fluid-saturated rocks: Attenuation and modulus dispersion. *Journal of Geophysical Research*, *86*(B3), 1803–1812.
- Sun, Y., Carcione, J. M., & Gurevich, B. (2020). Squirt-flow seismic dispersion models: A comparison. *Geophysical Journal International*, *222*(3), 2068–2082.
- Sun, Y., Gurevich, B., Glubokovskikh, S., Lebedev, M., Squelch, A., Arns, C., & Guo, J. (2019). A solid/fluid substitution scheme constrained by pore-scale numerical simulations. *Geophysical Journal International*, *220*(3), 1804–1812.
- Sun, Y., Gurevich, B., Lebedev, M., Glubokovskikh, S., Mikhailitsevich, V., & Guo, J. (2018). A triple porosity scheme for fluid/solid substitution: Theory and experiment. *Geophysical Prospecting*, *67*(4), 888–899.
- Tsai, H.-C., & Lee, C.-C. (1998). Compressive stiffness of elastic layers bonded between rigid plates. *International Journal of Solids and Structures*, *35*(23), 3053–3069.
- Vernik, L., & Hamman, J. (2009). Stress sensitivity of sandstones and 4D applications. *The Leading Edge*, *28*(1), 90–93.
- Walsh, J. (1965). The effect of cracks on the compressibility of rock. *Journal of Geophysical Research*, *70*(2), 381–389.
- Winkler, K. W. (1986). Estimates of velocity dispersion between seismic and ultrasonic frequencies. *Geophysics*, *51*(1), 183–189.
- Wulff, A. M., & Burkhardt, H. (1997). Mechanisms affecting ultrasonic wave propagation in fluid-containing sandstones under high hydrostatic pressure. *Journal of Geophysical Research*, *102*(B2), 3043–3050.
- Wyllie, M., Gardner, G., & Gregory, A. (1962). Studies of elastic wave attenuation in porous media. *Geophysics*, *27*(5), 569–589.
- Yurikov, A., Lebedev, M., Gor, G. Y., & Gurevich, B. (2018). Sorption-induced deformation and elastic weakening of Bentheim sandstone. *Journal of Geophysical Research: Solid Earth*, *123*, 8589–8601. <https://doi.org/10.1029/2018jb016003>
- Zhu, X., & McMechan, G. A. (1990). Direct estimation of the bulk modulus of the frame in a fluid-saturated elastic medium by Biot theory. In *SEG Technical Program Expanded Abstracts 1990* (pp. 787–790): Society of Exploration Geophysicists.
- Zimmerman, R. W. (1991). Aspect Ratio Distributions. In *Compressibility of sandstones* (pp. 128–139). Amsterdam; Oxford; New York: Elsevier.

2.3 A triple porosity scheme for fluid/solid substitution: theory and experiment

A triple porosity scheme for fluid/solid substitution: theory and experiment

Yongyang Sun^{1*}, Boris Gurevich^{1,2}, Maxim Lebedev¹, Stanislav Glubokovskikh¹, Vassili Mikhaltsevitch¹ and Junxin Guo¹

¹Department of Exploration Geophysics, Curtin University, GPO Box U1987, Perth, WA 6845, Australia, and ²CSIRO Energy, 26 Dick Perry Avenue, Kensington, WA 6151, Australia

Received September 2017, revision accepted July 2018

ABSTRACT

Quantifying the effects of pore-filling materials on elastic properties of porous rocks is of considerable interest in geophysical practice. For rocks saturated with fluids, the Gassmann equation is proved effective in estimating the exact change in seismic velocity or rock moduli upon the changes in properties of pore infill. For solid substance or viscoelastic materials, however, the Gassmann theory is not applicable as the rigidity of the pore fill (either elastic or viscoelastic) prevents pressure communication in the pore space, which is a key assumption of the Gassmann equation. In this paper, we explored the elastic properties of a sandstone sample saturated with fluid and solid substance under different confining pressures. This sandstone sample is saturated with octadecane, which is a hydrocarbon with a melting point of 28°C, making it convenient to use in the lab in both solid and fluid forms. Ultrasonically measured velocities of the dry rock exhibit strong pressure dependency, which is largely reduced for the filling of solid octadecane. Predictions by the Gassmann theory for the elastic moduli of the sandstone saturated with liquid octadecane are consistent with ultrasonic measurements, but underestimate the elastic moduli of the sandstone saturated with solid octadecane. Our analysis shows that the difference between the elastic moduli of the dry and solid-octadecane-saturated sandstone is controlled by the squirt flow between stiff, compliant, and the so-called intermediate pores (with an aspect ratio larger than that of compliant pore but much less than that of stiff pores). Therefore, we developed a triple porosity model to quantify the combined squirt flow effects of compliant and intermediate pores saturated with solid or viscoelastic infill. Full saturation of remaining stiff pores with solid or viscoelastic materials is then considered by the lower embedded bound theory. The proposed model gave a reasonable fit to the ultrasonic measurements of the elastic moduli of the sandstone saturated with liquid or solid octadecane. Comparison of the predictions by the new model to other solid substitution schemes implied that accounting for the combined effects of compliant and intermediate pores is necessary to explain the solid squirt effects.

Key words: Rock physics, Elastic, Fluid.

INTRODUCTION

Quantifying the exact change in seismic velocity or elastic moduli of porous rocks upon changes in properties of pore

infill is of considerable interest in geophysical practice. Naturally occurring pore infill can be gases (e.g. methane, CO₂, helium and steam), liquids (e.g. brine, light oil, heavy oil and magma) and solids (e.g. clay, bitumen, kerogen, salt, ice and gas hydrates; Saxena and Mavko 2015). For rocks

*E-mail: yongyang.sun@postgrad.curtin.edu.au

saturated with fluids, the Gassmann equation (Gassmann 1951) is widely proved effective in predicting the change in quasistatic undrained rock moduli upon change in pore-fluid properties without any detailed knowledge of pore geometry. (The predictions by the Gassmann equation only depend on the porosity, and fluid and frame stiffnesses. The Gassmann theory also stipulates that fluid has no effects on the overall shear modulus.) For rocks saturated with solid or viscoelastic materials, however, the Gassmann theory is not applicable as the finite rigidity of the pore-filling material (either solid or viscoelastic) prevents pressure communication throughout the entire pore space, which is a key assumption of the Gassmann theory.

Ciz and Shapiro (2007; C&S) proposed an extension of the Gassmann equation to the case of solid substance filling by defining a new heuristic parameter, which is related to volume-averaged strain within the pore space. This parameter depends on the pore geometry and the elastic moduli of the pore infill. However, it is hard to estimate in practice. Hence, they proposed approximated equations, which reduce to the Gassmann equation for bulk modulus and a similar equation for shear modulus. But Saxena and Mavko (2014) pointed out the C&S model tends to largely underestimate the elastic moduli of solid-filled rocks. Hence, Mavko and Saxena (2013) and Saxena and Mavko (2014) derived generalized equations, referred as the embedded bound theory, for fluid/solid substitution under a general case of non-uniform (spatially variant) stresses. The relations are built on recursive use of the Hashin and Shtrikman (1963) bounds for two-phase materials. This guarantees that the substitution results are physically realizable. General substitution equations require the knowledge of microstructural information, which is usually unavailable as the digital rock images of rocks cannot be used to resolve the very thin pores. Indeed, Makarynska *et al.* (2010) showed that the presence of pores with a low aspect ratio leads to a dramatic increase of the difference between effective shear moduli of the dry and solid saturated rock, an effect similar to the stiffening effect of squirt flow in fluid-filled rocks at ultrasonic frequencies. This similarity was recognized by Leurer and Dvorkin (2006) who proposed the term 'solid squirt' to describe the stiffening of the compliant grain contacts by a solid infill. More generally, the works of Leurer and Dvorkin (2006) and Makarynska *et al.* (2010) highlight the fact that the presence of pores with a range of compliances leads to strong heterogeneity of the stress field in the pore infill, which in turn has a strong effect on the effective moduli of the solid-saturated rocks. Here and next, the compliance of the pores refers to their behaviour in the dry rock, and is controlled by

their aspect ratio: the smaller the aspect ratio, the larger the compliance.

To take into account the heterogeneity of the stresses in pore space quantitatively, Saxena and Mavko (2015) extended the approach of Gurevich, Makarynska and Perukhina (2009) to model the effects of solid-filled compliant pores on the overall elastic stiffness using the formalism proposed by Sayers and Kachanov (1991) and Sayers and Kacganov (1995). However, we note that this scheme has an important assumption that confining pressure induces different stress gradients within compliant and stiff pores, both of which are still spatially uniform. This implies that compliant pores are assumed to be completely isolated from stiff pores, which is analogous to high-frequency limit. Hence, this scheme is not consistent with the Gassmann equation in the low-frequency limit. To overcome this inconsistency, Glubokovskikh, Gurevich and Saxena (2016) employed the solution of Tsai and Lee (1998) to model the deformation of a grain-to-grain contact open into a stiff pore space. Each compliant pore is approximated as a plane circular interlayer with traction-free edges. Comparison of the model predictions against laboratory measurements shows that this model accurately predicts the general trend but shows some discrepancy, especially for shear modulus. They attributed the mismatch to the oversimplified rock microstructure underlying the theoretical mode. Besides, their predictions are close to those given by the lower embedded bound theory, which defines the smallest change upon solid substitution. Saxena and Mavko (2015) argued that for porous rocks with a mix of stiff and soft or compliant pores, the true change in effective elastic moduli will be larger than that predicted by the lower embedded bound theory as this theory corresponds to the case of equilibrated pressure communication in pore space without any compliant pores. To explore this issue further, we conducted solid substitution experiments on a Bentheim sandstone sample. The sample is prepared from the same block as the samples used for experiments described by Saenger *et al.* (2016). Our experiments, reported later in this paper, show that the dual porosity scheme of Glubokovskikh *et al.* (2016) is not sufficient to explain the data. When studying dispersion in a large number of fluid-saturated sandstones, De Paula *et al.* (2012) showed that the characteristic frequency of typical compliant pores lies close to the seismic frequency domain, but is well below the ultrasonic frequency. Thus, compliant and stiff pores might not fully account for the solid squirt effects in the experiments. Besides, the measured elastic moduli of a rock with only equant pores present, are significantly smaller than those given by the effective medium model for spherical pores

(Berryman 1980). Hence, De Paula *et al.* (2012) argued that the squirt effects are caused by the presence of the so-called intermediate pores, which are softer than stiff pores but much stiffer than compliant pores. This provides a good prospective to better characterize the solid squirt effects.

In this work, we generalize the Glubokovskikh *et al.* (2016) model to the case of triple pore structure, including stiff, compliant and the so-called intermediate pores, in order to account for the solid squirt effects. To this end, we used the derived relations to estimate the unrelaxed rock frame moduli that account for the solid squirt effects. The unrelaxed rock frame contains compliant and intermediate pores filled with solid or viscoelastic materials. The remaining stiff pores are then saturated with solid or viscoelastic materials by the lower embedded bound theory to predict the undrained rock moduli. The validity and applicability of the developed model is tested using ultrasonic measurements of a sandstone sample saturated with octadecane, a hydrocarbon with a melting point of 28°C, which makes it convenient to use both in solid and fluid forms in the laboratory. We also compare the new solid substitution scheme to the ones discussed above.

THEORETICAL MODEL

We consider a typical rock with bulk modulus K_g and shear modulus μ_g . The pore space is divided into three parts – stiff ϕ_s , compliant ϕ_c and intermediate pores ϕ_m . Effective porosity is characterized by the sum of three types of pores as $\phi = \phi_s + \phi_c + \phi_m$. By construction, each typical intermediate pore is defined as a pore with an aspect ratio larger than that of compliant pores but much less than that of stiff pores. This implies that both compliant and intermediate pores are deformed to much larger degree than do stiff pores. In that case, the effects of stiff, compliant and intermediate pores saturated with solid or viscoelastic substances can be treated successively. To estimate the fully saturated elastic moduli of a rock with a mix of stiff, compliant and intermediate pores, a plausible approach is to perform the computation in three steps. First, we conduct analysis of the pressure-dependent dry rock moduli (K_{dry} , μ_{dry}) to obtain the parameters for fluid/solid substitution. Second, we substitute these parameters into the derived relations to estimate the unrelaxed rock frame moduli where both compliant and intermediate pores are saturated with solid or viscoelastic materials but stiff pores still remain empty. Once the unrelaxed rock frame moduli are known, the undrained rock moduli can be obtained by the lower embedded bound theory, appropriate for stiff pores embedded into homogeneous rock matrix.

Compliant, intermediate and stiff porosity

Following Mavko and Jizba (1991) and using the discontinuity formalism by Sayers and Kachanov (1991) and Sayers and Kacganov (1995), Gurevich *et al.* (2009) represented the expressions of unrelaxed rock frame moduli as

$$\frac{1}{K_{ufc}} = \frac{1}{K_{bc}} + sB_{Nc} \quad (1)$$

and

$$\frac{1}{\mu_{ufc}} = \frac{1}{\mu_{bc}} + \frac{4}{15}sB_{Nc} + \frac{2}{5}sB_{Tc}, \quad (2)$$

where K_{bc} and μ_{bc} are the dry rock frame moduli of a hypothetical rock with compliant pores closed and stiff porosity equal to the unstressed value. The symbol $s = A/V$ is surface-to-volume ratio of all discontinuities. B_{Nc} and B_{Tc} are the normal and tangential specific compliance of a typical compliant inclusion. When compliant pores are empty, equations (1) and (2) reduce to

$$\frac{1}{K_{dry}} = \frac{1}{K_{bc}} + sB_{Nc}^{dry} \quad (3)$$

and

$$\frac{1}{\mu_{dry}} = \frac{1}{\mu_{bm}} + \frac{4}{15}sB_{Nc}^{dry} + \frac{2}{5}sB_{Tc}^{dry}, \quad (4)$$

where B_{Nc}^{dry} and B_{Tc}^{dry} are the dry normal and tangential specific compliance of a typical compliant inclusion.

Following De Paula *et al.* (2012), intermediate porosity will exhibit an exponential decay with increasing confining pressure, similar to compliant porosity but at much higher confining pressures. In analogy to equations (1)–(4), the expressions of unrelaxed rock frame moduli at much higher confining pressures when all compliant pores are closed can be written as

$$\frac{1}{K_{ufm}} = \frac{1}{K_{bm}} + sB_{Nm} \quad (5)$$

and

$$\frac{1}{\mu_{ufm}} = \frac{1}{\mu_{bm}} + \frac{4}{15}sB_{Nm} + \frac{2}{5}sB_{Tm}, \quad (6)$$

where K_{bm} and μ_{bm} are the dry rock frame moduli of a hypothetical rock with both compliant and intermediate pores closed and stiff porosity equal to the unstressed value. B_{Nm} and B_{Tm} are the normal and tangential specific compliance of a typical intermediate inclusion. Furthermore, the deformation of stiff pores at relatively large confining pressures is

neglected. When all intermediate pores are empty, equations (5) and (6) also reduce to

$$\frac{1}{K_{dry}} = \frac{1}{K_{hm}} + s B_{Nm}^{dry} \quad (7)$$

and

$$\frac{1}{\mu_{dry}} = \frac{1}{\mu_{hm}} + \frac{4}{15} s B_{Nm}^{dry} + \frac{2}{5} s B_{Tm}^{dry}, \quad (8)$$

where B_{Nm}^{dry} and B_{Tm}^{dry} are the dry normal and tangential specific compliance of a typical intermediate inclusion. Note that for large confining pressure where all compliant pores are closed, $K_{ufc} = K_{ufm}$. Thus, the variation of elastic moduli of a porous rock due to the combined effects of compliant and intermediate pores can be expressed to the following form:

$$\frac{1}{K_{uf}} = \frac{1}{K_{hm}} + s B_{Nc} + s B_{Nm} \quad (9)$$

and

$$\frac{1}{\mu_{uf}} = \frac{1}{\mu_{hm}} + \frac{4}{15} (s B_{Nc} + s B_{Nm}) + \frac{2}{5} (s B_{Tc} + s B_{Tm}). \quad (10)$$

Similarly, when both compliant and intermediate pores are empty, equations (9) and (10) reduce to

$$\frac{1}{K_{dry}} = \frac{1}{K_{hm}} + s B_{Nc}^{dry} + s B_{Nm}^{dry} \quad (11)$$

and

$$\frac{1}{\mu_{dry}} = \frac{1}{\mu_{hm}} + \frac{4}{15} (s B_{Nc}^{dry} + s B_{Nm}^{dry}) + \frac{2}{5} (s B_{Tc}^{dry} + s B_{Tm}^{dry}). \quad (12)$$

Subtracting equations (11) and (12) from equations (9) and (10) separately, we obtain the following relations between the elastic moduli of the fully saturated and dry frame:

$$\frac{1}{K_{uf}} - \frac{1}{K_{dry}} = s (B_{Nc} - B_{Nc}^{dry}) + s (B_{Nm} - B_{Nm}^{dry}), \quad (13)$$

$$\begin{aligned} \frac{1}{\mu_{uf}} - \frac{1}{\mu_{dry}} &= \frac{4}{15} [s (B_{Nc} - B_{Nc}^{dry}) + s (B_{Nm} - B_{Nm}^{dry})] \\ &+ \frac{2}{5} [s (B_{Tc} - B_{Tc}^{dry}) + s (B_{Tm} - B_{Tm}^{dry})]. \end{aligned} \quad (14)$$

Equations (13) and (14) give the effective elastic moduli of the unrelaxed rock frame if the pore infill's compliances and the dry frame moduli are known. Note that the equations require the knowledge of relations between the compliances of the dry and saturated with solid or viscoelastic materials both for compliant and intermediate inclusions having K_f

and μ_f . To use equations (13) and (14), we have to establish the relations between the dry and saturated compliances of compliant and intermediate pores. As defined, a typical compliant inclusion is approximated as a plane circular interlayer with traction-free edges. Hudson (1981) first derived and Schoenberg and Douma (1988) reorganized the relations for penny-shaped cracks:

$$\frac{1}{s B_{Nc}} = \frac{1}{s B_{Nc}^{dry}} + \frac{M_{fc}}{\phi_c}, \quad (15)$$

$$\frac{1}{s B_{Tc}} = \frac{1}{s B_{Tc}^{dry}} + \frac{\mu_{fc}}{\phi_c}, \quad (16)$$

where M_{fc} refers to the proper effective compressional stiffness of the pore fill for compliant pores and ϕ_c is the compliant porosity as a function of confining pressure. Similarly, relations between the dry and saturated compliances of intermediate pores can be written as

$$\frac{1}{s B_{Nm}} = \frac{1}{s B_{Nm}^{dry}} + \frac{M_{fm}}{\phi_m} \quad (17)$$

and

$$\frac{1}{s B_{Tm}} = \frac{1}{s B_{Tm}^{dry}} + \frac{\mu_{fm}}{\phi_m}, \quad (18)$$

where M_{fm} refers to the proper effective compressional stiffness of the pore infill for intermediate pores, ϕ_m is the intermediate porosity as a function of confining pressure. There is a comprehensive discussion given by Glubokovskikh *et al.* (2016) about the solution to accurately characterize the circular interlayer. In this work, we employed the solution of Tsai and Lee (1998) suggested by Glubokovskikh *et al.* (2016). The effective compression stiffness of a circular interlayer can be expressed as

$$M_f = K_f + \frac{4}{3} \mu_f - \frac{(K_f - \frac{2}{3} \mu_f)^2}{(K_f + \frac{4}{3} \mu_f) \frac{\alpha \gamma_f I_0(\alpha \gamma_f)}{2 I_1(\alpha \gamma_f)}}, \quad (19)$$

where $\gamma_f = \sqrt{\frac{36 \mu_f}{3 K_f + 4 \mu_f}}$, $\alpha = r/h$ is an inverse aspect ratio of compliant or intermediate pores and I_k refers to a modified Bessel function of the first kind of the order k .

Substituting equations (15)–(18) into equations (13) and (14), we can obtain the relations for estimating the unrelaxed rock frame moduli containing compliant and intermediate pores:

$$\frac{1}{K_{uf}} = \frac{1}{K_{hm}} + \frac{1}{\frac{1}{K_{dry}} - \frac{1}{K_{ufm}} + \frac{M_{fc}}{\phi_c}} + \frac{1}{\frac{1}{K_{ufm}} - \frac{1}{K_{hm}} + \frac{M_{fm}}{\phi_m}}, \quad (20)$$

$$\frac{1}{\mu_{uf}} = \frac{1}{\mu_{hm}} + \frac{4}{15} \left(\frac{1}{\frac{1}{\mu_{dry}} - \frac{1}{\mu_{ufm}} + \frac{\mu_{fc}}{\phi_c}} + \frac{1}{\frac{1}{\mu_{ufm}} - \frac{1}{\mu_{hm}} + \frac{\mu_f}{\phi_m}} \right) + \left(\frac{1}{\frac{1}{\mu_{dry}} - \frac{1}{\mu_{ufm}} - \frac{4}{15} \frac{1}{\frac{1}{K_{dry}} - \frac{1}{K_{ufm}} + \frac{M_{fc}}{\phi_c}} + \frac{5}{2} \frac{\mu_f}{\phi_c}} + \frac{1}{\frac{1}{\mu_{ufm}} - \frac{1}{\mu_{hm}} - \frac{4}{15} \frac{1}{\frac{1}{K_{ufm}} - \frac{1}{K_{hm}} + \frac{M_{fm}}{\phi_m}} + \frac{5}{2} \frac{\mu_f}{\phi_m}} \right). \quad (21)$$

Equations (20) and (21) show that if the pore infill is a fluid, then $M_{fc} = M_{fm} = 0$ and $\mu_f = 0$, and hence the unrelaxed rock frame moduli K_{uf} and μ_{uf} reduce to the initial dry rock moduli K_{dry} and μ_{dry} . This corresponds to the low-frequency limit. In the opposite limiting case, M_f tends to P-wave modulus of the pore infill L_f , which corresponds to the high-frequency limit. This behaviour is expected due to stiffening effect of the adhesion at the top and bottom of the interlayer. This implies that the proposed model for the estimation of unrelaxed rock frame moduli gives a continuous transition from low frequency to high frequency.

Once the unrelaxed rock frame moduli are known, the fully saturated rock moduli can be obtained by the lower embedded bound theory (Saxena and Mavko 2014) since the induced stresses in stiff pores are likely to be approximated equilibrated. For the undrained bulk modulus K_{sat} , this method gives

$$K_{sat} = K_{bc} + \frac{\left(1 - \frac{K_{bc}}{K_g}\right)^2}{\frac{\phi_s}{K_f} + \frac{1 - \phi_s}{K_g} - \frac{K_{bc}}{(K_g)^2}}, \quad (22)$$

where

$$K_{bc} = \frac{(1 - \phi_s) \left(\frac{1}{K_g} - \frac{1}{K_{uf}} \right) + \frac{3\phi_s}{4} \left(\frac{1}{\mu_g} - \frac{1}{\mu_f} \right)}{\frac{1}{K_g} \left(\frac{1}{K_g} - \frac{1}{K_{uf}} \right) + \frac{3\phi_s}{4} \left(\frac{1}{K_g \mu_g} - \frac{1}{K_{uf} \mu_f} \right)}. \quad (23)$$

Meanwhile, for the undrained shear modulus μ_{sat} , this method gives

$$\mu_{sat} = \mu_{bc} + \frac{\left(1 - \frac{\mu_{bc}}{\mu_g}\right)^2}{\frac{\phi_s}{\mu_f} + \frac{1 - \phi_s}{\mu_g} - \frac{\mu_{bc}}{(\mu_g)^2}}, \quad (24)$$

where

$$\mu_{bc} = \frac{(1 - \phi_s) \left(\frac{1}{\mu_g} - \frac{1}{\mu_{uf}} \right) + \frac{3\phi_s}{4} \left(\frac{1}{\chi_g} - \frac{1}{\chi_f} \right)}{\frac{1}{\mu_g} \left(\frac{1}{\mu_g} - \frac{1}{\mu_{uf}} \right) + \frac{3\phi_s}{4} \left(\frac{1}{\chi_g \mu_g} - \frac{1}{\mu_{uf} \chi_f} \right)} \quad (25)$$

and

$$\chi = \frac{\mu}{8} \frac{9K + 8\mu}{K + 2\mu}. \quad (26)$$

Stress dependency

Equations (20) and (21) require the knowledge of dry rock frame moduli and the fraction of compliant and intermediate pores at different confining pressures as well as other related parameters. These parameters can be extracted from the pressure-dependent dry rock moduli. Shapiro (2003) derived the pressure-dependent dry rock moduli by the presence of stiff and compliant pores, which can be written as

$$K_{dry} = K_{bc} \left[1 + \theta_s \left(\frac{1}{K_{bc}} - \frac{1}{K_g} \right) P - \theta_c \phi_{c0} e^{-\frac{\theta_c P}{K_{bc}}} \right] \quad (27)$$

and

$$\mu_{dry} = \mu_{bc} \left[1 + \theta_{s\mu} \left(\frac{1}{K_{bc}} - \frac{1}{K_g} \right) P - \theta_{c\mu} \phi_{c0} e^{-\frac{\theta_{c\mu} P}{K_{bc}}} \right], \quad (28)$$

where θ_s and θ_c are the pressure sensitivity coefficients for stiff and compliant porosity, $\theta_{s\mu}$ and $\theta_{c\mu}$ are the shear pressure sensitivity coefficients for stiff and compliant porosity, respectively. ϕ_{c0} is value of compliant porosity in the unstressed rocks. Shapiro (2003) further gave the pressure-dependent stiff and compliant porosity to the following form:

$$\phi_s(P) = \phi_{s0} - P \left(\frac{1}{K_{bc}} - \frac{1}{K_g} \right), \quad (29)$$

$$\phi_c(P) = \phi_{c0} e^{-\frac{\theta_c P}{K_{bc}}}. \quad (30)$$

Indeed, Pervukhina, Gurevich, Dewhurst, and Siggins (2010) verified the linear relationship between the rock moduli and stiff porosity and the exponential relationship between the rock moduli and compliant porosity up to the pressure of 100 MPa with the simultaneous measurements of ultrasonic velocities and porosity for a suit of sandstones. As defined, intermediate pores tend to deform to much greater extent than stiff pores. Thus, the intermediate porosity will exhibit an exponential decay with increasing confining pressure, which is similar to the compliant porosity but at much higher confining pressures

$$\phi_m(P) = \phi_{m0} e^{-\frac{\theta_m P}{K_{bm}}}, \quad (31)$$

where ϕ_{m0} is the initial value of intermediate porosity in the unstressed rocks, θ_m is the bulk sensitivity coefficient for intermediate pores. Thus, closure of intermediate porosity at much higher confining pressure tend to affect the dry rock moduli in a similar way as closing of compliant porosity at low confining pressures, which can be expressed as

$$K_{ufm}(P) = K_{bm} \left[1 - \theta_m \phi_{m0} e^{-\frac{\theta_m P}{K_{bm}}} \right] \quad (32)$$

and

$$\mu_{ufm}(P) = \mu_{bm} \left[1 - \theta_{\mu m} \phi_{m0} e^{-\frac{\theta_{\mu m} P}{K_{bm}}} \right]. \quad (33)$$

Note that for much higher confining pressures (above 50–100 MPa, suggested by De Paula *et al.* 2012), $K_{ufm} = K_{uf}$ and $\mu_{ufm} = \mu_{uf}$. As a result, the variation of the pressure-dependent dry rock moduli due to the combined effect of compliant and intermediate porosity can be written as

$$K_{dry} = K_{bm} \left[1 - \theta_m \phi_{m0} e^{-\frac{\theta_m P}{K_{bm}}} - (1 + \phi_{m0}) \theta_c \phi_{c0} e^{-\frac{\theta_c P}{K_{bc}}} \right] \quad (34)$$

$$\mu_{dry} = \mu_{bm} \left[1 - \theta_{\mu m} \phi_{m0} e^{-\frac{\theta_{\mu m} P}{K_{bm}}} - (1 + \phi_{m0}) \theta_c \phi_{c0} e^{-\frac{\theta_c P}{K_{bc}}} \right]. \quad (35)$$

Equations (34) and (35) give an explicit dependency of the dry rock moduli on pressure and frequency. All the required parameters can be extracted directly from the fitting to the ultrasonic experimental data for dry materials. Note that such estimation of parameters does not involve fitting the moduli of the rock saturated with a fluid or solid infill and hence is independent from those measurements. A detailed workflow is described below.

Parameter estimation workflow

In this section, we outline the workflow to be applied to the ultrasonic dry rock moduli under different confining pressures. This workflow will be utilized to derive the fraction of stiff, compliant, and intermediate porosity and other related parameters for fluid/solid substitution. Then, these parameters will be used to predict fully saturated rock moduli.

- 1 Dry rock moduli K_{dry} and μ_{dry} under different confining pressures are obtained from the ultrasonic compressional and shear velocities V_p and V_s along with density.
- 2 Required parameters (K_{bc} , μ_{bc} , ϕ_{c0} , θ_c , $\theta_{\mu c}$, θ_s , $\theta_{\mu s}$) for compliant and stiff pores are obtained by the least-square fitting of the pressure-dependent dry rock moduli with coupled equations (27) and (28).

- 3 The characteristic aspect ratio α_c of a typical compliant inclusion can be related to the stress sensitivity coefficient θ_c of an elastic medium with a dilute concentration of ellipsoidal cavities (Kuster and Toksöz 1974; Christensen 2005) by equation (36)

$$\theta_c = \frac{K_{bc}(3K_{bc} + 4\mu_{bc})}{\pi \alpha_c \mu_{bc}(3K_{bc} + \mu_{bc})}. \quad (36)$$

- 4 Given that the effects of compliant pores are characterized by an exponential term and the effects of intermediate porosity are characterized by a linear term as stiff porosity at relatively small confining pressures, the values of $K_{ds}(P_i)$ under different confining pressures can be obtained by adding the exponential term $K_{bc} \theta_c \phi_{c0} e^{-\frac{\theta_c P_i}{K_{bc}}}$ from the dry bulk moduli $K_{dry}(P_i)$.

- 5 Similarly, parameters for intermediate porosity (ϕ_{m0} , θ_m , K_{bm} , $\theta_{\mu m}$) are obtained by the least-square fitting of pressure-dependent dry rock moduli with coupled equations (32) and (33) if the pressure-dependent dry rock moduli are available at relatively high confining pressures.

- 6 Or since K_{bm} and μ_{bm} represent the case when both compliant and intermediate pores are closed, the coherent potential approximation (CPA) effective medium model for spherical pores (Berryman 1980) can be employed to compute K_{bm} and μ_{bm} with the aspect ratio estimated from the analysis of micro-CT images for stiff pores. In that case, other related parameters for intermediate porosity can be estimated with the given K_{bm} and μ_{bm} .

- 7 Similar to compliant porosity, the characteristic aspect ratio of intermediate pores can be computed by equation (37)

$$\theta_m = \frac{K_{bm}(3K_{bm} + 4\mu_{bm})}{\pi \alpha_m \mu_{bm}(3K_{bm} + \mu_{bm})}. \quad (37)$$

- 8 Using parameters derived from steps (1) to (7), we can compute the unrelaxed rock frame moduli through equations (20) and (21).

- 9 Then, the elastic moduli of the fully saturated rock can be obtained through equations (22) and (24).

Experimental validation

To examine the validity and applicability of the developed model, we apply it to a sandstone sample saturated with liquid and solid octadecane. It is a hydrocarbon with a melting point of 28°C, which makes it convenient to use both in the fluid and solid form in the laboratory.

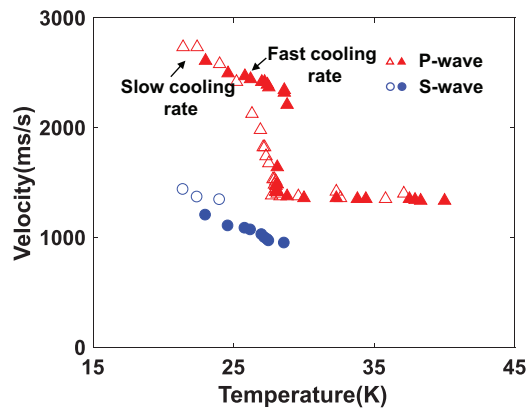


Figure 1 Ultrasonic velocities in octadecane for a range of temperature.

Figure 1 illustrates the results of ultrasonic velocities of octadecane (99% purity, Sigma-Aldrich) measured by transmission method (Crane and Knopp 2009) for a range of temperatures. Measurement is performed at room pressure using piezoelectric S-wave transducers V153 RM (central frequency 0.5 MHz). Such transducer is a source and a receiver of both P- and S-waves (Lebedev *et al.* 2013).

As we observe, the compressional wave velocity remains unchanged while the shear wave velocity vanishes at temperature above 28°C, which behaves like a fluid. Solid and open symbols represent the case of different cooling rate within the measurements. Note that at a slow cooling rate (open symbols), the measured compressional velocity gradually increases with the temperature decreasing. This implies that the transition of liquid–solid is more homogeneous. However, at a fast cooling rate (solid symbols), the measured compressional velocity sharply increased. This implies that some parts of the liquid octadecane pore fill becomes solid while other parts still remain liquid. That is why we observe the shear wave velocity ‘earlier’ than in the previous case.

In this work, we use 3.87 and 1.46 GPa for the bulk and shear moduli of the solid octadecane at temperature 22.4°C. For the liquid octadecane, we use 1.53 GPa for the bulk modulus. The measured density of octadecane is 777 kg/m³. Note that we observe slight density change of octadecane due to the transition from liquid to solid form. This might lead to significant effects on the velocities’ prediction of fully saturated sandstone sample. The other used parameters are summarized in Table 1. The sample rock frame (bulk, 36 GPa; shear, 40 GPa) predominantly comprises mineral quartz (97%) and has a porosity of 23.56%.

Table 1 The parameters used for computation of the sandstone saturated with liquid and solid octadecane

K_g	μ_g	K_f (solid)	μ_f (solid)	K_f (fluid)	ϕ
36 GPa	40 GPa	3.87 GPa	1.46 GPa	1.53 GPa	0.2356

Measurements

For this sample rock, ultrasonic P- and S-wave velocities of the dry and octadecane-saturated (both fluid and solid forms) sandstone as a function of confining pressure are conducted in the range from 0 to 35 MPa using an experimental set-up described in Lebedev *et al.* (2013). Our approach is to measure velocities of dry sandstone firstly under different confining pressures. And then, we put the sandstone on the top of solid octadecane and vacuum the target in vacuum chamber for 24 hours. After that, we start heating the sample and solid octadecane. As we observe, octadecane melts gradually and fluid-form octadecane is moving up into the pore space by capillary force. At the end, the sandstone sample is fully saturated with liquid octadecane, although it is unknown whether this achieves 100% saturation. It might be possible to achieve full saturation using a capillary imbibition method (McCann and Sothcott 1992) but it is unclear if it will work for octadecane. Then, we measure the velocities of liquid-octadecane-saturated sandstone again. After that, we cool the sample down to 20–25°C and carry out the measurement once more.

Within the experiment, pore volume of the sample is vented to the atmosphere. No pore pressure control has been done. This means that for fluid-saturated rock, the pore pressure is zero and the effective pressure is the same as the confining pressure. However, this is not true for solid-filled rock: application of the confining pressure to such rock will induce a heterogeneous stress field within the pore fill, and the effective pressure is unknown. Hence, for solid-filled rocks it is not possible to measure any properties as a function of effective pressure, only as a function of confining pressure.

RESULTS

As aforementioned in the workflow, the estimation of the unrelaxed rock frame moduli requires the knowledge of the pressure-dependent rock moduli and other related parameters for stiff, compliant and intermediate porosity. Our model starts from the fitting of the experimental data to derive these parameters. Non-linear least-square fitting of the pressure-dependent dry rock moduli are implemented on

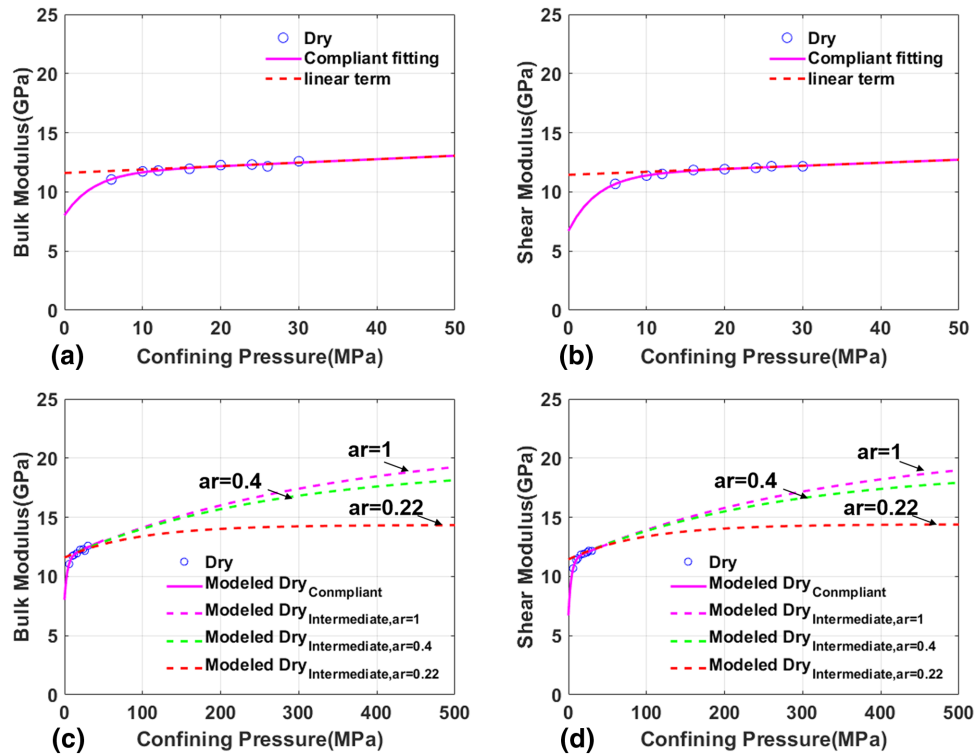


Figure 2 Bulk and shear moduli of a dry Bentheim sandstone versus confining pressure. (a and b) Calculated from ultrasonic velocities up to 50 MPa (blue open circles) and predicted variations due to closing of compliant pores (magenta solid line). (c and d) Predicted variations due to closing of compliant and intermediate pores up to 500 MPa with the assumption of an aspect ratio for stiff pores to 1, 0.4, and 0.22 (dashed lines).

the sandstone sample through coupled equations (27) and (28).

Figure 2(a–d) provides the fitting results of the dry sandstone moduli against the experimental data as a function of confining pressure in the range from 0 to 35 MPa. Blue open circles are the dry bulk and shear moduli calculated from the ultrasonic velocities of a dry Bentheim sandstone sample. And the magenta solid line show the approximation of the elastic moduli through coupled equations (27) and (28). The fitting gives the compressional sensitivity coefficient for compliant pores $\theta_c = 3.16 \times 10^3$, which corresponds to an aspect ratio $\alpha_c = 1.78 \times 10^{-4}$. The results show that the dry rock moduli have a considerable increase with the confining pressure increasing. This trend is well characterized by the combination of an exponential term and a linear term. Note that the exponential term vanishes at pressure 10–20 MPa, which corresponds to the closure of soft or compliant pores. Thus, we can obtain the bulk and shear moduli of the dry sandstone in high pressure limit, where all compliant pores are closed and only stiff pores are left, for 11.60 and 11.44 GPa, respectively.

Shapiro (2003) assumes that stiff pores have an aspect ratio of order one (the so-called equant pores, Thomsen 1995), and concludes that the contribution of the deformation of stiff porosity is small compared to that of compliant porosity, and thus can be neglected. However, compared to the value computed by the coherent potential approximation (CPA) for spherical pores 29.11 GPa, we observe an obvious difference of 10 GPa. This implies that the mismatch between the fitted dry rock moduli in the high pressure limit and the estimated elastic moduli of a rock with stiff porosity only by the CPA cannot be explained by the presence of stiff pores with an aspect ratio of unity. Indeed, several experimental studies show that in many cases, the contribution of stiff porosity term in equations (27) and (28) (i.e. the term that varies linearly with confining pressure at relatively small pressures) is significant (Eberhart-Phillips *et al.* 1989; Vernik and Hamman 2009; Gurevich *et al.* 2010). In other words, this suggests that in addition to stiff and compliant pores, the entire pore space contains pores with an aspect ratio larger than that of compliant pores but much

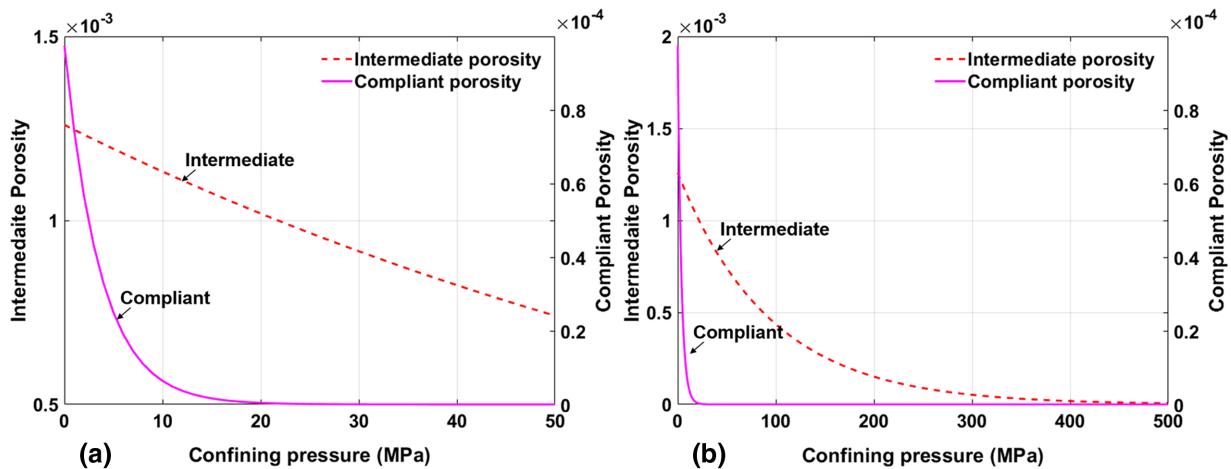


Figure 3 Compliant porosity (red solid line) and intermediate porosity (blue dashed line) in a Bentheim sandstone as a function of confining pressure: (a) up to 50 MPa and (b) above 50 MPa. Note that compliant porosity exhibits an exponential decay with increasing pressure increasing at low pressures. On the other hand, intermediate porosity shows an exponential decay in much broader pressure range, so that the decay at low pressures is almost linear.

less than that of stiff pores, which are defined as intermediate pores.

Such porosity would exhibit an exponential decay with the increasing confining pressure and approach the closure at much higher confining pressures. However, according to the definition of intermediate porosity, the fitting of equations (32) and (33) require the dry rock moduli in much higher pressure limit, which is not available in this work. Thus, we use the CPA method to compute the elastic moduli in much higher pressure limit where both compliant and intermediate pores are closed. Note that the aspect ratio for stiff pores, which can be estimated from the analysis of micro-CT images of the pore structure in the following-up research, is unknown in this work. Therefore, we conduct the computation with three assumed aspect ratios for stiff pores. The dashed lines in Fig. 2(c,d) show the projected pressure-dependent dry moduli of the sandstone in a broader pressure range, as predicted by the model with intermediate porosity involved through equations (32) and (33). The larger the aspect ratio, the larger the dry rock moduli in much higher pressure limit. Correspondingly, the pressure dependency of compliant porosity and intermediate porosity are shown in Fig. 3(a,b) (for intermediate porosity, only aspect ratio of 0.22 is given). Note the linear behaviour of intermediate porosity at pressure below 50–60 MPa. However, at a broader range of confining pressures, intermediate porosity exhibits a significant exponential trend, which is very similar to compliant porosity. Thus, an increase of the range of pressures of ultrasonic experiments can help reduce the range of possible aspect ratios of stiff pores.

DISCUSSION

With the knowledge of required parameters derived for fluid/solid substitution, we first compare the validity and applicability of dual pore structure solid substitution scheme with other methods against the ultrasonic P- and S-wave velocities in Fig. 4(a,b). First of all, the ultrasonically measured elastic moduli of the dry sandstone exhibit strong pressure dependency, which is significantly reduced for the filling of solid octadecane in the rock. Second, we observe that the Gassmann fluid predictions (blue open circles) show a good agreement with the measured liquid-octadecane-saturated bulk modulus (black solid circles), but a little discrepancy for shear modulus. However, the Ciz and Shapiro (2007; C&S) model (black solid triangles) significantly underestimates the solid-octadecane-saturated bulk and shear moduli (black solid triangles), which is consistent with the current understanding of limitations of this theory. Similar to the Gassmann theory, the C&S model also obeys the assumption of the equilibrated stress distribution through the entire pore space and neglects the effects of stiffening due to squirt flow between compliant and stiff pores. Even with these effects taken into account, the dual pore structure scheme by Glubokovskikh *et al.* (2016) model (red stars), give predictions very close to the values given by the lower embedded bound theory (magenta solid line), which defines the smallest change upon solid substitution that occurs in equilibrated pore space. This implies that only compliant and stiff pores might not fully describe the solid squirt effects.

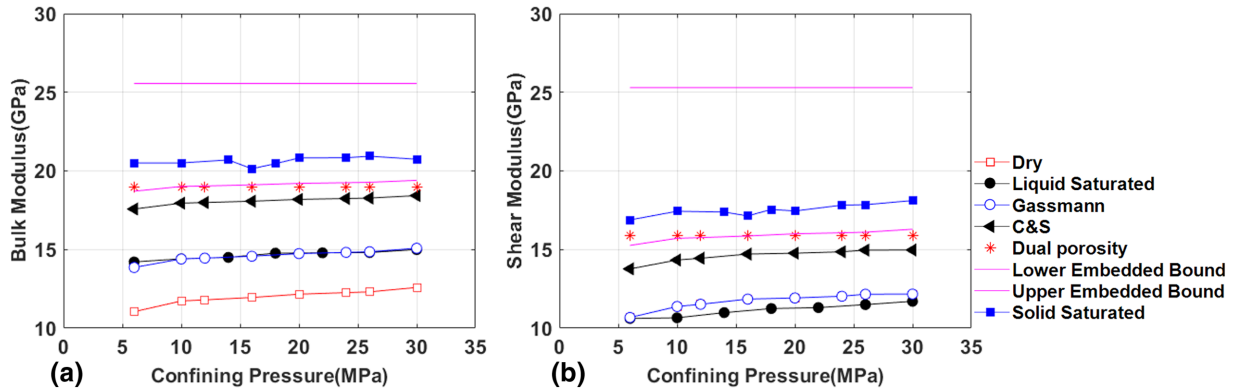


Figure 4 Octadecane-saturated moduli of a Bentheim sandstone predicted by a number of substitution schemes as a function of confining pressure: (a) bulk and (b) shear moduli. Predictions by the Gassmann theory (blue open circles) have a good agreement with the measured liquid-octadecane-saturated (black solid circles) bulk modulus but a slight discrepancy for shear modulus. However, the C&S (black solid triangles) model significantly underestimate the measured bulk and shear moduli of the sandstone saturated with solid octadecane. By comparison, dual porosity model (red stars) gives a closer estimates but still has a clear discrepancy for both bulk and shear moduli. Moreover, this model give predictions close to those given by the lower embedded bound theory (magenta solid line), which defines the smallest change upon solid substitution that occurs in equilibrated pore space.

Figure 5(a,b) provides the predictions of the present triple porosity model (red solid circles, red solid diamonds and red solid squares) against the estimates given by other solid substitution schemes aforementioned. The predictions using an aspect ratio of 1 (red solid squares) for stiff pores largely overestimate the solid-octadecane-saturated rock moduli. This implies that the assumption of De Paula *et al.* (2012) in his paper that only equant pores left when both compliant and intermediate pores are closed is worth exploring. Meanwhile, predictions with an aspect ratio of stiff pores for 0.22 match well with the ultrasonically measured elastic moduli. This aspect

ratio is consistent with values of aspect ratios for sand-related pores in the literature (Xu and White 1995). The agreement indicates that the triple porosity combination might account for the solid squirt effects more precisely. However, it seems very interesting that the bulk modulus of the solid-octadecane-saturated rock has no variation with the increasing of confining pressure, which accords well with the predictions by the present model. Meanwhile, the shear modulus implies a slightly increasing trend, which is not consistent with the present theory. A plausible cause of this difference is the instability of the ultrasonic measurements at relatively small

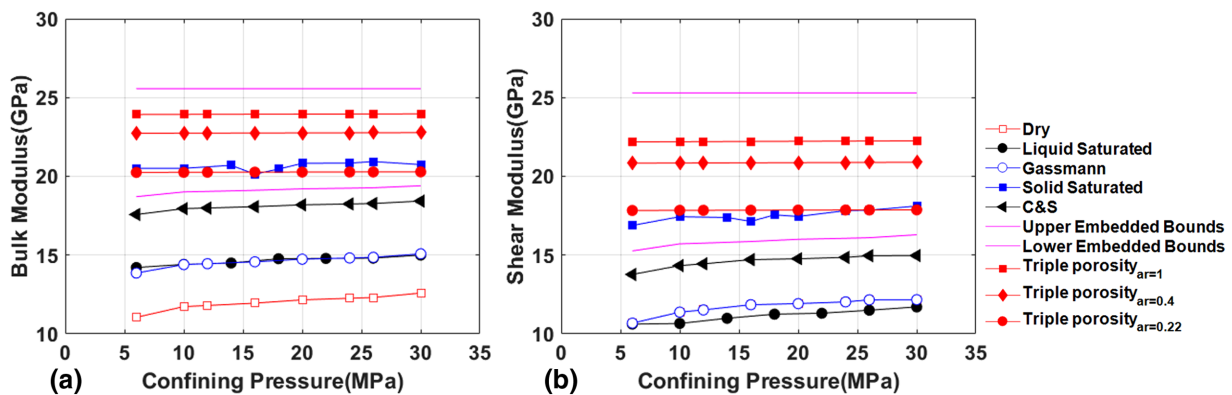


Figure 5 Octadecane-saturated moduli of a Bentheim sandstone predicted by a number of substitution schemes as a function of confining pressure. (a) Bulk and (b) shear moduli. Compared to other substitution schemes, the triple porosity model gives the best fit to ultrasonic measurements of both bulk and shear moduli (blue solid squares) with the assumption of an aspect ratio for stiff pores to 0.22 (red solid circles). Moreover, this model (blue open circles) also has a good agreement with the measured liquid-octadecane-saturated (black solid circles) bulk modulus, but a slight discrepancy for shear modulus.

confining pressures as only few points of data are available. Thus, more data are needed to examine the applicability of the proposed model.

CONCLUSIONS

In this paper, we present a simple solid substitution scheme based on the concept of a triple pore structure in order to better account for the solid squirt effects. We extend the Glubokovskikh *et al.* (2016) model to a more general case containing stiff, compliant and the so-called intermediate pores. Intermediate pores tend to deform to a greater extent than do stiff pores but much less than do compliant pores. At relatively large confining pressures, intermediate pores are approximated as a plane circular interlayer with traction-free edges, which is similar to compliant pores at relatively small confining pressures. Exact equations are derived to estimate the unrelaxed rock frame moduli, which consider the effects of solid substance or viscoelastic materials saturated both in the compliant and intermediate pores. And the lower embedded bound theory is employed to estimate the fully saturated rock moduli for the remaining stiff pores. The equations only require the knowledge of dry rock moduli at given confining pressure. All the required parameters for solid substitution can be extracted from the fitting results of pressure-dependent dry rock moduli. No adjustable parameters are included in the expressions.

Using a sandstone sample saturated with octadecane, we explore the validity and applicability of the proposed model against other solid substitution schemes. Ultrasonically measured dry rock moduli exhibit significant pressure dependency, which is considerably reduced by the filling of solid octadecane in the rock. Predictions by the Gassmann theory accord well with ultrasonic measurements of bulk modulus but a small discrepancy for shear modulus of the sandstone saturated with liquid octadecane. However, the Ciz and Shapiro (2007; C&S) model largely underestimates the elastic moduli of the solid octadecane filled rock. This suggests that stiffening occurs due to substantial reduction of compliance of grain contacts by the solid infill. The C&S model cannot be used to describe the solid squirt effects. Solid substitution based on the binary pore structure performs better than the C&S model. However, predictions of these models are very close to those given by the lower embedded bound theory, which defines the smallest change upon solid substitution in the equilibrated pore space. This implies that only compliant and stiff pores might not fully describe the solid squirt effects. Comparison of the triple porosity model proposed in this paper against

the ultrasonic measurements of the solid-filled rock moduli reveals a reasonable fit for bulk modulus but a little discrepancy for shear modulus at small confining pressures, which is probably due to the instability of the ultrasonic measurements at relatively small confining pressures. Moreover, the scheme also reduces to the Gassmann equation when the pore fill is fluid or inviscid liquid.

ACKNOWLEDGEMENTS

The authors thank the Sponsor of the Curtin Reservoir Geophysics Consortium (CRGC) and the China Scholarship Council (CSC) for the financial support.

CONFLICT OF INTEREST

The authors declare that there is no conflict of interest concerning the publication of this paper.

ORCID

Maxim Lebedev  <http://orcid.org/0000-0003-1369-5844>

REFERENCES

- Berryman J.G. 1980. Long-wavelength propagation in composite elastic media II. Ellipsoidal inclusions. *The Journal of the Acoustical Society of America* **68**, 1820–1831.
- Christensen R. 2005. *Mechanics of Composite Materials*. NY: Dover Publications.
- Ciz R. and Shapiro S.A. 2007. Generalization of Gassmann equations for porous media saturated with a solid material. *Geophysics* **72**, A75–A79.
- Crane R.L. and Knopp J.S. 2009. *Eshbach's Handbook of Engineering Fundamentals*, 5th edn. John Wiley & Sons.
- de Paula O.B., Pervukhina M., Makarynska D. and Gurevich B. 2012. Modeling squirt dispersion and attenuation in fluid-saturated rocks using pressure dependency of dry ultrasonic velocities. *Geophysics* **77**, WA157–WA168.
- Eberhart-Phillips D., Han D.-H. and Zoback M.D. 1989. Empirical relationships among seismic velocity, effective pressure, porosity, and clay content in sandstone. *Geophysics* **54**, 82–89.
- Gassmann F. 1951. Über die Elastizität poröser Medien: Vierteljahrsschrift der Naturforschenden Gesellschaft in Zürich **96**, 1–23.
- Glubokovskikh S., Gurevich B. and Saxena N. 2016. A dual-porosity scheme for fluid/solid substitution. *Geophysical Prospecting* **64**, 1112–1121.
- Gurevich B., Makarynska D., de Paula O.B. and Pervukhina M. 2010. A simple model for squirt-flow dispersion and attenuation in fluid-saturated granular rocks. *Geophysics* **75**, N109–N120.
- Gurevich B., Makarynska D. and Pervukhina M. 2009. Ultrasonic moduli for fluid-saturated rocks: Mavko-Jizba relations rederived and generalized. *Geophysics* **74**, N25–N30.

- Gurevich B. and Saxena N. 2015. A simple recipe for solid substitution at low frequencies and application to heavy oil rocks. Paper presented at the 77th EAGE Conference and Exhibition 2015.
- Hashin Z. and Shtrikman S. 1963. A variational approach to the elastic behavior of multiphase materials. *Journal Mechanics Physical Solids* 11, 127–140.
- Hudson J.A. 1981. Wave speeds and attenuation of elastic waves in material containing cracks. *Geophysical Journal International* 64, 133–150.
- Kuster G.T. and Toksöz M.N. 1974. Velocity and attenuation of seismic waves in two-phase media: Part I. Theoretical formulations. *Geophysics* 39, 587–606.
- Lebedev M., Pervukhina M., Mikhaltsevitch V., Dance T., Bilenko O. and Gurevich B. 2013. An experimental study of acoustic responses on the injection of supercritical CO₂ into sandstones from the Otway Basin. *Geophysics* 78, D293–D306.
- Leurer K.C. and Dvorkin J. 2006. Viscoelasticity of precompact unconsolidated sand with viscous cement. *Geophysics* 71, T31–T40.
- Makarynska D., Gurevich B., Behura J. and Batzle M. 2010. Fluid substitution in rocks saturated with viscoelastic fluids. *Geophysics* 75, E115–E122.
- Mavko G. and Jizba D. 1991. Estimating grain-scale fluid effects on velocity dispersion in rocks. *Geophysics* 56, 1940–1949.
- Mavko G. and Saxena N. 2013. Embedded-bound method for estimating the change in bulk modulus under either fluid or solid substitution. *Geophysics* 78, L87–L99.
- Pervukhina M., Gurevich B., Dewhurst D.N. and Siggins A.F. 2010. Applicability of velocity–stress relationships based on the dual porosity concept to isotropic porous rocks. *Geophysical Journal International* 181, 1473–1479.
- Saenger E.H., Lebedev M., Uribe D., Osorno M., Vialle S., Duda M., Iglauer S. and Steeb H. 2016. Analysis of high-resolution X-ray computed tomography images of Bentheim sandstone under elevated confining pressures. *Geophysical Prospecting* 64, 848–859.
- Saxena N. and Mavko G. 2014. Exact equations for fluid and solid substitution. *Geophysics* 79, L21–L32.
- Saxena N. and Mavko G. 2015. Effects of fluid-shear resistance and squirt flow on velocity dispersion in rocks. *Geophysics* 80, D99–D110.
- Sayers C. and Kachanov M. 1991. A simple technique for finding effective elastic constants of cracked solids for arbitrary crack orientation statistics. *International Journal of Solids and Structures* 27, 671–680.
- Sayers C. and Kachanov M. 1995. Microcrack-induced elastic wave anisotropy of brittle rocks. *Journal of Geophysical Research: Solid Earth* 100, 4149–4156.
- Schoenberg M. and Douma J. 1988. Elastic wave propagation in media with parallel fractures and aligned cracks. *Geophysical Prospecting* 36, 571–590.
- Shapiro S.A. 2003. Elastic piezosensitivity of porous and fractured rocks. *Geophysics* 68, 482–486.
- Tsai H.-C. and Lee C.-C. 1998. Compressive stiffness of elastic layers bonded between rigid plates. *International Journal of Solids and Structures* 35, 3053–3069.
- Vernik L. and Hamman J. 2009. Stress sensitivity of sandstones and 4D applications. *The Leading Edge* 28, 90–93.
- Xu S. and White R.E. 1995. A new velocity model for clay-sand mixtures. *Geophysical Prospecting* 43, 91–118.

2.4 A solid/fluid substitution scheme constrained by pore-scale numerical simulations

A solid/fluid substitution scheme constrained by pore-scale numerical simulations

Yongyang Sun¹,¹ Boris Gurevich,^{1,2} Stanislav Glubokovskikh¹,¹ Maxim Lebedev,¹ Andrew Squelch,¹ Christoph Arns³ and Junxin Guo^{4,5}

¹Department of Exploration Geophysics, Curtin University, GPO Box U1987, Perth, WA 6845, Australia. E-mail: yongyang.sun@postgrad.curtin.edu.au

²CSIRO, 26 Dick Perry Avenue, Kensington, WA 6151, Australia

³University of New South Wales, Sydney, NSW 2052, Australia

⁴Department of Earth and Space Sciences, Southern University of Science and Technology, Shenzhen 518055, China

⁵School of Earth and Space Sciences, University of Science and Technology of China, Hefei 230026, China

Accepted 2019 November 26. Received 2019 November 26; in original form 2019 August 27

SUMMARY

Estimating the effects of pore filling material on the elastic moduli or velocities of porous and fractured rocks attracts widespread attention. This effect can be modelled by a recently proposed triple-porosity scheme, which quantifies this effect from parameters of the pressure dependency of the elastic properties of the dry rock. This scheme divides total porosity into three parts: compliant, intermediate and stiff. Each type of pores is assumed to be spheroidal and characterized by a single aspect ratio. However, the implementation of this model requires the asymptotic values of the elastic moduli at much higher pressures where only non-closable pores remain open. Those pressures are beyond the capacity of most rock physics laboratories and can even crush typical sandstone samples. Experimental data at such pressures are usually unavailable. To address this issue, we introduce pore-scale numerical simulations in conjunction with effective medium theories (EMT) to compute the asymptotic values directly from the microtomographic images. This workflow reduces the uncertainty of model predictions on the geometric information of stiff pores and strengthens the predictive power and usefulness of the model without any adjustable parameters. Applying this to a Bentheim sandstone fully filled with liquid and solid octadecane gives a reasonable match between model predictions and laboratory measurements. This success verifies the accuracy and applicability of the model and indicates its potential in further exploitation and characterization of heavy oil reservoirs and other similar reservoirs.

Key words: Acoustic properties; Seismic attenuation; Microstructure.

1 INTRODUCTION

A link between the elastic moduli of rocks and the properties of pore-filling materials is required for many geophysical applications such as reservoir characterization from seismic data or 4-D seismic monitoring. Establishing such a link requires an understanding of the interactions among the rock matrix, pore space, and solid or liquid pore fill. Pore fill can be gas (e.g. air, hydrocarbon gas, CO₂ and steam), liquid (e.g. brine, oil, magma) or solid (e.g. kerogen, bitumen, salt, ice, gas hydrates, etc.) (Saxena *et al.* 2016). For a fluid pore fill (liquid or gas), the Gassmann (1951) equation gives an exact relationship between the dry and saturated moduli, and has been widely employed to predict the change in saturated elastic moduli upon the change of fluid properties without any detailed geometrics information (Smith *et al.* 2003). The Gassmann theory also stipulates that the effective shear modulus is unaffected by the pore

fluid properties (Berryman 1999). However, the Gassmann theory has an important restriction: it assumes that the pressure in the pore fill is spatially uniform. Thus for rocks filled with solid substances or high-viscosity or non-Newtonian fluids, the Gassmann theory is invalid as the shear compliance of the pore fill impedes the pressure communication between different pores (Makarynska *et al.* 2010; Saxena & Mavko 2014; Glubokovskikh *et al.* 2016; Sun *et al.* 2018).

Ciz & Shapiro (2007, referred to as C&S model) derived an approximate extension of the Gassmann equation to a solid pore fill. However, recent studies (Saxena & Mavko 2014; Glubokovskikh *et al.* 2016; Sun *et al.* 2018) show that the C&S model gives a lower bound to the elastic moduli of porous and fractured rocks saturated with a solid or high-viscosity liquid because it also assumes that stress throughout the pore fill is spatially uniform. This assumption should be accurate if all pores are of approximately the same shape,

but can be violated if the pore space contains pores with a range of shapes and compliances.

Laboratory experiments show that the dry moduli increase with increasing effective pressure (which is defined as the difference between the confining pressure and pore pressure). Several authors have ascribed the significant initial change in elastic moduli with increasing effective pressure to the closure of crack-like compliant pores (Walsh 1965; Zimmerman *et al.* 1986; Shapiro 2003). In particular, Shapiro (2003) developed a model based on a binary pore structure by dividing the total porosity into two parts: stiff or equant porosity, which is the dominant portion of the pore space, and soft or compliant porosity, whose total volume is small, but which controls the pressure dependency of the elastic moduli. Makarynska *et al.* (2010) showed that the presence of compliant pores increases the effect of the solid pore fill on the effective moduli—an effect similar to squirt flow in rocks saturated with a fluid at ultrasonic frequencies (see Leurer & Dvorkin 2006).

The disproportional effect of the compliant pores on the elastic moduli of rocks saturated with a solid is modelled by Saxena & Mavko (2015). However, their approach assumes that the compliant pores are isolated from the stiff pores. Therefore, the stress in the pore fill is not uniform and hence the scheme of Saxena & Mavko (2015) does not reduce to the Gassmann equation for a fluid pore fill. To ensure Gassmann consistency, Glubokovskikh *et al.* (2016) modelled the compliant pores as grain-to-grain contacts open into stiff pores. Compliant pores are modelled as thin circular disks with traction-free edges. The stiffness of the disk is calculated using the solution of the elastic problem by Tsai & Lee (1998). Although this model gives the general trend of the overall elastic moduli resulting from the solid pore fill, the model predictions systematically deviate from experimental data, especially for the shear modulus. This discrepancy is similar to the one observed for liquid-filled rocks at ultrasonic frequencies (de Paula *et al.* 2012) and probably occurred because the binary structure model of the pore space is oversimplified. Indeed some studies show that in addition to compliant and stiff pores there exist pores with intermediate compliance, which are responsible for gradual increase of the dry bulk and shear moduli with pressure of up to hundreds of MPa (Shapiro 2003; Wang *et al.* 2005; Adelinet *et al.* 2010).

Recently, Sun *et al.* (2018) generalized the model of Glubokovskikh *et al.* (2016) to a triple-porosity scheme by adding, similarly to de Paula *et al.* (2012), a newly defined type of pores called intermediate pores. Intermediate pores are defined as having an aspect ratio between that of compliant pores and of the stiff pores. The pressure dependency of the dry moduli is governed by the conjunction of those three pore structures. Two kinds of stress relaxation within the pore space are modelled: (1) between compliant and ‘stiff’ (plus intermediate pores) pores in a relatively low pressure range and (2) between intermediate and stiff pores in a high pressure range. Intermediate porosity decreases in an exponential way at much higher pressures, which behaves similar to the compliant porosity at lower pressures. However, the implementation of this method requires the dry bulk and shear moduli K_{hm} and μ_{hm} in high-pressure limit where rocks are assumed to contain stiff pores only. The pressures corresponding to this limit (200–500 MPa) are beyond the capacity of most rock physics laboratories and can even crush typical sandstone samples (Zhang *et al.* 1990; Wong *et al.* 1997; Fortin *et al.* 2007). Therefore, K_{hm} and μ_{hm} cannot be measured directly. Sun *et al.* (2018) computed K_{hm} and μ_{hm} using an effective medium theory (EMT). This approach requires knowledge of the aspect ratio of stiff pores. Detailed analysis of this issue gives a plausible range of such aspect ratios, and thus the model predicts

a range of the elastic moduli of solid-filled sandstone. Sun *et al.* (2018) applied this approach to a Bentheim sandstone fully saturated with solid octadecane and found that the experimental data lie well within the predicted range. Yet, the prediction uncertainty (associated with lack of knowledge of the effective aspect ratio of stiff pores) reduces the predictive power and usefulness of the theoretical model.

The aim of this paper is to eliminate the uncertainty of model predictions by determining the effective aspect ratio of stiff pores directly from microtomographic images of the pore samples. This is done by numerically simulating K_{hm} and μ_{hm} directly from the 3-D image of a rock fragment using finite element method (FEM) (Roberts & Garboczi 2000; Arns *et al.* 2001, 2002), and inverting these moduli for the aspect ratio using the EMT (assuming that most of the porosity resolved in the image is stiff porosity). An alternative would be to use simulated K_{hm} and μ_{hm} directly in the theoretical model. However, such moduli would likely vary from fragment to fragment due to spatial variation of porosity. Determining the effective aspect ratio of stiff pores is likely to be more robust.

In this work, we first reproduce the theories of the triple-porosity model and modify the workflow by pore-scale numerical simulations based on FEM. We then demonstrate the details of how numerical simulations help constrain the predictions of the triple-porosity model. In the end, we compare the modified model predictions with other solid substitutions schemes against the laboratory measurements.

2 TRIPLE-POROSITY MODEL

In order to account for the pressure dependency of the elastic moduli, Sun *et al.* (2018) proposed a triple-porosity model, in which the pore space is divided into stiff, intermediate and compliant pores. This triple-porosity structure is necessary for adequate characterization of the pore geometry, which in turn is essential for modelling the fluid effects (de Paula *et al.* 2012; Sun *et al.* 2018). Total porosity ϕ is divided into three parts: compliant ϕ_c , intermediate ϕ_m and stiff ϕ_s . The three types of pores are modelled as spheroids, each with a different aspect ratio. The main results that are used to compute the ‘unrelaxed’ frame moduli K_{uf} and μ_{uf} , which correspond to the moduli of a hypothetical rock in which all non-stiff pores (including compliant and intermediate pores in this work) are fully saturated with fluid and stiff pores remain empty, are described by the following equations (Sun *et al.* 2018):

$$\frac{1}{K_{uf}} = \frac{1}{K_{hm}} + \frac{1}{\frac{1}{\frac{1}{K_{dry}} - \frac{1}{K_d}} + \frac{M_{fc}}{\phi_c}} + \frac{1}{\frac{1}{\frac{1}{K_d} - \frac{1}{K_{hm}}} + \frac{M_{fm}}{\phi_m}} \quad (1)$$

and

$$\frac{1}{\mu_{uf}} = \frac{1}{\mu_{hm}} + \frac{4}{15} \left(\frac{1}{K_{uf}} - \frac{1}{K_d} \right) + \frac{1}{\frac{1}{\frac{1}{\mu_{dry}} - \frac{1}{\mu_d}} - \frac{4}{15} \left(\frac{1}{K_{dry}} - \frac{1}{K_d} \right)} + \frac{5}{2} \frac{\mu_f}{\phi_c} + \frac{1}{\frac{1}{\mu_d} - \frac{1}{\mu_{hm}} - \frac{4}{15} \left(\frac{1}{K_d} - \frac{1}{K_{hm}} \right)} + \frac{5}{2} \frac{\mu_f}{\phi_m}, \quad (2)$$

where K_{hm} and μ_{hm} are the high-pressure dry moduli (in this high-pressure limit all pores except stiff pores are assumed completely

closed), K_{dry} and μ_{dry} are the pressure-dependent dry moduli calculated directly from ultrasonic velocities and density, K_d and μ_d correspond to the dry moduli of a hypothetical rock in which compliant pores are closed, ϕ_c and ϕ_m are the pressure-dependent compliant and intermediate porosity, respectively, μ_f is the shear modulus of the pore fill, and M_{fc} and M_{fm} are the modified compression stiffness of a typical fluid- or solid-saturated compliant and intermediate pore respectively as given by Tsai & Lee (1998).

Once K_{uf} and μ_{uf} are obtained, we can compute the undrained moduli by saturating the remaining stiff porosity using the lower embedded bound theory (Mavko & Saxena 2013; Saxena & Mavko 2014; Glubokovskikh *et al.* 2016). We do not reproduce the derivation details but outline the workflow to obtain all the parameters (K_{hm} , μ_{hm} , ϕ_c , ϕ_m , K_d , μ_d , M_{fc} and M_{fm}) in equations (1) and (2) (an extension of the workflow described by Sun *et al.* (2018).

(1) Dry moduli K_{dry} and μ_{dry} are computed from the pressure dependency of ultrasonic P - and S -wave velocities and the measured density.

(2) Parameters of compliant pores (ϕ_{c0} , θ_c , α_c) are obtained directly from the deformation equations (3) and (4) based on the dual-porosity model by Shapiro (2003) through the least square fitting of the pressure dependency of the dry moduli calculated in step (1).

$$K_{dry} = K_{hc} \left[1 + \theta_s \left(\frac{1}{K_{hc}} - \frac{1}{K_g} \right) P - \theta_c \phi_{c0} e^{-\frac{\theta_c P}{K_{hc}}} \right] \quad (3)$$

and

$$\mu_{dry} = \mu_{hc} \left[1 + \theta_{s\mu} \left(\frac{1}{\mu_{hc}} - \frac{1}{\mu_g} \right) P - \theta_{c\mu} \phi_{c0} e^{-\frac{\theta_{c\mu} P}{\mu_{hc}}} \right], \quad (4)$$

where K_{hc} and μ_{hc} represent the dry moduli of a hypothetical rock in which compliant pores are closed and the porosity of stiff pores equal to zero-pressure value, ϕ_{c0} is the initial compliant porosity at zero pressure, K_g and μ_g are the bulk and shear moduli of the mineral matrix, θ_c and $\theta_{c\mu}$ are the bulk and shear stress sensitivity coefficients of compliant pores, and θ_s and $\theta_{s\mu}$ are the bulk and shear stress sensitivity coefficients of stiff pores.

(3) Similarly to compliant pores, parameters of intermediate pores (K_{hm} , μ_{hm} , ϕ_{m0} , θ_m , $\theta_{\mu m}$) could be derived directly from the deformation equations

$$K_d = K_{hm} \left[1 - \theta_m \phi_{m0} e^{-\frac{\theta_m P}{K_{hm}}} \right] \quad (5)$$

and

$$\mu_d = \mu_{hm} \left[1 - \theta_{\mu m} \phi_{m0} e^{-\frac{\theta_{\mu m} P}{\mu_{hm}}} \right], \quad (6)$$

where θ_m and $\theta_{\mu m}$ are the bulk and shear stress sensitivity coefficients of intermediate pores. ϕ_{m0} is the initial intermediate porosity at zero pressure. For large pressures where compliant pores are closed, $K_d = K_{dry}$ and $\mu_d = \mu_{dry}$. K_d can be obtained from the sum of K_{dry} and the exponential term $K_{hc} \theta_c \phi_{c0} e^{-\frac{\theta_c P}{K_{hc}}}$, and μ_d can be obtained in the same way. If the pressure dependencies of the dry moduli are available at relatively high pressures (50–500 MPa), the parameters (K_{hm} , μ_{hm} , ϕ_{m0} , θ_m , $\theta_{\mu m}$) can be obtained by the least-square fitting directly. However, ultrasonic velocities at these pressures are seldom available. Thus, we choose to compute the elastic moduli K_{hm} and μ_{hm} by pore-scale numerical simulations using finite element method. At the voxel size of 2–5 μm these images do not contain compliant or even intermediate pores, and thus the simulated dry moduli can be expected to correspond to the moduli of the rock containing only stiff pores (so called ‘Swiss Cheese’

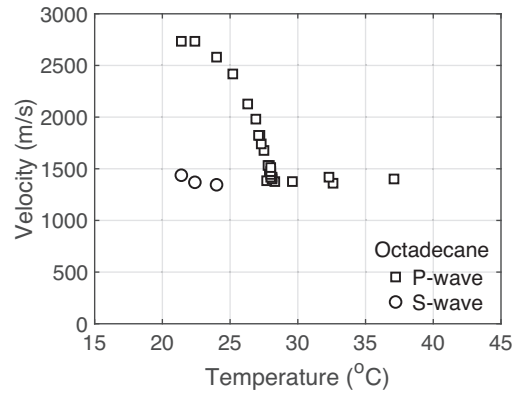


Figure 1. Ultrasonic P - (open squares) and S -wave (open circles) velocities of octadecane as a function of temperature.

rock, see Shapiro 2003). This assumption is consistent with the results of Saenger *et al.* (2016), who simulated elastic properties from digital images obtained under different confining pressures and found that simulated P - and S -wave velocities are not sensitive to the confining pressure. Then, other parameters (ϕ_{m0} , θ_m , $\theta_{\mu m}$) of intermediate pores can be obtained from K_{hm} and μ_{hm} , as well as from the slope of the linear decay of the intermediate porosity versus pressure at relatively small effective pressures. This slope is in turn obtained from the first-order Taylor expansion (7) and (8) of deformation equations (5) and (6)

$$K_d = K_{hm} (1 - \theta_m \phi_{m0}) + \theta_m^2 \phi_{m0} P \quad (7)$$

and

$$\mu_d = \mu_{hm} \left(1 - \theta_{\mu m} \phi_{m0} + \frac{\theta_{\mu m} \theta_m \phi_{m0}}{K_{hm}} \right). \quad (8)$$

(4) Pore-scale numerical simulations can only be performed on a pore-scale image of a mm-size rock fragment. Since porosity can be spatially varying, the simulation results depend on the choice of the fragment, which in turn creates an uncertainty in K_{hm} and μ_{hm} . To deal with this issue, we choose to invert the effective aspect ratio of stiff pores using the EMT based on the numerical simulation. We then substitute the obtained aspect ratio and measured total porosity of the entire sample into the same EMT to calculate K_{hm} and μ_{hm} .

(5) With all the parameters obtained from previous steps, we then calculate the unrelaxed rock frame moduli using equations (1) and (2).

(6) Finally, we compute the fully saturated moduli through the lower embedded bound theory by saturating the remaining open stiff pores with a fluid or a true solid.

Previous workflow presents the procedure of using the triple-porosity scheme to estimate the effective moduli of porous rocks saturated with fluids or true solids. Within the workflow, pore-scale numerical simulations are key in deriving the parameters of intermediate pores and are described in next section.

3 APPLICATION

3.1 Experimental data of a Bentheim sandstone

In order to illustrate the validity and applicability of the modified model constrained by pore-scale numerical simulation presented in previous sections, we apply the model to the data of Sun *et al.* (2018). This ultrasonic data is measured on a Bentheim sandstone,

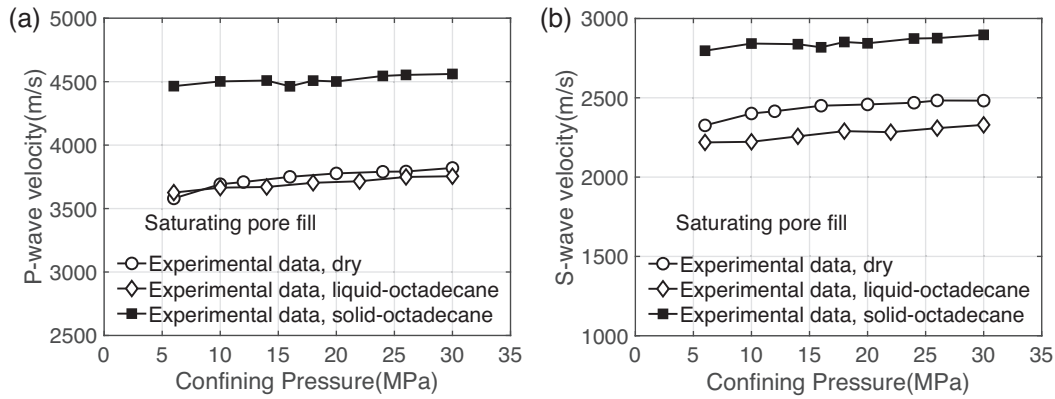


Figure 2. Ultrasonic P wave (a) and S wave (b) of the dry (open circles), liquid- (open squares) and solid-octadecane-saturated (solid squares) Bentheim sandstone as a function of confining pressures.

Table 1. Material properties for the mineral (Vernik 1998) and pore fills used for the modeling and simulations. K_g and μ_g is the bulk and shear moduli of matrix.

K_g	μ_g	K_f (solid)	μ_f (solid)	K_f (fluid)	ϕ
37.3 GPa	38.2 GPa	3.87 GPa	1.46 GPa	1.53 GPa	23.56 per cent

which has a porosity of 23.56 per cent and is very homogeneous, predominantly comprised of 97 per cent quartz with small portion of accessory feldspars, heavy minerals and Fe-(hydr) oxides (Dubelaar & Nijland 2015). As shown in Fig. 1, the pore fill, octadecane, was chosen because it has a melting/freezing point of $T_m = 28$ °C, making it easy to perform laboratory experiments with this substance in both liquid and solid states.

Figs 2(a) and (b) demonstrate the laboratory measurements of ultrasonic P - and S -wave velocities of the sample in a dry state (open circles) and liquid- (open diamonds) and solid-octadecane (solid squares) saturated in the pressure range of 6–30 MPa. In the dry state, both P - and S -wave velocities increase clearly with the increasing confining pressure. However, under the condition of solid-octadecane saturated, the pressure dependency of velocities is reduced. To model this difference, we will need the physical properties of the dry sample and octadecane in liquid and solid forms. These properties are summarized in Table 1.

Note that the ultrasonic measurements on dry sample yield the dry bulk and shear moduli of the rock as the dry velocities are not dispersive (Adelinet *et al.* 2010; Adam & Otheim 2013). Hence, the dry moduli can be obtained directly from those dry velocities and measured density. In the following sections, we will present analysis of velocities and moduli as functions of confining pressure rather than effective pressure, because it is impossible to independently control pore pressure in the solid pore fill.

3.2 Numerical simulations

3.2.1 Image acquisition

Digital rock images used in this study are acquired by 3-D X-ray microscope VeraXRM-500 (ZRadia-Zeiss) at X-ray energy of 60 kV at the voxel size of $2 \mu\text{m}$ on the same Bentheim sandstone. For simulation purposes, image segmentation—which is the procedure of attributing different ranges of grey levels to various phases—controls the accuracy of pore-scale numerical simulations. The first step in this procedure is using a 3-D non-local filter to suppress the

noise effects. The threshold image segmentation is achieved using combination of Avizo 9.3 software (mainly image processing) and the ImageJ/Fiji software with the 3-D ImageJ Suite plugin (analysis, Ollion *et al.* 2013). The maximum size of the original data set obtained from the cylindrical core samples is $510 \times 550 \times 893$ voxels. As shown in Figs 3(a)–(d), several subsets of different sizes, are extracted for numerical simulations. All these subsets have the same voxel size of $2 \mu\text{m}$ and are segmented to two-phase images: mineral matrix and pore space.

3.2.2 Property prediction

Microstructures defined by the extracted digital images have been already discretized and ready for the numerical computation of elastic moduli. We calculate the elastic moduli of the mixture system with FEM (Roberts & Garboczi 2000; Arns *et al.* 2001, 2002). The digital image is assumed to have periodic boundary conditions. Elastic moduli of the matrix are set to $K_g = 37.3$ GPa and $\mu_g = 38.3$ GPa, given by Vernik (1998) (average values of the elastic moduli of clean arenites and arenites). Elastic moduli of the pore fill K_f and μ_f are set to zero in order to simulate the dry moduli. Numerical simulation results based on the four different discretized images (Figs 3a–d) are presented in Table 2.

Table 2 shows that all the simulations overestimate the dry elastic moduli compared with the experimental data at pressure $P_e = 6$ MPa. This is consistent with the previous assumption that numerical simulations from microtomographic X-ray images only corresponds to the effects of stiff pores. We assume that the ‘best’ simulation results are identical to the high-pressure limit moduli K_{hm} and μ_{hm} . This cannot be established directly. Indeed, not only laboratory equipment is mostly limited to $P < 50$ – 100 MPa, but even if we could measure rocks at pressures of 200–2000 MPa, these pressures would likely be outside the elastic regime. However, as suggested by a number of authors (Arns *et al.* 2007; Andrä *et al.* 2013; Saenger *et al.* 2016), we can infer this information indirectly. A typical X-ray microtomographic has a linear size of 1000 voxels and is about 10–50 average linear sand grain sizes. Thus, a typical grain has a length of about 20–100 voxels. The thinnest grain contacts that can be confidently resolved have a thickness of 5 voxels (at least!). Hence the smallest aspect ratio that can be resolved is $a = 0.05$ – 0.25 (or larger if we need more. These contacts will close at pressures $P = aK$, where K is bulk modulus of the rock matrix. For the Bentheim sandstone, $K \sim 10$ GPa; this gives P on the order of 500–2500 MPa. However, the simulations presented in Table 2 show that numerical simulations depend on the choice of

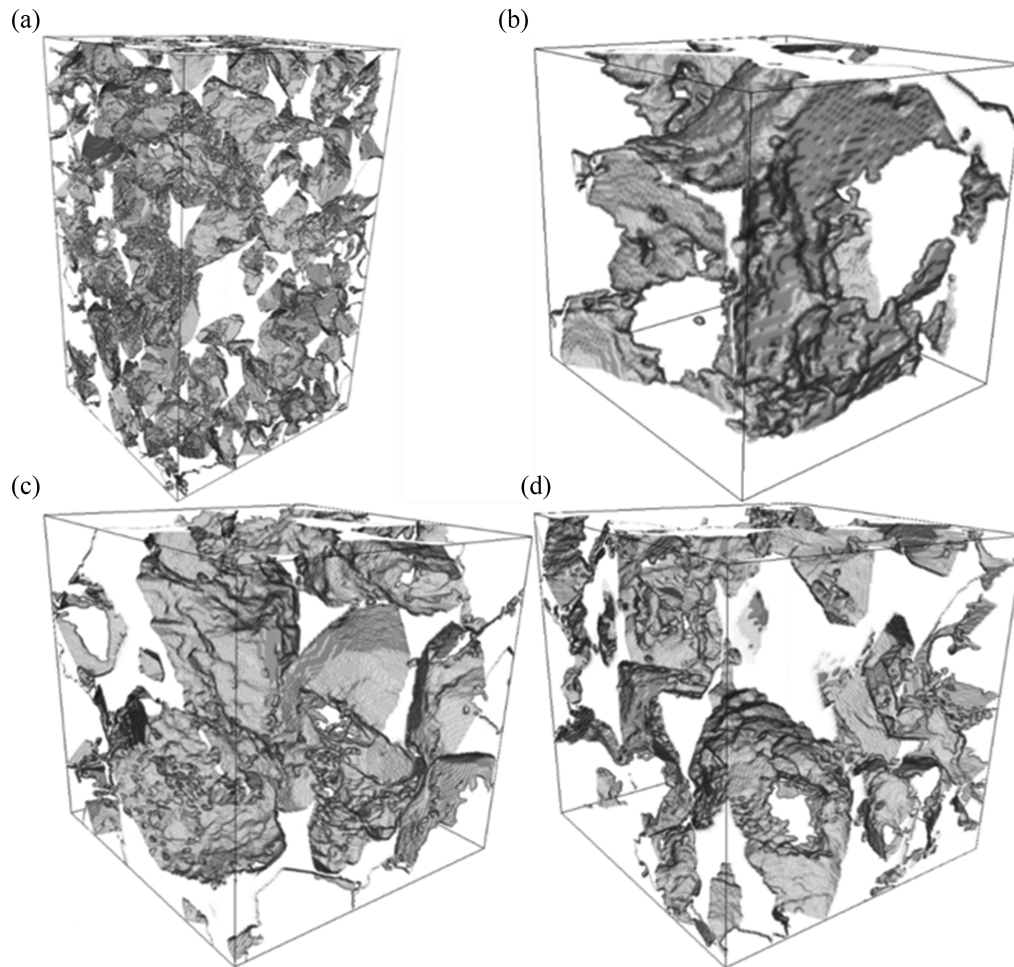


Figure 3. Pore space images of different sizes (a) $510 \times 550 \times 893$, (b) $128 \times 128 \times 128$, (c) $256 \times 256 \times 256$, and (d) $256 \times 256 \times 256$ of subsets extracted from the original cylinder core plugs with the same voxel size of $2 \mu\text{m}$. Images (c) and (d) are the subsets of the same size extracted from different place in the original data set.

Table 2. Simulated dry moduli using different fragments of the digital images.

	K_{dry} (GPa)	μ_{dry} (GPa)	ϕ
$128 \times 128 \times 128$	19.06	18.49	18.65 per cent
$256 \times 256 \times 256$ (upper)	15.98	14.17	21.73 per cent
$256 \times 256 \times 256$ (lower)	13.76	13.20	25.84 per cent
$510 \times 550 \times 893$	17.06	16.29	21.34 per cent
$P_e = 6 \text{ MPa}$	11.67	9.59	

the fragment, which in turn creates an uncertainty in K_{hm} and μ_{hm} . To address this issue, we use the simulation results in conjunction with EMT to determine the effective aspect ratio of stiff pores and then substitute the aspect ratio into the same EMT to compute K_{hm} and μ_{hm} .

3.2.3 Computation of the aspect ratio of stiff pores

In order to compute the aspect ratio of stiff pores, in Figs 4(a) and (b), we compare the numerical simulation results (open circles) against the predictions given by the Self-Consistent Approximation

(SCA, Berryman 1980; Ogushwitz 1985) method, assuming the pore geometry of spheres (red dashed line), needles (blue dotted line), and spheroids with an aspect ratio of 0.5 (dashed line), 0.23 (solid line) and 0.1 (dotted line). We note that the predictions given by setting the aspect ratio of stiff pores to 0.23 provide a satisfactory fit to our numerical simulation results. Then, in Figs 5(a) and (b), we compare the numerical simulation results against the predictions given by different EMT methods: the SCA, Kuster-Toksoz (referred to as KT) model (Kuster & Toksöz 1974) and differential effective medium theory (referred to as DEM, Cleary *et al.* 1980; Norris 1985; Zimmerman 1991) using the same aspect ratio of 0.23 for stiff pores. The SCA method gives the predictions closest to our numerical predictions. This suggests that the SCA method is the best option to compute the effective aspect ratio of stiff pores.

We then compute the high-pressure limit moduli $K_{hm} = 14.74 \text{ GPa}$ and $\mu_{hm} = 14.20 \text{ GPa}$ by substituting the aspect ratio of stiff pores $\alpha_s = 0.23$ into the SCA method. Then, following the eqs (7) and (8) in the previous section, we obtain the parameters of intermediate pores (θ_m , $\theta_{\mu m}$, ϕ_{m0}). To this end, as shown in Table 3, all the parameters required in the eqs (1) and (2) are obtained from the pressure dependency of ultrasonic velocities and density. We then compare the model predictions against the experimental data in next section.

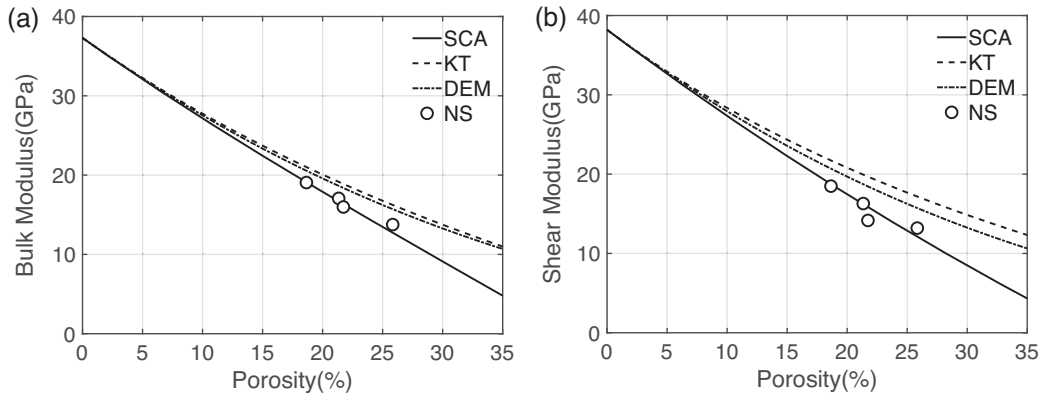


Figure 4. Comparison of the pore-scale numerical simulations to the predictions for the dry bulk (a) and shear (b) moduli using the SCA method assuming different pore shapes.

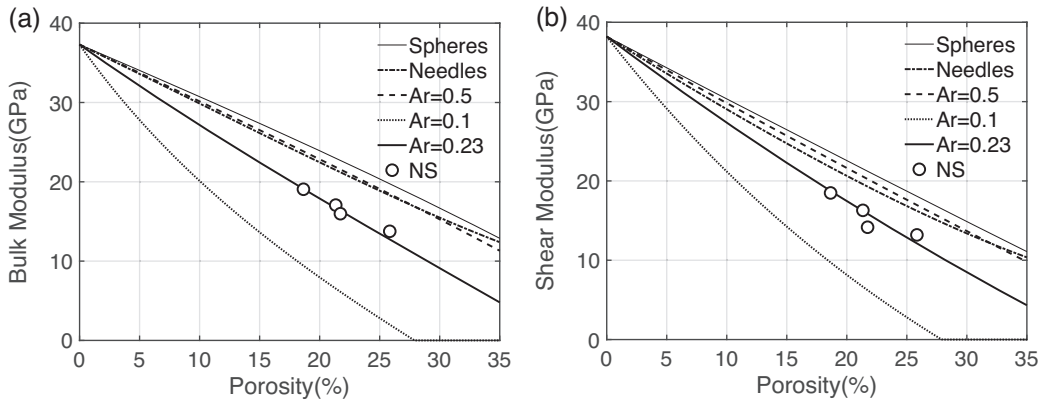


Figure 5. Comparison of the pore-scale numerical simulations to a range of theories used to predict the dry bulk (a) and shear (b) moduli using the same aspect ratio of 0.23 for stiff pores.

Table 3. The parameters of compliant and intermediate porosity of the Bentheimer sandstone obtained by applying the workflow of Section 3 to ultrasonic measurements in a dry state.

θ_c	α_c	θ_m	α_m	ϕ_{c0}	ϕ_{m0}
3.16×10^3	1.78×10^{-4}	1.37×10^2	4.2×10^{-3}	9.75×10^{-4}	1.6×10^{-3}

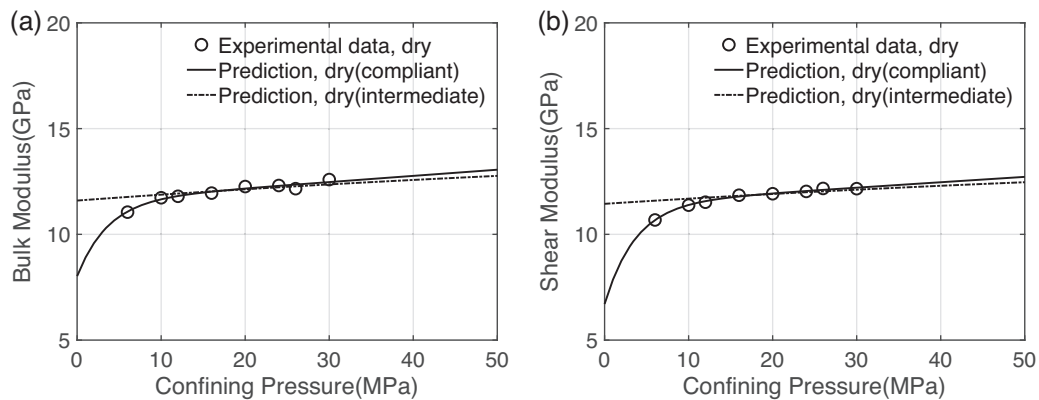


Figure 6. Dry bulk (a) and shear (b) moduli of a Bentheimer sandstone as a function of pressure up to 50 MPa. The bulk and shear moduli calculated from the ultrasonic velocities are shown by open circles. Variations of the elastic moduli modelled for low pressures and caused by the closure of the compliant and intermediate pores are shown by the solid line and dashed-dotted line, respectively.

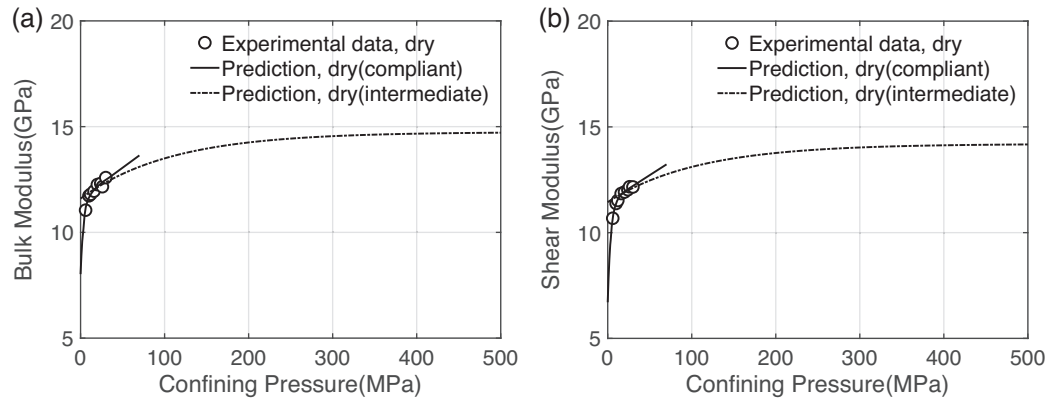


Figure 7. Dry bulk (a) and shear (b) moduli of a Bentheim sandstone as a function of pressure up to 500 MPa. The bulk and shear moduli calculated from the ultrasonic velocities are shown by open circles. Variations of the elastic moduli modelled for low pressures and caused by the closure of the compliant and intermediate pores are shown by the solid line and dashed–dotted line, respectively.

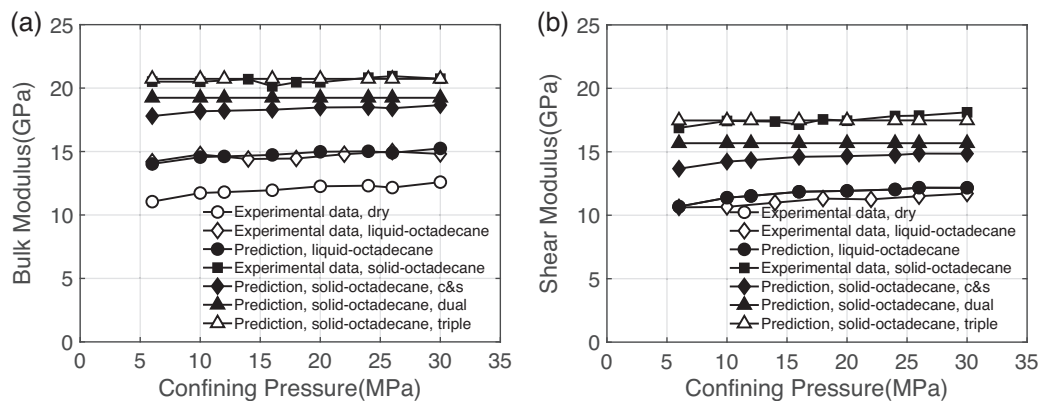


Figure 8. Comparison of the experimental bulk (a) and shear (b) moduli of a Bentheim sandstone saturated with liquid- and solid-octadecane against predictions of different models as a function of confining pressure. Open circles, diamonds and solid squares are the dry, liquid- and solid-octadecane-saturated moduli calculated from the ultrasonic velocities and density respectively. Open triangles are the predictions of the triple-porosity scheme constrained by pore-scale numerical simulations. Solid diamonds and triangles are the predictions of the C&S and dual-porosity models.

Alternatively, aspect ratio could be estimated by inverting the moduli of each fragment (Arns *et al.* 2003; Liu *et al.* 2018). Given that the moduli for all fragments closely follow the single aspect ratio trend (Figs 4 and 5), this approach should give similar results.

3.3 Results

Figs 6(a) and (b) show the least square fitting of the theoretical pressure dependency of the dry moduli (solid line) to the measurements (open circles) for pressures up to 50 MPa. We observe that a combination of exponential and linear terms accounts well for the increase of the dry moduli with the increasing effective pressure. Note that the exponential trend attributed to the compliant cracks closure vanishes within 10–20 MPa. On the other hand, the linear term (dashed–dotted line) is ascribed to the gradual closure of stiff pores (including intermediate pores). However, at pressures up to 500 MPa [see Figs 7(a) and (b), a zoom-in plot of Figs 6(a) and (b)], the dry moduli also show an exponential increase resulting from the closure of intermediate pores, similar to the behaviour of compliant pores at low pressures (<20 MPa). This behaviour at higher pressures has been documented by the ultrasonic measurements of several eclogites and country rocks under confining pressure up to 800 MPa by Wang *et al.* (2005), which exhibit an approximately

exponential increase of the dry moduli with the increasing confining pressures.

We then substitute the parameters from Table 3 into our model and give the model predictions, as shown in Figs 8(a) and (b). First, we see that the C&S model (solid diamonds) gives much lower prediction of the solid-octadecane-saturated moduli in comparison with the experimental data (solid squares). The dual-porosity model (solid triangles) performs much better, but still has a clear discrepancy compared against the experimental data. Compared with the C&S model and the dual-porosity model, the present model (open triangles) gives more accurate estimates, which agree well with the laboratory measurements of the elastic moduli of the sandstone saturated with solid octadecane. Moreover, in the case of liquid octadecane in the pore space (open diamonds), the present model (solid circles) gives predictions that are consistent with the Gassmann theory.

4 DISCUSSION

One important feature of our scheme is that we assume the rock contains three types of pores, compliant, intermediate and stiff. Each type of pores is described to be spheroidal and has an aspect ratio. While this is a crude simplification in regard to the realistic pore shapes, such treatment seems to provide a good fit to the pressure

dependency of the dry moduli. In this sense, this approximation is reasonable and effective.

Different from the recognition of a binary pore structure, we add a newly defined pore type, intermediate, to explain the pressure effects on the dry moduli at much higher pressures. As defined, intermediate porosity decreases in an exponential law at intermediate pressures, say 200–1000 MPa. We do not claim that this behavior of the pores at such high pressures is realistic. Indeed, those pressures are beyond the capacity of most rock physics laboratories and can even crush typical sandstone samples (Zhang *et al.* 1990; Wong *et al.* 1997; Fortin *et al.* 2007), though not mantle rocks (Wang *et al.* 2005). Sandstones at such pressures probably lie outside of the elastic regime. Yet the assumption of the behavior of velocities at such pressures is helpful for understanding of pore space geometry.

Application of our model requires the asymptotic values of the dry moduli in high-pressure limit that are usually unknown or hard to obtain directly from ultrasonic measurements due to the restriction of narrow measurement range of pressures. This work introduced pore-scale numerical simulations based on FEM in conjunction with the SCA to determine the effective aspect ratio of stiff pores and then compute the values by substituting the aspect ratio into the SCA. Such treatment implies that the numerical simulation results only correspond to the effects of stiff pores, while soft (compliant and intermediate) pores in the digital rock images are not resolved. While this assumption is reasonable for digital rock images with the voxel size of about 2–5 μm , the smallest voxel size currently available, future developments might provide more direct ways to characterize the pore shapes.

Another potential limitation of our approach is that the model is only suitable for pure sandstone. For shaley sandstone or other complex composite rocks, the pressure effects on the dry moduli are more complicated, and not only controlled by the closure of cracks. Moreover, the pore shapes information extracted from digital rock images is different from those of pure sandstone. Such influence might be studied in future work.

5 CONCLUSIONS

We present a simple scheme for fluid or solid substitution constrained by pore-scale numerical simulation based on finite element method. This scheme relates the change of the effective elastic moduli of porous and fractured rocks to the moduli of pore fill, including fluids, high-viscosity fluids and elastic solids. Pore-scale numerical simulations based on FEM are used to successfully determine the aspect ratio of stiff pores directly from microtomographic images in conjunction with the self-consistent medium theory. Then, the asymptotic values of dry moduli in high-pressure limit where only non-closable pores remain open are obtained using the SCA and then substituted into the scheme to estimate the effective elastic moduli of porous and fractured rocks saturated with various pore fills. The workflow avoids the need to assume the specific geometry of stiff pores and reduces the uncertainty of model predictions without any adjustable parameters. This strengthens the predictive power and usefulness of the model in predicting the effective elastic moduli of rocks resulting from the change in the moduli of pore fill. Successful application to a liquid- and solid-octadecane-saturated Bentheim sandstone has verified the accuracy and applicability of this scheme and indicated its potential in further exploitation and characterization of heavy oil and similar reservoirs.

ACKNOWLEDGEMENTS

We thank the financial support from the Curtin Reservoir Geophysics Consortium (CRGC) and the China Scholarship Council (CSC). This work was accomplished with the assistance of the Computational Infrastructure (NCI), which is supported by the Australian Government and the Pawsey Supercomputing Centre with funding from the Australian Government and the Government of Western Australia.

REFERENCES

- Adam, L. & Otheim, T., 2013. Elastic laboratory measurements and modeling of saturated basalts, *J. geophys. Res.*, **118**, 840–851.
- Adelinet, M., Fortin, J., Guéguen, Y., Schubnel, A. & Geoffroy, L., 2010. Frequency and fluid effects on elastic properties of basalt: experimental investigations, *Geophys. Res. Lett.*, **37**, doi:10.1029/2009GL041660.
- Andrä, H. *et al.*, 2013. Digital rock physics benchmarks—Part II: computing effective properties, *Comput. Geosci.*, **50**, 33–43.
- Arns, C.H., Knackstedt, M.A. & Mecke, K., 2003. Reconstructing complex materials via effective grain shapes, *Phys. Rev. Lett.*, **91**, 215506.
- Arns, C.H., Knackstedt, M.A., Pinczewski, M.V. & Lindquist, W., 2001. Accurate estimation of transport properties from microtomographic images, *Geophys. Res. Lett.*, **28**, 3361–3364.
- Arns, C.H., Knackstedt, M.A., Pinczewski, W.V. & Garboczi, E.J., 2002. Computation of linear elastic properties from microtomographic images: methodology and agreement between theory and experiment, *Geophysics*, **67**, 1396–1405.
- Arns, C.H., Madadi, M., Sheppard, A.P. & Knackstedt, M.A., 2007. Linear elastic properties of granular rocks derived from X-ray-CT images, in *SEG Technical Program Expanded Abstracts 2007*, pp. 1711–1715, Society of Exploration Geophysicists.
- Berryman, J.G., 1980. Long-wavelength propagation in composite elastic media II. Ellipsoidal inclusions, *J. acoust. Soc. Am.*, **68**, 1820–1831.
- Berryman, J.G., 1999. Origin of Gassmann's equations, *Geophysics*, **64**, 1627–1629.
- Ciz, R. & Shapiro, S.A., 2007. Generalization of Gassmann equations for porous media saturated with a solid material, *Geophysics*, **72**, A75–A79.
- Cleary, M.P., Lee, S.-M. & Chen, I.-W., 1980. Self-consistent techniques for heterogeneous media, *J. Eng. Mech. Div.*, **106**, 861–887.
- de Paula, O.B., Pervukhina, M., Makarynska, D. & Gurevich, B., 2012. Modeling squirt dispersion and attenuation in fluid-saturated rocks using pressure dependency of dry ultrasonic velocities, *Geophysics*, **77**, WA157–WA168.
- Dubelaar, C.W. & Nijland, T.G., 2015. The Bentheim Sandstone: geology, petrophysics, varieties and its use as dimension stone, in *Engineering Geology for Society and Territory*, Vol. 8, pp. 557–563, Springer.
- Fortin, J., Guéguen, Y. & Schubnel, A., 2007. Effects of pore collapse and grain crushing on ultrasonic velocities and V_p/V_s , *J. geophys. Res.*, **112**, doi:10.1029/2005JB004005.
- Gassmann, F., 1951. Über die Elastizität poröser Medien: Vierteljahrsschrift der Naturforschenden Gesellschaft in Zürich, **96**, 1–23.
- Glubokovskikh, S., Gurevich, B. & Saxena, N., 2016. A dual-porosity scheme for fluid/solid substitution, *Geophys. Prospect.*, **64**, 1112–1121.
- Kuster, G.T. & Toksöz, M.N., 1974. Velocity and attenuation of seismic waves in two-phase media: Part I. Theoretical formulations, *Geophysics*, **39**, 587–606.
- Leurer, K.C. & Dvorkin, J., 2006. Viscoelasticity of precompact unconsolidated sand with viscous cement, *Geophysics*, **71**, T31–T40.
- Liu, X., Yin, X. & Luan, X., 2018. Seismic rock physical modelling for gas hydrate-bearing sediments, *Sci. China Earth Sci.*, **61**, 1261–1278.
- Makarynska, D., Gurevich, B., Behura, J. & Batzle, M., 2010. Fluid substitution in rocks saturated with viscoelastic fluids, *Geophysics*, **75**, E115–E122.
- Mavko, G. & Saxena, N., 2013. Embedded-bound method for estimating the change in bulk modulus under either fluid or solid substitution, *Geophysics*, doi:10.1190/geo2013-0074.1.

- Norris, A., 1985. A differential scheme for the effective moduli of composites, *Mech. Mater.*, **4**, 1–16.
- Ogushwitz, P., 1985. Applicability of the Biot theory. I. Low-porosity materials, *J. acoust. Soc. Am.*, **77**, 429–440.
- Ollion, J., Cochenec, J., Loll, F., Escudé, C. & Boudier, T., 2013. TANGO: a generic tool for high-throughput 3D image analysis for studying nuclear organization, *Bioinformatics*, **29**, 1840–1841.
- Roberts, A.P. & Garboczi, E.J., 2000. Elastic properties of model porous ceramics, *J. Am. Ceram. Soc.*, **83**, 3041–3048.
- Saenger, E.H., Lebedev, M., Uribe, D., Osorno, M., Vialle, S., Duda, M., Iglauer, S. & Steeb, H., 2016. Analysis of high-resolution X-ray computed tomography images of Bentheim sandstone under elevated confining pressures, *Geophys. Prospect.*, **64**, 848–859.
- Saxena, N. & Mavko, G., 2014. Exact equations for fluid and solid substitution, *Geophysics*, **79** (3), doi:10.1190/geo2013-0187.1.
- Saxena, N. & Mavko, G., 2015. Effects of fluid-shear resistance and squirt flow on velocity dispersion in rocks, *Geophysics*, **80**(2), doi:10.1190/geo2014-0304.1.
- Saxena, N., Mavko, G., Hofmann, R., Gurevich, B., Glubokovskikh, S., Aliyeva, S. & Dutta, P., 2016. Rock-physics models for heavy-oil and organic-solid substitution, *Leading Edge*, **35**, 506–510.
- Shapiro, S.A., 2003. Elastic piezosensitivity of porous and fractured rocks, *Geophysics*, **68**, 482–486.
- Smith, T.M., Sondergeld, C.H. & Rai, C.S., 2003. Gassmann fluid substitutions: a tutorial, *Geophysics*, **68**, 430–440.
- Sun, Y., Gurevich, B., Lebedev, M., Glubokovskikh, S., Mikhaltsevitch, V. & Guo, J., 2018. A triple porosity scheme for fluid/solid substitution: theory and experiment, *Geophys. Prospect.*, 1–12.
- Tsai, H.-C. & Lee, C.-C., 1998. Compressive stiffness of elastic layers bonded between rigid plates, *Int. J. Solids Struct.*, **35**, 3053–3069.
- Vernik, L., 1998. Acoustic velocity and porosity systematics in siliciclastics, *Log Analyst*, **39** (4), 27–35.
- Walsh, J., 1965. The effect of cracks on the compressibility of rock, *J. geophys. Res.*, **70**, 381–389.
- Wang, Q., Ji, S., Salisbury, M.H., Xia, B., Pan, M. & Xu, Z., 2005. Pressure dependence and anisotropy of P-wave velocities in ultrahigh-pressure metamorphic rocks from the Dabie–Sulu orogenic belt (China): implications for seismic properties of subducted slabs and origin of mantle reflections, *Tectonophysics*, **398**, 67–99.
- Wong, T., David, C. & Zhu, W., 1997. The transition from brittle faulting to cataclastic flow in porous sandstones: mechanical deformation, *J. geophys. Res.*, **102**, 3009–3025.
- Zhang, J., Wong, T.F. & Davis, D.M., 1990. Micromechanics of pressure-induced grain crushing in porous rocks, *J. geophys. Res.*, **95**, 341–352.
- Zimmerman, R.W., 1991. *Compressibility of Sandstones*, Vol. **29**, Elsevier.
- Zimmerman, R.W., Somerton, W.H. & King, M.S., 1986. Compressibility of porous rocks, *J. geophys. Res.*, **91**, 12 765–12 777.

2.5 Modeling elastic properties of Vycor glass saturated with liquid and solid adsorbate



Modeling elastic properties of Vycor glass saturated with liquid and solid adsorbates

Yongyang Sun¹ · Boris Gurevich^{1,2} · Gennady Y. Gor³

Received: 26 January 2019 / Revised: 14 April 2019 / Accepted: 24 April 2019 / Published online: 31 May 2019
© Springer Science+Business Media, LLC, part of Springer Nature 2019

Abstract

A combination of ultrasonic experiments with gas adsorption is a promising tool for improved characterization of nanoporous materials. The use of ultrasound requires understanding of the effects of adsorbates on the elastic properties of nanoporous medium. This issue is not trivial, because nanostructured materials, as well as nanoconfined matter, may exhibit physical properties that differ substantially from the properties of “normal” bulk materials. In this paper, we investigate the change of elastic properties of Vycor glass filled with adsorbed liquid and solid argon within the context of elasticity and compare the modeling results with the ultrasonic measurements. The modeling requires the knowledge of solid moduli of Vycor glass and the pore geometry, which cannot be measured directly. Instead, we estimate these parameters from the dry moduli using so-called Differential Effective Medium (DEM) theory, in which the pores are assumed to be of spheroidal shape characterized by a single aspect ratio. Predictions of the Gassmann equation give an excellent fit to the measured elastic moduli of Vycor glass completely filled with liquid argon at temperature 80 K. Estimates of the DEM show a reasonable agreement with ultrasonic measurements on the elastic moduli of Vycor glass fully saturated with solid argon at 74 K in shear modulus but a significant overestimate in bulk modulus. This might be due to the effects of the confinement on the moduli of argon in nanopores. Although the validation and generalization of this conclusion requires further laboratory experiments for a number of well characterized solid–fluid systems, our finding shed light on the understanding of elastic properties of nanoporous materials mixed with adsorbates in various phases. These results provide steps toward development of methods for ultrasonic characterization of confined fluid and solid phases.

Keywords Ultrasound · Characterization · Elasticity · Effective medium theory · Vycor

1 Introduction

Gas adsorption is a classical tool used for characterization of porous materials (Gregg and Sing 1982). When adsorption in porous material is studied, the primary interest is typically focused on an adsorption isotherm, which provides a lot of information about the porous material and its interaction

with the adsorbate (Thommes and Cychosz 2014; Thommes et al. 2015). In recent years, however, the idea of using data complementary to adsorption isotherms for extracting the information about the porous materials has started to attract attention. In particular the mechanical effects of adsorption are of interest, e.g. the adsorption-induced deformation (Gor et al. 2017); the strain isotherms measured during the adsorption process strongly depend on the pore size and surface chemistry, and thus are suitable fingerprints of the materials (Kowalczyk et al. 2016; Balzer et al. 2016; Ustinov and Do 2006; Siderius et al. 2017).

Another approach is to probe the elastic properties of adsorbates in the pores, which are also related to the pore-sizes (Gor et al. 2015; Dobrzanski et al. 2018; Maximov and Gor 2018) and surface properties (Evans and Stewart 2015; Nygård 2016; Gor 2017). The elastic properties of adsorbates can be readily probed by ultrasound, as the speeds of acoustic waves propagation have simple relations to elastic

✉ Gennady Y. Gor
gor@njit.edu
<http://porousmaterials.net/>

¹ Department of Exploration Geophysics, Curtin University, GPO Box U1987, Perth, WA 6845, Australia

² CSIRO Energy, 26 Dick Perry Avenue, Kensington, WA 6151, Australia

³ Otto H. York Department of Chemical and Materials Engineering, New Jersey Institute of Technology, Newark, NJ, USA

moduli. Ultrasound has been employed for studying numerous adsorbates (Molz et al. 1993; Page et al. 1995; Charnaya et al. 2001; Schappert and Pelster 2008; Warner and Beamish 1988), bringing, in particular, information of amount adsorbed (Warner and Beamish 1988), dynamics of pore filling (Page et al. 1995), pressures in the pores (Schappert and Pelster 2016), solid–liquid phase transitions (Charnaya et al. 2001), etc... However, many of those results were qualitative rather than quantitative. In order to make the ultrasonic data measured in porous materials quantitative, the knowledge of elasticity of composite materials has to be employed. The application of theories used for *macroporous* materials to *nanoporous* materials is questionable, because nanostructured materials, as well as nanoconfined matter, may exhibit physical properties that differ substantially from the properties of “normal” bulk materials (Huber 2015).

Recently, Gor and Gurevich (2018) showed that the elastic moduli of Vycor glass fully saturated with adsorbed fluids, such as argon (Schappert and Pelster 2014) and *n*-hexane (Page et al. 1995), are consistent with the predictions of the Gassmann equation (Gassmann 1951), which relates elastic moduli of saturated porous media to the moduli of the dry porous matrix and the saturating fluid. However, the Gassmann theory also requires the knowledge of the bulk modulus of the solid Vycor matrix, which cannot be measured directly. Gor and Gurevich (2018) estimated this modulus in two independent ways: (1) from deformation of the Vycor glass caused by adsorption of water (Amberg and McIntosh 1952) and (2) from the moduli of the dry Vycor glass using effective medium theory (EMT). These two approaches gave similar values, and were used by Gor and Gurevich (2018) to compute the end members of the predictions of the Gassmann equation. However both approaches have their weaknesses. The drawback of the first approach is that the adsorption-induced deformation data used for the calculation of bulk modulus were measured over 65 years ago, and it is not certain that the samples measured were identical to the ones used in the ultrasonic experiments. The second approach has an uncertainty related to the shapes of nanopores in the Vycor glass, which are necessary for the calculation of elastic moduli using the EMT. Moreover, the estimates made were based on the assumption that the pores are circular cylinders, as often accepted for interpreting adsorption data in Vycor glass (Thommes et al. 2006; Landers et al. 2013; Kolesnikov et al. 2018). In addition, the question of estimating the elastic moduli of Vycor glass completely saturated with solid adsorbates remains open.

Recently Schappert and Pelster (2013b) reported ultrasonic measurements on the elastic moduli of Vycor glass saturated with adsorbed solid argon. These data, together with the previous measurements of Vycor glass saturated with liquid argon (Schappert and Pelster 2013a), can help quantify the effect of various adsorbates on the elastic

properties of nanoporous materials. Within the context of elasticity, we study these quantitative effects by comparing the experimental data against the EMT modeling results. Such EMT modeling requires the knowledge of solid moduli of Vycor matrix and the geometrics of nanopores, which cannot be measured directly from the laboratory experiments. In this work, we estimate these parameters from the dry moduli using one specific EMT, so-called Differential Effective Medium (DEM) theory. Then, substituting these parameters as well as the elastic moduli of both liquid and solid argon into the same DEM, we investigate the change of elastic properties of nanoporous Vycor glass filled with various phase adsorbates. This paper provides a framework that helps understand the quantitative effects of liquid and solid adsorbates on the elastic properties of a composite nanoporous system.

2 Data

To achieve understanding of the effects of various adsorbates on the elastic properties of a nanoporous medium, it is useful to start with a simple system. We consider the ultrasonic measurements carried out during adsorption of vapors on a Vycor glass, in which the pores are filled with liquid and solid argon. From the molecular standpoint argon is one of the simplest adsorbates, due to its non-specific van der Waals interactions between the argon atoms and with the glass surface, and it is straightforward to model argon adsorption and its elastic properties in particular via molecular simulations (Coasne et al. 2009; Gor et al. 2015, 2016; Dobrzanski et al. 2018). Therefore, the system of Vycor glass and adsorbed argon can be regarded as an ideal system to study the influences of nanoconfinement on thermodynamics of fluids, in particular its elastic properties, as well as the liquid–solid phase transitions.

In this paper, we use the data of Schappert and Pelster (2008, 2013a, b, 2014), who measured the adsorbed fraction dependence of ultrasonic velocities in a Vycor glass 7930, saturated with argon at temperatures of $T = 80$ K (liquid) and 74 K (solid) (we call it sample 1). Note that confined argon freezes at lower temperature than the melting point of bulk argon ($T = 84$ K), and in pores of Vycor glass is frozen below $T = 76$ K (Schappert and Pelster 2011). In the experiments of Schappert and Pelster (2008, 2013a, b, 2014), a dry Vycor glass is gradually saturated by means of vapor adsorption at a constant temperature.

Figure 1a, b show the ultrasonic measurements on the effective bulk and shear moduli of a Vycor glass during adsorption (solid red squares) and desorption (open red squares) of liquid argon at $T = 80$ K as a function of filling fraction of argon. Figure 1b shows that the effective shear modulus remains almost independent of argon saturation,

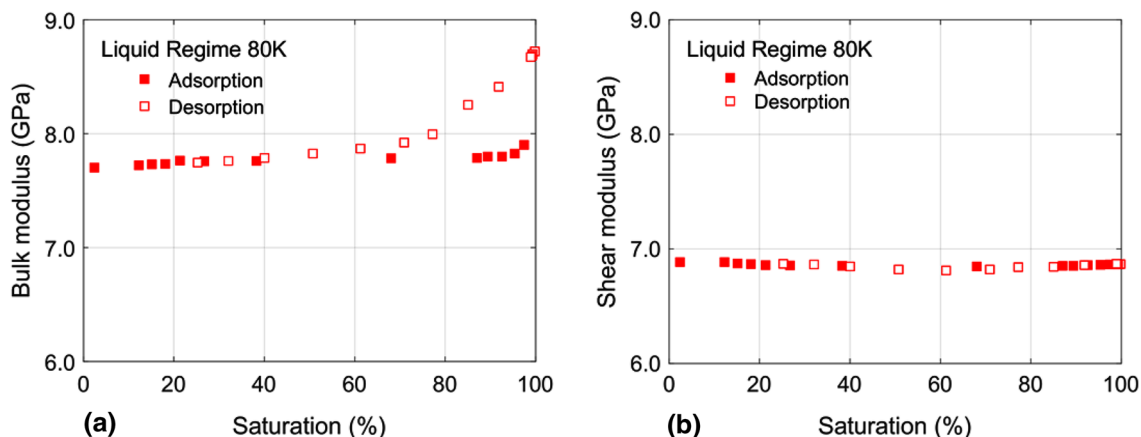


Fig. 1 Effective bulk and shear moduli of Vycor glass during filling the pores with liquid argon at T=80 K as a function of filling fraction of argon (bulk $K_0=7.73$ GPa and shear $G_0=6.86$ GPa moduli of the dry sample)

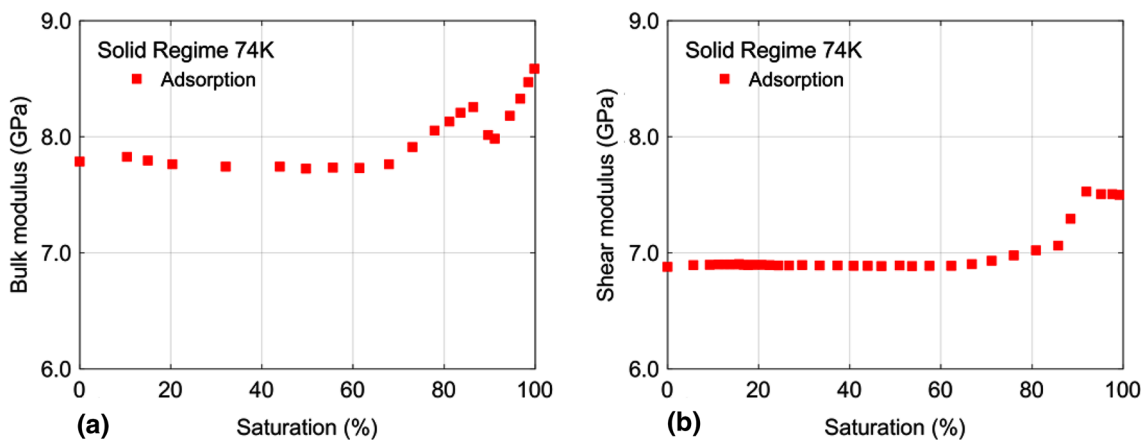


Fig. 2 Effective bulk and shear moduli of Vycor glass during filling with solid argon at T=74 K as a function of filling fraction of argon (bulk $K_0=7.79$ GPa and shear $G_0=6.88$ GPa moduli of the dry sample)

which implies that the adsorbed liquid argon does not affect the effective shear modulus of the porous sample. At the same time, the effective bulk modulus increases sharply upon capillary condensation when the filling fraction approaches 100%. This result is consistent with the conventional theory of poroelasticity (Gassmann 1951; Biot 1956) and suggests that the nanoconfined argon at 80 K is in liquid state.

Figure 2a, b show the ultrasonic measurements on the effective bulk and shear moduli of the same Vycor glass filled with solid argon at T=74 K, which is below the freezing point of argon confined in Vycor nanopores T=76 K (Schappert and Pelster 2011). The moduli are plotted as a function of filling fraction of argon. Similarly to the Vycor glass filled with liquid argon, both the effective bulk and shear moduli remain almost constant until the filling fraction approaches 0.66. Within the range of 0.66–0.89, both

the effective bulk and shear moduli show a gradual increase, which implies the increased amount of frozen argon. When the filling fraction is 0.89 at T=74 K, the shear modulus remains approximately constant at further filling while the effective bulk modulus continues to increase. No appropriate explanation has been found so far in literature to account for this significant difference, which might lead to non-negligible effects on our modeling results. Given that our focus in this paper is the case of full saturation $f=100\%$, this behavior at partial saturation will be the attention of our future work.

Computing the effective elastic properties of Vycor glass saturated with liquid or solid argon requires the knowledge of the elastic properties of each constituent, the volume fractions of the components, and the spatial distributions of how the various phases are arranged relative to each other. In this work, we have the dry moduli K_0

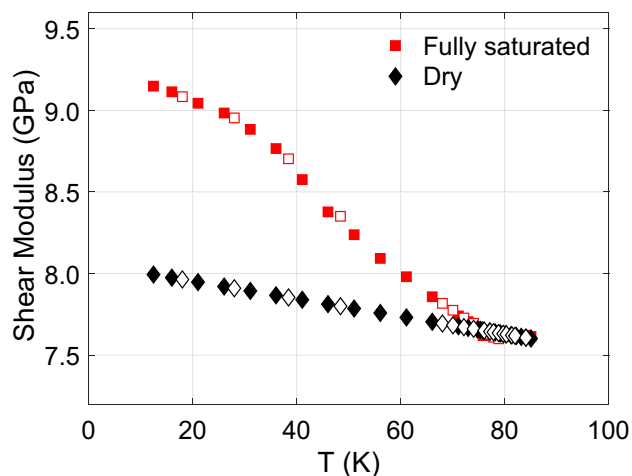


Fig. 3 Effective shear modulus during temperature cycles, cooling (closed markers) and heating (open markers), for different fillings of Vycor glass. Note that the effective shear modulus of the completely filled sample increases markedly on cooling. In this case, the value of the slope of the increase, however, is considerably smaller for temperatures below about 30 K

and G_0 , porosity ϕ , and saturated moduli. However, the moduli K_s and G_s of Vycor matrix [sometimes referred to as backbone, see Bentz et al. (1998)], cannot be measured directly because the same Vycor cannot be manufactured in non-porous form. The knowledge of the dry moduli K_0 and G_0 is insufficient to estimate K_s and G_s , as the dependence of the dry moduli K_0 and G_0 on the solid moduli K_s and G_s is controlled by the pore geometry, which is also too complex. Therefore, additional information is required to obtain K_s and G_s .

Such information is contained in the ultrasonic measurements on the elastic properties of Vycor glass fully saturated with liquid and solid argon if the moduli of “bulk” liquid and solid argon are known. These values are indeed well documented (Keeler and Batchelder 1970; Anderson and Swenson 1975; Shimizu et al. 2001; Barker and Dobbs 1955). However, ultrasonic measurements show that argon confined in Vycor glass may not be completely frozen at $T = 74$ K (Schappert and Pelster 2013a), and its moduli may be lower than that of bulk argon. Specifically, Schappert and Pelster (2013a) showed that the shear modulus of Vycor glass saturated with argon increases continuously with the decrease of temperature down to $T = 12$ K, and this increase is much more rapid than for dry Vycor glass, see Fig. 3. These measurements were done on a slightly different sample, which we call sample 2, with a porosity of 25%, which is smaller than that of sample 1 (28%). However since all Vycor glass was produced using a standard manufacturing process, it is reasonable to assume that these two samples share the same solid moduli K_s and G_s .

3 Methods

Generally, the effective elastic properties of a porous medium depend on the elastic properties of each constituent, the volume fractions of the various components, and the spatial distributions of how the various phases are arranged relative to each other. If the geometrical details are unknown, the predictions are limited to the upper and lower bounds of effective elastic properties of the composite medium. A number of theories have been developed to find possible ranges of the effective elastic properties of the composite medium regardless of any geometric details. For any given volume fraction of constituents, the effective moduli will fall between the bounds, but the position of the moduli between the bounds depends on the geometric details (Mavko et al. 2009). Another group of approaches are based on effective medium theories (EMT), which describe the macroscopic elastic properties of a composite medium in terms of the volume fractions and the constituent moduli, assuming a specific inclusion geometry. Here we consider one bound method, Hashin–Shtrikman (HS) bounds (Hashin and Shtrikman 1963), which are the tightest possible bounds for isotropic mixtures, and one EMT method, the modified Kuster–Toksöz theory (KT) (Kuster and Toksöz 1974; Berryman 1980), which is called the differential effective medium (DEM) theory (Cleary et al. 1980; Norris 1985; Zimmerman 1990). This method is exact for low porosity and takes into account the interactions between pores for high porosity. These two approaches are described as follows.

3.1 Rigorous bounds

One common way to estimate the elastic properties of multiple materials is to find the bounds or the ranges of solutions, especially when the microstructure is unknown or too complicated. Berryman (1980) discussed various rigorous bounds on the effective moduli of composites. For example, the well-known Voigt (arithmetic) and Reuss (harmonic) averages are, respectively, rigorous upper and lower bounds for both bulk K and shear G moduli. Tighter bounds for elastic moduli of isotropic mixtures have been derived by Hashin and Shtrikman (1963). Moreover it has been shown that HS bounds are realizable, that is, for any volume fractions of the constituents, there always exists their possible geometrical configuration for which HS bounds are exact. The expressions for HS bounds are given by

$$K^{HS\pm} = K_s + \frac{\phi}{(K_f - K_s)^{-1} + (1 - \phi)\left(K_s + \frac{4}{3}G_s\right)^{-1}} \quad (1)$$

$$G^{HS\pm} = G_s + \frac{\phi}{(G_f - G_s)^{-1} + \frac{2(1-\phi)}{5} \frac{(K_s + 2G_s)}{G_s} \left(K_s + \frac{4}{3}G_s\right)^{-1}} \quad (2)$$

where K and G are the bulk and shear moduli of two constituents denoted by subscripts s and f with volume fractions $(1 - \phi)$ and ϕ , respectively. These expressions give the upper bound (denoted by ‘+’) when constituent s is stiffer than constituent f , and the lower bound (denoted by ‘-’) when constituent f is stiffer than constituent s .

3.2 Specific inclusion shape methods

In addition to rigorous bounds there are methods to estimate the effective moduli for particular geometries. These methods are collectively known as effective medium theories or EMT. Most EMT methods use the solution for the elastic deformation of a single inclusion of one material in an infinite background medium of the second material and then use one scheme or another to estimate the effective moduli when there is a distribution of these inclusions (Mavko et al. 2009). In particular, the KT theory is based on the long wavelength, first-order scattering of elastic waves in a two-phase medium (Berryman 1980). According to this theory, effective elastic bulk and shear moduli K and G of a mixture of a solid with the moduli K_s and G_s with a volume fraction $1 - \phi$, and fluid or solid pore filling with the moduli K_f and G_f and volume fraction ϕ , are given by the equations

$$(K - K_s) \frac{\left(K_s + \frac{4}{3}G_s\right)}{\left(K + \frac{4}{3}G_s\right)} = \phi(K_f - K_s)P^{sf} \tag{3}$$

$$(G - G_s) \frac{(G_s + \zeta_s)}{(G + \zeta_s)} = \phi(G_f - G_s)Q^{sf} \tag{4}$$

where $\zeta_s = \frac{G_s(9K_s+8G_s)}{6(K_s+2G_s)}$. The coefficients P^{sf} and Q^{sf} describe the effect of an inclusion in a background medium s , and depend on the inclusion shapes. Wu (1966) gave the expressions for spheroidal inclusions of arbitrary aspect ratio α as

$$P = \frac{1}{3}T_{ijij} \tag{5}$$

and

$$Q = \frac{1}{5}\left(T_{ijij} - \frac{1}{3}T_{ijij}\right) \tag{6}$$

where the tensor $T_{ijkl}(K_s, G_s, K_f, G_f, \alpha)$ relates the uniform far-field strain field to the strain within the spheroidal inclusion and is a function of the host and inclusion moduli as well as the pore aspect ratio α . Detailed mathematical expressions of the components of the tensor T_{ijkl} are given in (Berryman 1980). When the pore space is empty ($K_f = 0; G_f = 0$), Eqs. (3) and (4) reduce to

$$(K_s - K_0) \frac{\left(K_s + \frac{4}{3}G_s\right)}{\left(K_0 + \frac{4}{3}G_s\right)} = \phi K_s P^{s0}, \tag{7}$$

$$(G_s - G_0) \frac{(G_s + \zeta_s)}{(G_0 + \zeta_s)} = \phi G_s Q^{s0}, \tag{8}$$

where superscript 0 indicates that coefficients P and Q are calculated for empty pores.

The KT model described by Eqs. (3), (4) and (7), (8) is exact in the limit of small volume fraction of inclusions, but might be inaccurate for large volume fractions and may even violate rigorous bounds, especially for strongly oblate inclusions (Berryman 1980). Since the porosity of Vycor (0.25–0.28) glass is not small, it is preferable to use the KT model in an iterative manner, by adding a small amount of inclusions at each iteration. Such scheme is known as the differential effective medium (DEM) (Cleary et al. 1980; Norris 1985; Zimmerman 1990). The DEM scheme is known to be realizable, that is, there always exists a geometrical configuration, for which its predictions are exact (Norris 1985; Milton 2002). In the following analysis we will use the DEM for our calculations, but will still refer to Eqs. (3)–(8) for simplicity.

Most commonly, the DEM scheme is used to estimate the effective bulk K and shear G moduli from porosity ϕ , bulk and shear moduli of the solid matrix K_s and G_s , and the pore geometry α . Here we do the opposite: using the DEM for empty pores, we estimate the solid moduli K_s and G_s and the pore geometry α from the bulk K_0 and shear G_0 moduli of the dry sample and the porosity ϕ . Then, these parameters are substituted into the same DEM and the Gassmann equation but for argon-filled pores to predict the effective elastic moduli of nanoporous medium filled with adsorbed fluids or solids and compared with the ultrasonic measurements.

3.3 The Gassmann equation

When the pore is filled with a fluid ($G_f = 0$), the effective bulk modulus K of the fluid-saturated medium is related to the dry bulk modulus K_0 by an exact equation known as the Gassmann equation (Gassmann 1951; Berryman 1999)

$$K = K_0 + \frac{\left(1 - \frac{K_0}{K_s}\right)^2}{\frac{\phi}{K_f} + \frac{1-\phi}{K_s} - \frac{K_0}{K_s^2}}. \tag{9}$$

Equation (9) shows that the bulk modulus K of the saturated medium is fully determined by the bulk moduli of the solid K_s , dry frame K_0 and fluid K_f , and the porosity ϕ , and

is independent of the aspect ratio of the pores. However, the dependence on pore shape is implicit in Eq. (9) as it controls the ratio K_0/K_s . At the same time, the shear modulus of the fluid-saturated medium G equals to that of the dry material G_0 ,

$$G = G_0. \quad (10)$$

the Gassmann equation is widely used in exploration and production geophysics to estimate properties of subsurface fluids from seismic reflections (Smith et al. 2003). The Gassmann equation provides an exact link between dry and saturated moduli irrespective of geometry, and hence for fluid saturated materials is preferable to any other EMT.

3.4 Workflow

Using the data presented in Sect. 2, we develop a workflow combining the data of sample 1 and sample 2 to obtain the solid moduli K_s and G_s and the pore geometry α according to the DEM theory. Then, the effective moduli of Vycor glass completely filled with liquid and solid argon are obtained by substituting these parameters into the same DEM theory. These predictions are then compared to the ultrasonic measurements. Detailed workflow is as follows:

1. Assuming the Poisson's ratio ν of the dry Vycor glass is independent of temperature and equals that of sample 1, we obtain the dry bulk modulus K_0 at $T=30$ K from the measured dry shear modulus G_0 of sample 2 at this temperature. The temperature of 30 K is taken as a reference, since at a higher temperature it is known that thermodynamic properties of confined solid argon noticeably differ from those of the bulk argon (Molz et al. 1993; Knorr et al. 2003).
2. For sample 2 at $T=30$ K, we calculate the solid moduli K_s , G_s , and the aspect ratio α from the dry moduli K_0 and G_0 , and the effective shear modulus G of Vycor glass fully saturated with solid argon using the Eqs. (7) and (8).
3. We attribute the temperature dependence of the shear modulus of the dry Vycor sample 2, shown in Fig. 3, to the variation of solid modulus. This dependence gives a factor 1.03 for the difference between the moduli at $T=74$ K and at $T=30$ K. Thus, we obtain the solid shear modulus G_s at $T=74$ K.
4. Assuming that sample 1 and sample 2 share the same solid shear modulus G_s at $T=74$ K, we calculate the solid bulk modulus K_s and the aspect ratio α from the dry moduli K_0 and G_0 and the solid shear modulus G_s of sample 2 using the Eqs. (7)–(9).

5. Substituting the solid moduli K_s and G_s and the aspect ratio α into the Eqs. (3) and (4) and the Gassmann Eq. (9), we estimate the effective elastic moduli of Vycor glass fully saturated with liquid and solid argon and compare the modeling results to the ultrasonic measurements.

4 Results

Using the ultrasonic measurements on the elastic moduli of Vycor glass (sample 1 and 2) completely filled with adsorbed liquid and solid argon shown in Sect. 2, we carry out the modeling using the methods presented in Sect. 3 and compare the results to the experiments.

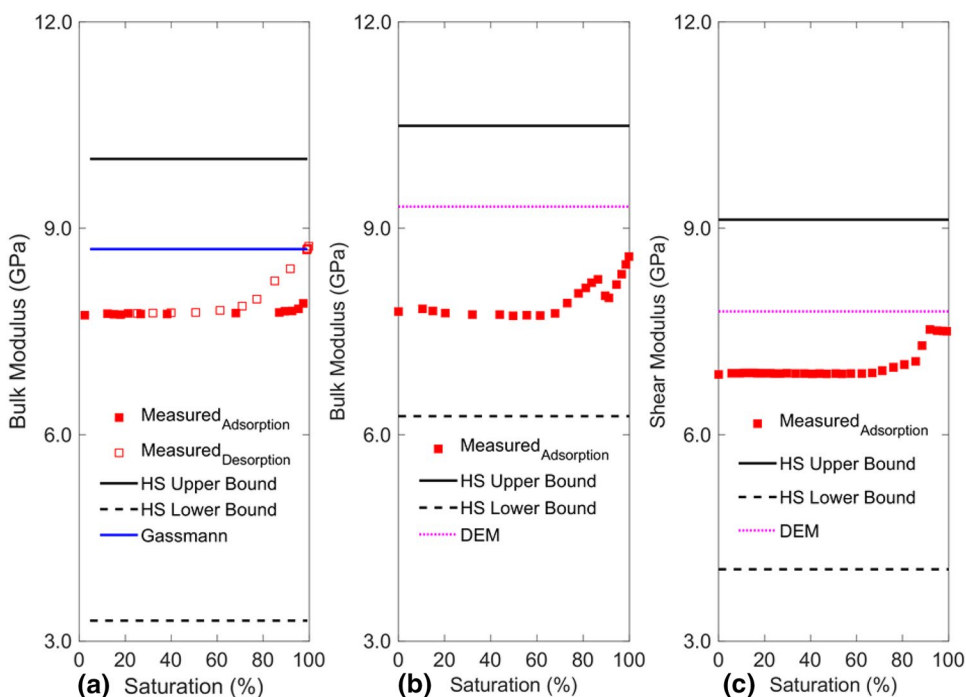
4.1 Deriving solid moduli of Vycor matrix from the data of sample 2 at $T=30$ K

As presented in the workflow, both the bound estimates and the EMT theories require the knowledge of the solid moduli of Vycor matrix, which cannot be measured directly. In this work, we use the DEM theory, in which the pore structure is modelled as a spheroid characterized by a single pore aspect ratio α , to estimate the solid moduli K_s and G_s based on the data of both sample 1 and 2.

Since all Vycor is produced using the same manufacturing process, we assume that sample 1 and 2 should share the same solid moduli. As presented in Fig. 2, Schappert and Pelster (2008) reported the bulk modulus $K_0=7.73$ GPa, the shear modulus $G_0=6.86$ GPa, and the porosity $\phi=0.28$ of the dry sample 1. Further, for the same sample used in experiments with solid argon at $T=74$ K, Schappert and Pelster (2013b) reported slightly higher values: the bulk modulus $K_0=7.79$ GPa and the shear modulus $G_0=6.86$ GPa (the difference could be due to a slight temperature dependence of the properties of Vycor glass or a slight difference in pore geometry). However, the pore geometric details are unknown, which means that the effective aspect ratio α of the pores is unavailable. Hence Eqs. (7) and (8) cannot be solved for three unknowns.

As discussed earlier, Schappert and Pelster (2013a) reported the variation of the effective shear modulus of Vycor glass (sample 2) saturated with adsorbed argon against temperature, which is presented in Fig. 3. At $T=30$ K, the shear moduli of sample 2 when dry and filled with solid argon are $G_0=7.90$ GPa and $G=8.87$ GPa respectively. It is reasonable to assume that the Poisson's ratio ν of the dry Vycor glass is independent of temperature and equals that of sample 1 ($\nu=0.31$). This yields the dry bulk modulus of sample 2 $K_0=8.94$ GPa. Then

Fig. 4 Predictions of the Gassmann equation (solid blue line), the DEM theory (magenta dotted lines), HS bounds (black dashed and solid lines) for the elastic moduli of Vycor glass against ultrasonic measurements (squares) as a function of the filling fraction of argon: bulk modulus of Vycor glass saturated with liquid argon (**a**); bulk (**b**) and shear (**c**) moduli of Vycor glass saturated with solid argon. The pore geometry is modelled as a spheroid with an aspect ratio of 0.75 (Color figure online)



Eqs. (7) and (8) can be written for the dry bulk and shear moduli K_0 and G_0 , while Eq. (4) gives the effective shear modulus G of the solid argon filled sample 2. These three equations can be solved for three unknowns (K_s , G_s and α) provided the elastic moduli of solid argon at $T = 30$ K are known. For the solid argon moduli, we use the data of Barker and Dobbs (1955), who reported the bulk $K_f = 2.27$ GPa and shear $G_f = 1.10$ GPa moduli of solid argon at $T = 30$ K. Solving the equations with these moduli gives $K_s = 16.69$ GPa, $G_s = 15.82$ GPa, and $\alpha = 0.68$. Note that the dry shear modulus $G_0 = 7.90$ GPa at $T = 30$ K is higher than at $T = 74$ K (7.67 GPa) by a factor 1.03. As the temperature dependence of the dry shear modulus G_0 is caused by the corresponding variation of the solid modulus G_s , the latter should be smaller at $T = 74$ K than at $T = 30$ K by a factor 1.03, and thus equals $G_s = 15.36$ GPa.

4.2 Constituent moduli used for estimating the elastic moduli of Vycor glass fully saturated with liquid argon at $T = 80$ K and solid argon at $T = 74$ K

With the dry bulk K_0 and shear moduli G_0 of sample 1 as well as the solid shear modulus $G_s = 15.36$ GPa derived from sample 2 at $T = 74$ K, we solve the Eqs. (7) and (8) to obtain the solid bulk modulus of Vycor matrix $K_s = 15.94$ GPa and the pore aspect ratio $\alpha = 0.75$ of sample 1. The value $K_s = 15.94$ GPa is close to the value $K_s = 16.1$ GPa estimated by Gor and Gurevich (2018) from adsorption-induced deformation experiments but slightly smaller than that we derived

for sample 2 at $T = 30$ K ($K_s = 16.20$ GPa). This difference is unlikely to affect our modeling results, as the estimate of G_s from the DEM theory is relatively insensitive to K_0 . Moreover, the value K_s is not used for any further calculations.

Calculation of the effective elastic moduli of Vycor glass completely filled with liquid and solid argon using the DEM theory also requires the elastic moduli K_f and G_f of liquid and solid argon at the corresponding temperature. For liquid argon at $T = 80$ K, we use the value $K_f = 1.06$ GPa (Gor et al. 2015). For solid argon at $T = 74$ K, we use $K_f = 1.88$ GPa and $G_f = 0.85$ GPa, which are also given by Barker and Dobbs (1955). These values are consistent well with the later measurements by Keeler and Batchelder (1970).

4.3 Comparison of the predictions by the DEM with the ultrasonic measurements at $T = 74$ and $T = 80$ K

Substituting the constituent moduli into the same DEM theory, Eqs. (3), (4), and the HS bounds, Eqs. (1), (2), give the predictions of the effective elastic properties of Vycor glass fully saturated with liquid and solid argon. Figure 4a–c show the comparison between the predictions of the effective elastic moduli of Vycor glass saturated with liquid or solid argon and the experiments as a function of the filling fraction. Solid and dashed lines give the predictions of different methods presented in Sect. 3. Figure 4a shows that the prediction of the Gassmann equation for Vycor glass fully ($f = 1$) saturated with liquid argon at $T = 80$ K gives

an excellent agreement with the ultrasonic measurements. This conclusion was drawn earlier by Gor and Gurevich (2018), who obtained the solid modulus K_s in a different way, namely from adsorption-induced deformation.

Figure 4b, c show the predictions of the effective bulk and shear moduli of Vycor glass fully ($f=1$) saturated with solid argon using the DEM theory (magenta dotted line) and the HS bounds (black dashed and solid lines), and the experimental data (red squares, both open and closed symbols). We observe that the DEM theory significantly overestimates the effective bulk modulus of Vycor glass fully saturated with solid argon at $T=74$ K, as shown in Fig. 4b. At the same time, for the effective shear modulus (Fig. 4c), the prediction is within 0.2 GPa from the experiments, which is probably within the measurement error.

5 Discussion

We have explored the applicability of elastic mixture theories to nanoporous medium, commonly employed and proved effective in describing the wave propagating in macroporous media. To this end, we have applied these theories to the ultrasonic measurements on Vycor glass saturated with liquid and solid argon. Since the solid moduli of Vycor matrix K_s and G_s are unknown, we chose to invert these values from the experimental data of dry and solid argon-filled shear modulus of Vycor glass at $T=30$ K. The values K_s and G_s were then used to predict the effective elastic moduli of Vycor glass completely filled with liquid argon at $T=80$ K and solid argon at $T=74$ K respectively.

We have found that predictions of the Gassmann equation give an excellent fit to the ultrasonic measurements on the elastic moduli of Vycor glass fully saturated with liquid argon at $T=80$ K. This agreement was earlier concluded by Gor and Gurevich (2018) using the solid modulus K_s estimated in a different way, namely from adsorption-induced deformation. The estimated effective shear modulus of Vycor glass completely filled with solid argon at $T=74$ K by the DEM theory also shows a reasonable fit to the experiments. However, we observe a significant discrepancy in the effective bulk modulus. This might have resulted from several possible reasons:

First, Schappert and Pelster (2013a) pointed out that the phase transition of argon in completely filled pores might not be instant but continuous over a broad temperature range of about 45 K (from 75 K down to 30 K). At $T=74$ K, some portion of the filling argon probably remains in the liquid state. However, given that the predicted effective shear modulus is much closer to the ultrasonic measurements than the bulk modulus, the existence of liquid argon at $T=74$ K is not

consistent with the data, as the presence of the liquid argon would have affected the effective shear modulus to a greater extent than the bulk modulus (since the shear modulus of liquid is zero).

Second, the confinement of argon in nanopores might affect its elastic moduli. Note that all the elastic moduli of both liquid and solid argon we use in this work are the properties of “bulk” argon. Moreover, it is unclear whether the confinement affects the bulk and shear moduli in the same way. Ultrasonic measurements, presented in Fig. 4a, b, show that the effective bulk modulus of Vycor glass saturated with solid argon at $T=74$ K is very close to that for Vycor filled with liquid argon at $T=80$ K. This suggests that the bulk modulus of confined argon at $T=74$ K (which is close to the melting point of argon in confinement of $T=76$ K) might be close to that of liquid argon at $T=80$ K. Note that this conclusion follows directly from the experiments, and not from any theories used for our calculations.

Additionally, an important assumption of our estimates is that all the components of the mixture are isotropic. However, Keeler and Batchelder (1970) observed that solid argon exhibits its elastic anisotropy, which might affect the elastic properties of the mixture. Yet, it appears unlikely for this effect to lead to the significant difference between the effective bulk and shear moduli.

It is insightful to compare the composite models used above for the elastic properties of Vycor glass to the models used to model its adsorption properties. Adsorption studies also rely on simple geometrical models for pores, mainly slit-shaped, cylindrical and spherical (Thommes and Cychoz 2014). Adsorption isotherms on Vycor glass, which has long channel-like pores, are typically described within the cylindrical pore model (Landers et al. 2013). A recent molecular simulation study of elastic properties of argon confined in silica mesopores suggested that a spherical pore model is more reliable and free of some artifacts related to the anisotropy of fluid confined in cylindrical pores (Gor et al. 2015; Dobrzanski et al. 2018). Our analysis shows that the pore geometry might be slightly ‘stiffer’ than cylinders but ‘softer’ than spheres: the average pore stiffness is comparable to that of spheroids with an aspect ratio of about 0.75.

Our analysis is based on a single aspect ratio, which is a limitation. Apparently the aspect ratio range is not very broad, as evidenced by lack of dependence of the Vycor sample shear modulus on liquid fraction. Indeed, the presence of low-aspect ratio pores (cracks) in addition to near spherical or cylindrical ones would cause a variation of the shear modulus with liquid fraction (O’Connell and Budiansky 1977; Mavko and Jizba 1991). Yet the measured shear modulus of Vycor is almost exactly independent of liquid fraction (Fig. 1b). According to the squirt flow theory (Jones 1986; Müller et al. 2010), this

means that the smallest aspect ratio α present in such quantity as to have an effect on elastic properties is larger than a critical aspect ratio α_c defined by the equation

$$\alpha_c = \sqrt[3]{\frac{f\eta}{K_s}}, \quad (11)$$

where K_s is the bulk modulus of the solid. For the parameters of liquid argon in Vycor (viscosity $\eta = 2.7 \times 10^{-4}$ Pa s) and frequency of ultrasonic experiments ($f = 6\text{--}13$ MHz), this means that $\alpha \gg 0.01$. Still there may be a range of aspect ratios > 0.1 , which our approach does not account for. Unfortunately, to our knowledge no information on the distribution of pore shapes in Vycor is available in the literature. In the absence of such information, a single aspect ratio is the most reasonable approach, as the corresponding model will have the minimal number of parameters. However, the range of aspect ratios $\alpha > 0.1$ may still be responsible for some of the discrepancy between model predictions and observations.

6 Conclusions

We have explored the validity and applicability of elasticity, widely employed and proved effective in macroporous medium, within a nanoporous medium. Our analysis shows that predictions of the Gassmann equation give an excellent fit to the ultrasonic measurements on the effective elastic moduli of Vycor glass fully saturated with liquid argon at $T = 80$ K. Very small deviations are observed, which probably are related to the confinement effects on the thermodynamics of argon in nanopores. This observation is consistent with the calculations from molecular modeling (Gor 2014; Gor et al. 2015; Dobrzanski et al. 2018).

Theoretical estimates using the DEM theory also agree well in the effective shear modulus of Vycor glass completely filled with solid argon at $T = 74$ K, which is probably within the measurement errors, but significantly overestimate the effective bulk modulus. Three possible reasons are proposed to explain the discrepancy. The first one is that the phase transition of argon is not thoroughly finished at such temperature. Some portion of argon still remains in the liquid state. Another important reason is that solid argon exhibits non-negligible anisotropy, which might affect the effective elastic properties of the mixture. Last but not the least, the discrepancy suggests that although the shear modulus of solid argon confined in nanopores is close to that of bulk argon at such temperature, the bulk modulus might be totally different, showing a significantly lower value than that of bulk argon. This peculiarity of confined solid argon

is consistent with the observation of some other thermodynamic properties (Molz et al. 1993; Wallacher and Knorr 2001).

Although further laboratory experiments for a number of well characterized solid–fluid systems are required to verify these conclusions, our results shed light on the understanding of elastic properties of nanoporous materials saturated with various adsorbates and provide steps toward development of methods for ultrasonic characterization of confined fluid and solid phases.

Acknowledgements The authors thank the sponsors of the Curtin Reservoir Geophysics Consortium and China Scholarship Council (CSC) for financial support, and Stanislav Glubokovskikh and Patrick Huber for useful discussions.

References

- Amberg, C., McIntosh, R.: A study of adsorption hysteresis by means of length changes of a rod of porous glass. *Can. J. Chem.* **30**(12), 1012–1032 (1952)
- Anderson, M., Swenson, C.: Experimental equations of state for the rare gas solids. *J. Phys. Chem. Solids* **36**(3), 145–162 (1975)
- Balzer, C., Cimino, R.T., Gor, G.Y., Neimark, A.V., Reichenauer, G.: Deformation of microporous carbons during N₂, Ar, and CO₂ adsorption: insight from the density functional theory. *Langmuir* **32**(32), 8265–8274 (2016)
- Barker, J., Dobbs, E.: CXX. Measurement of the elasticity of solid argon with an ultrasonic interferometer. *Lond. Edinb. Dubl. Phil. Mag.* **46**(381), 1069–1080 (1955)
- Bentz, D.P., Garboczi, E.J., Quenard, D.A.: Modelling drying shrinkage in reconstructed porous materials: application to porous Vycor glass. *Model. Simul. Mater. Sci. Eng* **6**(3), 211 (1998)
- Berryman, J.G.: Long-wavelength propagation in composite elastic media II. Ellipsoidal inclusions. *J. Acoust. Soc. Am.* **68**(6), 1820–1831 (1980)
- Berryman, J.G.: Origin of Gassmann's equations. *Geophysics* **64**(5), 1627–1629 (1999)
- Biot, M.A.: Theory of propagation of elastic waves in a fluid-saturated porous solid. I. Low frequency range. *J. Acoust. Soc. Am.* **28**(2), 168–178 (1956)
- Charnaya, E., Plotnikov, P., Michel, D., Tien, C., Borisov, B., Sorina, I., Martynova, E.: Acoustic studies of melting and freezing for mercury embedded into Vycor glass. *Physica B* **299**(1–2), 56–63 (2001)
- Cleary, M.P., Lee, S.-M., Chen, I.-W.: Self-consistent techniques for heterogeneous media. *J. Eng. Mech* **106**(5), 861–887 (1980)
- Coasne, B., Czwartos, J., Sliwiska-Bartkowiak, M., Gubbins, K.E.: Effect of pressure on the freezing of pure fluids and mixtures confined in nanopores. *J. Phys. Chem. B* **113**(42), 13874–13881 (2009)
- Dobrzanski, C.D., Maximov, M.A., Gor, G.Y.: Effect of pore geometry on the compressibility of a confined simple fluid. *J. Chem. Phys* **148**(5), 054503 (2018)
- Evans, R., Stewart, M.C.: The local compressibility of liquids near non-adsorbing substrates: a useful measure of solvophobicity and hydrophobicity? *J. Phys. Condens. Matter* **27**(19), 194111 (2015)
- Gassmann, F.: Über die Elastizität poröser Medien. *Vierteljahrsschrift der Naturforschenden Gesellschaft in Zürich.* **96**, 1–23 (1951)

- Gor, G.Y.: Adsorption stress changes the elasticity of liquid argon confined in a nanopore. *Langmuir* **30**(45), 13564–13569 (2014)
- Gor, G.Y.: Bulk modulus of not-so-bulk fluid. In: *Poromechanics VI, Sixth Biot Conference on Poromechanics*, pp. 465–472 (2017). <https://doi.org/10.1061/9780784480779.057>
- Gor, G.Y., Gurevich, B.: Gassmann theory applies to nanoporous media. *Geophys. Res. Lett.* **45**(1), 146–155 (2018)
- Gor, G.Y., Siderius, D.W., Rasmussen, C.J., Krekelberg, W.P., Shen, V.K., Bernstein, N.: Relation between pore size and the compressibility of a confined fluid. *J. Chem. Phys.* **143**(19), 194506 (2015)
- Gor, G.Y., Siderius, D.W., Shen, V.K., Bernstein, N.: Modulus–pressure equation for confined fluids. *J. Chem. Phys.* **145**(16), 164505 (2016)
- Gor, G.Y., Huber, P., Bernstein, N.: Adsorption-induced deformation of nanoporous materials—a review. *Appl. Phys. Rev.* **4**(1), 011303 (2017)
- Gregg, S.J., Sing, K.S.W.: Adsorption, surface area and porosity. *Ber. Bunsenges. Phys. Chem.* **86**(10), 957 (1982)
- Hashin, Z., Shtrikman, S.: A variational approach to the theory of the elastic behaviour of multiphase materials. *J. Mech. Phys. Solids* **11**(2), 127–140 (1963)
- Huber, P.: Soft matter in hard confinement: phase transition thermodynamics, structure, texture, diffusion and flow in nanoporous media. *J. Phys. Condens. Matter* **27**(10), 103102 (2015)
- Jones, T.D.: Pore fluids and frequency-dependent wave propagation in rocks. *Geophysics* **51**(10), 1939–1953 (1986)
- Keeler, G., Batchelder, D.: Measurement of the elastic constants of argon from 3 to 77 degrees K. *J. Phys. C Solid State Phys.* **3**(3), 510 (1970)
- Knorr, K., Wallacher, D., Huber, P., Soprunyuk, V., Ackermann, R.: Are solidified fillings of mesopores basically bulk-like except for the geometric confinement? *Eur. Phys. J. E* **12**(1), 51–56 (2003)
- Kolesnikov, A., Georgi, N., Budkov, Y.A., Möllmer, J., Hofmann, J., Adolphs, J., Gläser, R.: Effects of enhanced flexibility and pore size distribution on adsorption-induced deformation of mesoporous materials. *Langmuir* **34**, 7575–7584 (2018)
- Kowalczyk, P., Balzer, C., Reichenauer, G., Terzyk, A.P., Gauden, P.A., Neimark, A.V.: Using in situ adsorption dilatometry for assessment of micropore size distribution in monolithic carbons. *Carbon* **103**, 263–272 (2016)
- Kuster, G.T., Toksöz, M.N.: Velocity and attenuation of seismic waves in two-phase media: part I. Theoretical formulations. *Geophysics* **39**(5), 587–606 (1974)
- Landers, J., Gor, G.Y., Neimark, A.V.: Density functional theory methods for characterization of porous materials. *Colloids. Surf. A Physicochem. Eng. Asp* **437**, 3–32 (2013)
- Mavko, G., Jizba, D.: Estimating grain-scale fluid effects on velocity dispersion in rocks. *Geophysics* **56**(12), 1940–1949 (1991)
- Mavko, G., Mukerji, T., Dvorkin, J.: *The rock physics handbook: tools for seismic analysis of porous media*. Cambridge University Press, Cambridge (2009)
- Maximov, M.A., Gor, G.Y.: Molecular simulations shed light on potential uses of ultrasound in nitrogen adsorption experiments. *Langmuir* **34**(51), 15650–15657 (2018)
- Milton, G.W.: *The theory of composites*. Cambridge University Press, Cambridge (2002)
- Molz, E., Wong, A.P., Chan, M., Beamish, J.: Freezing and melting of fluids in porous glasses. *Phys. Rev. B* **48**(9), 5741 (1993)
- Müller, T.M., Gurevich, B., Lebedev, M.: Seismic wave attenuation and dispersion resulting from wave-induced flow in porous rocks—a review. *Geophysics* **75**(5), 75A147–175A164 (2010)
- Norris, A.: A differential scheme for the effective moduli of composites. *Mech. Mater.* **4**(1), 1–16 (1985)
- Nygård, K.: Local structure and density fluctuations in confined fluids. *Curr. Opin. Colloid Interface Sci.* **22**, 30–34 (2016)
- O’Connell, R.J., Budiansky, B.: Viscoelastic properties of fluid-saturated cracked solids. *J. Geophys. Res.* **82**(36), 5719–5735 (1977)
- Page, J., Liu, J., Abeles, B., Herbolzheimer, E., Deckman, H., Weitz, D.: Adsorption and desorption of a wetting fluid in Vycor studied by acoustic and optical techniques. *Phys. Rev. E* **52**(3), 2763 (1995)
- Schappert, K., Pelster, R.: Elastic properties and freezing of argon confined in mesoporous glass. *Phys. Rev. B* **78**(17), 174108 (2008)
- Schappert, K., Pelster, R.: Freezing behavior of argon layers confined in mesopores. *Phys. Rev. B* **83**(18), 184110 (2011)
- Schappert, K., Pelster, R.: Continuous freezing of argon in completely filled mesopores. *Phys. Rev. Lett.* **110**(13), 135701 (2013a)
- Schappert, K., Pelster, R.: Elastic properties of liquid and solid argon in nanopores. *J. Phys. Condens. Matter* **25**(41), 415302 (2013b)
- Schappert, K., Pelster, R.: Influence of the Laplace pressure on the elasticity of argon in nanopores. *Europhys. Lett.* **105**(5), 56001 (2014)
- Schappert, K., Pelster, R.: Experimental method for the determination of adsorption-induced changes of pressure and surface stress in nanopores. *J. Phys. Condens. Matter* **29**(6), 06LT01 (2016)
- Shimizu, H., Tashiro, H., Kume, T., Sasaki, S.: High-pressure elastic properties of solid argon to 70 GPa. *Phys. Rev. Lett.* **86**(20), 4568 (2001)
- Siderius, D.W., Mahynski, N.A., Shen, V.K.: Relationship between pore-size distribution and flexibility of adsorbent materials: statistical mechanics and future material characterization techniques. *Adsorption* **23**(4), 593–602 (2017)
- Smith, T.M., Sondergeld, C.H., Rai, C.S.: Gassmann fluid substitutions: a tutorial. *Geophysics* **68**(2), 430–440 (2003)
- Thommes, M., Cychosz, K.A.: Physical adsorption characterization of nanoporous materials: progress and challenges. *Adsorption* **20**(2–3), 233–250 (2014)
- Thommes, M., Smarsly, B., Groenewolt, M., Ravikovitch, P.I., Neimark, A.V.: Adsorption hysteresis of nitrogen and argon in pore networks and characterization of novel micro- and mesoporous silicas. *Langmuir* **22**(2), 756–764 (2006)
- Thommes, M., Kaneko, K., Neimark, A.V., Olivier, J.P., Rodriguez-Reinoso, F., Rouquerol, J., Sing, K.S.: *Physisorption of gases, with special reference to the evaluation of surface area and pore size distribution (IUPAC Technical Report)*. *Pure Appl. Chem.* **87**(9–10), 1051–1069 (2015)
- Ustinov, E., Do, D.: Effect of adsorption deformation on thermodynamic characteristics of a fluid in slit pores at sub-critical conditions. *Carbon* **44**(13), 2652–2663 (2006)
- Wallacher, D., Knorr, K.: Melting and freezing of Ar in nanopores. *Phys. Rev. B* **63**(10), 104202 (2001)
- Warner, K., Beamish, J.: Ultrasonic measurement of the surface area of porous materials. *J. Appl. Phys.* **63**(9), 4372–4376 (1988)
- Wu, T.: The effect of inclusion shape on the elastic moduli of a two-phase material. *Int. J. Solids Struct.* **2**(1), 1–8 (1966)
- Zimmerman, R.W.: *Compressibility of sandstones*, vol. 29. Elsevier, New York (1990)

Publisher’s Note Springer Nature remains neutral with regard to jurisdictional claims in published maps and institutional affiliations.

Appendices

Appendix A

Statements of co-authors

Author 1: Boris Gurevich

To whom it may concern,

In the research leading to the following papers,

1. Sun, Y., Carcione, J. M., and Gurevich, B. (2020). Squirt-flow seismic dispersion models: A comparison. *Geophysical Journal International*, 222(3), 2068-2082.
2. Sun, Y., and Gurevich, B. (2020). Modeling the effect of pressure on the moduli dispersion in fluid-saturated rocks. *Journal of Geophysical Research: Solid Earth*, 125(8), e2019JB019297.
3. Sun, Y., Gurevich, B., Lebedev, M., Glubokovskikh, S., Mikhaltsevitch, V., and Guo, J. (2019). A triple porosity scheme for fluid/solid substitution: theory and experiment. *Geophysical Prospecting*, 67(4), 888–899.
4. Sun, Y., Gurevich, B., Glubokovskikh, S., Lebedev, M., Squelch, A., Arns, C., and Guo, J. (2019). A solid/fluid substitution scheme constrained by pore-scale numerical simulations. *Geophysical Journal International*, 220(3), 1804-1812.
5. Sun, Y., Gurevich, B., and Gor, G. Y. (2019). Modeling elastic properties of

vycor glass saturated with liquid and solid adsorbates. *Adsorption*, 25(5), 973–982. ,

my contribution focused on posing the problems, the supervision of these works and editing of the manuscripts. The bulk of the these works, including analytical analysis, numerical analysis, programming, modeling, and writing is done by Yongyang Sun.

Boris Gurevich

Signature:

Author 2: Stanislav Glubokovskikh

To whom it may concern,

In the research leading to the following papers,

1. Sun, Y., Gurevich, B., Lebedev, M., Glubokovskikh, S., Mikhaltsevitch, V., and Guo, J. (2019). A triple porosity scheme for fluid/solid substitution: theory and experiment. *Geophysical Prospecting*, 67(4), 888–899.
2. Sun, Y., Gurevich, B., Glubokovskikh, S., Lebedev, M., Squelch, A., Arns, C., and Guo, J. (2019). A solid/fluid substitution scheme constrained by pore-scale numerical simulations. *Geophysical Journal International*, 220(3), 1804-1812. ,

my contribution focused on posing the problems and the supervision of these works. The bulk of the these works, including analytical analysis, numerical analysis, programming, modeling, and writing is done by Yongyang Sun.

Stanislav Glubokovskikh

Signature:

Author 3: Maxim Lebedev

To whom it may concern,

In the research leading to the following papers,

1. Sun, Y., Gurevich, B., Lebedev, M., Glubokovskikh, S., Mikhailsevitch, V., and Guo, J. (2019). A triple porosity scheme for fluid/solid substitution: theory and experiment. *Geophysical Prospecting*, 67(4), 888–899.
2. Sun, Y., Gurevich, B., Glubokovskikh, S., Lebedev, M., Squelch, A., Arns, C., and Guo, J. (2019). A solid/fluid substitution scheme constrained by pore-scale numerical simulations. *Geophysical Journal International*, 220(3), 1804-1812. ,

my contribution focused on the supervision of these works and providing Yongyang Sun with the laboratory data used for the modeling. The bulk of the these works, including analytical analysis, numerical analysis, programming, modeling, and writing is done by Yongyang Sun.

Maxim Lebedev

Signature:

Author 4: Vassili Mikhaltsevitch

To whom it may concern,

In the research leading to the following paper,

1. Sun, Y., Gurevich, B., Lebedev, M., Glubokovskikh, S., Mikhaltsevitch, V., and Guo, J. (2019). A triple porosity scheme for fluid/solid substitution: theory and experiment. *Geophysical Prospecting*, 67(4), 888–899. ,

my contribution focused on providing technical advice and discussion. The bulk of the these works, including analytical analysis, numerical analysis, programming, modeling, and writing is done by Yongyang Sun.

Vassili Mikhaltsevitch

Signature:

Author 5: José M. Carcione

To whom it may concern,

In the research leading to the following paper,

1. Sun, Y., Carcione, J. M., and Gurevich, B. (2020). Squirt-flow seismic dispersion models: A comparison. *Geophysical Journal International*, 222(3), 2068-2082. ,

my contribution focused on posing the problem, the supervision of this work and the reviewing and editing of the manuscript. The bulk of the these works, including numerical analysis, programming, modeling, and writing is done by Yongyang Sun.

José M. Carcione

Signature:

Author 6: Gennady Gor

To whom it may concern,

In the research leading to the following paper,

1. Sun, Y., Gurevich, B., and Gor, G. Y. (2019). Modeling elastic properties of vycor glass saturated with liquid and solid adsorbates. *Adsorption*, 25(5), 973–982. ,

my contribution focused on posing the problem, the supervision of this work and the reviewing and editing of the manuscript. The bulk of the these works, including numerical analysis, programming, modeling, and writing is done by Yongyang Sun.

Gennady Gor

Signature:

Author 7: Christoph Arns

To whom it may concern,

In the research leading to the following paper,

1. Sun, Y., Gurevich, B., Glubokovskikh, S., Lebedev, M., Squelch, A., Arns, C., and Guo, J. (2019). A solid/fluid substitution scheme constrained by pore-scale numerical simulations. *Geophysical Journal International*, 220(3), 1804-1812. ,

my contribution focused on the supervision of this work and providing Yongyang Sun with technical advice and discussion on numerical simulations. The bulk of the these works, including numerical analysis, programming, modeling, and writing is done by Yongyang Sun.

Christoph Arns

Signature:

Author 8: Andrew Squelch

To whom it may concern,

In the research leading to the following paper,

1. Sun, Y., Gurevich, B., Glubokovskikh, S., Lebedev, M., Squelch, A., Arns, C., and Guo, J. (2019). A solid/fluid substitution scheme constrained by pore-scale numerical simulations. *Geophysical Journal International*, *220*(3), 1804-1812.

my contribution focused on the processing of the digital rock images used in this work. The bulk of these works, including numerical analysis, programming, modeling, and writing is done by Yongyang Sun.

Andrew Squelch

Signature:

Author 9: Junxin Guo

To whom it may concern,

In the research leading to the following paper,

1. Sun, Y., Gurevich, B., Lebedev, M., Glubokovskikh, S., Mikhaltsevitch, V., and Guo, J. (2019). A triple porosity scheme for fluid/solid substitution: theory and experiment. *Geophysical Prospecting*, 67(4), 888–899.
2. Sun, Y., Gurevich, B., Glubokovskikh, S., Lebedev, M., Squelch, A., Arns, C., and Guo, J. (2019). A solid/fluid substitution scheme constrained by pore-scale numerical simulations. *Geophysical Journal International*, 220(3), 1804-1812.

my contribution focused on providing Yongyang Sun with technical advice and discussion. The bulk of the these works, including analytical analysis, numerical analysis, programming, modeling, and writing is done by Yongyang Sun.

Junxin Guo

Signature:

Appendix B

Copyright Information

1. Sun, Y., Carcione, J. M., and Gurevich, B. (2020). Squirt-flow seismic dispersion models: A comparison. *Geophysical Journal International*, 222(3), 2068-2082.

4. Sun, Y., Gurevich, B., Glubokovskikh, S., Lebedev, M., Squelch, A., Arns, C., and Guo, J. (2019). A solid/fluid substitution scheme constrained by pore-scale numerical simulations. *Geophysical Journal International*, 220(3), 1804-1812.

What rights do I retain as an Oxford author?

- The right, after publication by Oxford University Press, to use all or part of the Article and abstract, for your own personal use, including your own classroom teaching purposes;
- The right, after publication by Oxford University Press, to use all or part of the Article and abstract, in the preparation of derivative works, extension of the article into book-length or in other works, provided that a full acknowledgement is made to the original publication in the journal;
- The right to include the article in full or in part in a thesis or dissertation, provided that this not published commercially;

2. Sun, Y., Carcione, J. M., and Gurevich, B. (2020). Squirt-flow seismic dispersion models: A comparison. *Geophysical Journal International*, 222(3), 2068-2082.

25/10/2020

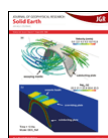
Mail - Yongyang Sun - Outlook

Thank you for your order with RightsLink / John Wiley and Sons

no-reply@copyright.com <no-reply@copyright.com>

Tue 11/08/2020 11:49 AM

To: Yongyang Sun <yongyang.sun@postgrad.curtin.edu.au>



Thank you for your order!

Dear Mr. Yongyang Sun,

Thank you for placing your order through Copyright Clearance Center's RightsLink® service.

Order Summary

Licensee: Mr. Yongyang Sun
Order Date: Aug 10, 2020
Order Number: 4885710003218
Publication: Journal of Geophysical Research: Solid Earth
Title: Modeling the Effect of Pressure on the Moduli Dispersion in Fluid-Saturated Rocks
Type of Use: Dissertation/Thesis
Order Total: 0.00 USD

View or print complete [details](#) of your order and the publisher's terms and conditions.

Sincerely,

Copyright Clearance Center

Tel: +1-855-239-3415 / +1-978-646-2777
customercare@copyright.com
<https://myaccount.copyright.com>



3. Sun, Y., Gurevich, B., Lebedev, M., Glubokovskikh, S., Mikhaltsevitch, V., and Guo, J. (2019). A triple porosity scheme for fluid/solid substitution: theory and experiment. *Geophysical Prospecting*, 67(4), 888–899.

25/10/2020

Mail - Yongyang Sun - Outlook

Thank you for your order with RightsLink / John Wiley and Sons

no-reply@copyright.com <no-reply@copyright.com>

Tue 11/08/2020 1:28 PM

To: Yongyang Sun <yongyang.sun@postgrad.curtin.edu.au>



Thank you for your order!

Dear Mr. Yongyang Sun,

Thank you for placing your order through Copyright Clearance Center's RightsLink® service.

Order Summary

Licensee: Mr. Yongyang Sun
Order Date: Aug 11, 2020
Order Number: 4885741433370
Publication: Geophysical Prospecting
Title: A triple porosity scheme for fluid/solid substitution: theory and experiment
Type of Use: Dissertation/Thesis
Order Total: 0.00 AUD

View or print complete [details](#) of your order and the publisher's terms and conditions.

Sincerely,

Copyright Clearance Center

Tel: +1-855-239-3415 / +1-978-646-2777
customer-care@copyright.com
<https://myaccount.copyright.com>



This message (including attachments) is confidential, unless marked otherwise. It is intended for the addressee(s) only. If you are not an intended recipient, please delete it without further

<https://outlook.office.com/mail/search/id/AAQkADi0MjWmZDgwLTUwNTgtNGQ1MS1hMzhlTFmOGRhNzMyZjhlNgAQAD1LPYM4GXmEzEKHhRUC...> 1/2

5. Sun, Y., Gurevich, B., and Gor, G. Y. (2019). Modeling elastic properties of vycor glass saturated with liquid and solid adsorbates. *Adsorption*, 25(5), 973–982.

26/10/2020

Mail - Yongyang Sun - Outlook

RE: Permission request

Journalpermissions <journalpermissions@springernature.com>

Mon 10/08/2020 11:19 PM

To: Yongyang Sun <yongyang.sun@postgrad.curtin.edu.au>

Dear Yongyang,

Thank you for your Springer Nature permissions query. Author retains the right to use his/her article for his/her further scientific career by including the final published journal article in other publications such as dissertations and postdoctoral qualifications provided acknowledgement is given to the original source of publication.

You do not need permission to reuse your article in a thesis/dissertation.

Best regards,

Paloma Hammond
Rights AssistantSpringerNature
The Campus, 4 Crinan Street, London N1 9XW, United Kingdom

E paloma.hammond@springernature.com

<https://www.macmillanihe.com/>
<http://www.nature.com>
<http://www.springer.com>
<https://www.palgrave.com/gp/>

BLACK LIVES MATTER

From: Yongyang Sun [mailto:yongyang.sun@postgrad.curtin.edu.au]**Sent:** 10 August 2020 10:24**To:** Journalpermissions**Subject:** Permission request**[External - Use Caution]**

To whom it may concern,

I am a PhD student at Curtin University, Australia and I am planning to submit my thesis by publication. I have published the following articles in Adsorption Journal of the International Adsorption Society

Sun, Y., Gurevich, B. & Gor, G.Y. Modeling elastic properties of Vycor glass saturated with liquid and solid adsorbates. *Adsorption* 25, 973–982 (2019). <https://doi.org/10.1007/s10450-019-00123-4>

In order to be able to include this publication in my thesis, I ask you herby for permission to do so. If you have any further questions please do not hesitate to contact me.

<https://outlook.office.com/mail/search/id/AAQkADI0MWJmZDgwLTlwNTgtNGQ1MS1hMzhiLTFnOGRhNzMyZjhlNgAQABC4hN6100plgK2MRLEqQH%...> 1/2

Every reasonable effort has been made to acknowledge the owners of copyright material. I would be pleased to hear from any copyright owner who has been omitted or incorrectly acknowledged.